2017

Grain Boundary Transport Mechanisms of Oxidation Behaviors in Alumina

Yan Wang
Lehigh University

Grain Boundary Transport Mechanisms of Oxidation Behaviors in Alumina

By

Yan Wang

Presented to the Graduate and Research Committee

of Lehigh University

in Candidacy for the Degree of

Doctor of Philosophy

in

Materials Science and Engineering

Lehigh University

August 2017

DISSERTATION SIGNATURE SHEET

Approved and recommended for acceptance as a dissertation in fulfillment of the requirements for the degree of Doctor and Philosophy.

Date

Dissertation Director

Accepted Date

Committee Members:

Martin P. Harmer

Helen M. Chan

Jeffrey M. Rickman

Shen J. Dillon

Dedicated to

Weiqi Wang, Meiyun Wang and Ying Zheng

ACKNOWLEDGEMENTS

First, I would like to thank my advisor, Prof. Martin P. Harmer, for giving me the opportunity to work with him for my PhD research. I really appreciate his encouragement and guidance during my PhD. His advising helped me learn not only new knowledge but methods to consider and analyze problems. I would also like to thank my co-advisor, Prof. Helen M. Chan, for her patience, guidance and help. She was always supportive when I had problems. Special thanks also to my other co-advisor Prof. Jeffrey M. Rickman for his insightful discussions and challenging questions, and my committee member Prof. Shen J. Dillon for his support and setting a good example for PhD students.

I would like to thank my group members, Shuailei Ma, Patrick Cantwell, Zhiyang Yu, Animesh Kundu, Qian Wu, Abigail Lawrence, Onthida Schumacher, Mike Kracum, Kevin Anderson, Denise Yin and Chris Marvel for their help both inside and outside the lab. It was a pleasure to work with them. Special thanks to Zhiyang for training and helping me on TEM operation and analysis, to Animesh for helping me with lab equipment setup and maintenance, and to Qian for training me on lab operations when I started. I also want to thank William Mushock, Suxing Wu, Robert Keyse and Micheal Rex for their technical training and help with my research.

I want to thank my officemates, Li Lv, Kevin Anderson, Mike Kracum, Sean McAnany, Charlie McLaren and Sultan Althahban for having fun together. Special thanks to Kevin, Mike, Sean and Charlie for their patience with my English questions. Office basketball and hard work at 4:30pm were always enjoyable. I also want to thank all the graduate students in the department.

I would also like to thank the administrative staff in the department and the Center for Advanced Materials and Nanotechnology, Susan Stetler, Janie Carlin, Katrina Kraft, Lisa Arechiga, Mary Anne Lynch and Anne Marie Lobley. They treated me as their family.

Finally, I would like to thank my family for their endless support. I can never thank my dad and mom enough, Weiqi Wang and Meiyun Wang, for their love. And I could not enjoy my life more without my wife, Ying Zheng.

Table of Contents

LIST OF TABLES

LIST OF FIGURES

ABSTRACT

Ni-based superalloys are resistant to high temperature oxidation due to the formation of a protective alumina scale known as a thermally grown oxide (TGO). The growth of the TGO in thermal barrier coatings (TBCs) is responsible for the spallation failure of the coatings. It is important to study grain boundary (GB) transport in alumina to understand the mechanisms of the growth of the alumina scale. This work studied the grain boundary transport in alumina from two aspects. The first was to study the effect of oxygen partial pressure (P_{O_2}) on the grain boundary transport in alumina. During the formation, there is a large P_{O_2} gradient across the alumina scale. But how the grain boundary transport varies under different P_{O_2} inside the alumina scale is still under debate. The second was to study the effect of Hf-doping on the grain boundary transport in alumina at different temperatures. It is well known that the addition of reactive elements, such as Hf and Y, can effectively increase the oxidation resistance of the alumina forming alloys. But the mechanism by which Hf-doping has a beneficial effect on slowing down grain boundary transport in alumina is still unclear.

In the first part of this study, grain boundary transport was measured in alumina under P_{O_2} ranging from 10^{-10} to 10^{-18} at 1400°C. Dense polycrystalline alumina samples containing nickel aluminate spinel marker particles were reduced and the reduction rates were measured at different P_{O_2}. The results showed that the dependence of the grain boundary transport on P_{O_2} is mainly due to the driving force, which is the gradient of P_{O_2} across the alumina. The point defect model which is most consistent with the measured results is one that assumes ionic diffusion determines the overall transport and the

concentration of ionic defects is determined by impurities. The results of this study confirm that transport in a formed alumina scale is controlled by extrinsic defects and not by intrinsic defects as suggested by other researchers.

The second part of this study uses the oxidation of Ni marker particles to measure the influence of Hf^{4+} on the grain boundary transport in polycrystalline alumina. At temperatures above 1250°C, 500ppm Hf doping retarded the transport by a factor of 8, whereas the retardation increased to a factor of 20 below 1200°C. The GB structures in samples subjected to oxidation heat-treatments at 1400°C and 1150°C were studied using aberration-corrected high-angle annular dark field (HAADF) scanning transmission electron microscopy (STEM) imaging. The results show that Hf^{4+} strongly segregated at alumina grain boundaries and occupied Al^{3+} sites. There was a large frequency of GBs exhibiting {2-1-10} facets at 1400°C. Whereas at 1150°C, there was a large proportion of non-faceted GBs. Together with the previous results of the effect of Hf concentration on grain boundary transport in alumina, the results showed that the effect of Hf-doping on slowing down grain boundary transport in alumina is consistent with a site-blocking mechanism. These results taken together indicate a possible occurrence of a grain boundary complexion transition taking place in the current system. This study has revealed novel aspects of the oxidation behavior in Hf-doped alumina, and also suggested a complex influence of dopants and temperature on the GB structures and kinetic properties.

CHAPTER 1 INTRODUCTION

High temperature gas turbine systems rely on a thermal protection coating system comprising a metallic bond coat and a ceramic coating. During service, oxidation of the bond coat results in the formation of an alumina layer whose growth rate dictates the lifetime of the coating[1–3]. Thus, the study of the transport mechanisms in this alumina layer is of considerable scientific and technological importance.

Alumina scales experience large gradients of oxygen partial pressure (P_{O_2})[4], but it is unclear how P_{O_2} affects grain boundary transport in alumina. It has been generally assumed that alumina exhibits negligible nonstoichiometry and that the concentration of point defects is independent of P_{O_2}. However, recent high temperature oxygen permeation experiments by Kitaoka et al.[5–9] at 1650°C suggested a dependence of grain boundary diffusivities on P_{O_2}, which was interpreted using an intrinsic point defect chemistry model. In order to shed more light on this subject, GB transport rates were measured in alumina under P_{O_2} from 10^{-10} to 10^{-20} at 1400°C. The results will be discussed in terms of the functional dependence of the GB transport on P_{O_2}, and the implications for the role of alumina nonstoichiometry (if any).

It is well known that reactive elements, such as Hf, Y and Zr, can retard oxidation of alumina forming alloys[10,11]. Many studies have sought to understand the mechanisms by which oxidation is inhibited[10–14]. However, the complex chemistry of commercial high-temperature alloys makes a detailed analysis of these systems rather difficult. For this reason, a Ni marker experiment has been employed to study the effect of reactive elements on the oxidation behavior in alumina[15,16]. Previous study has given some indications

that multiple diffusion mechanisms may be operative at grain boundaries owing to boundary transitions that modify local structure and chemistry[17]. To assess the impact of such transitions on transport, more oxidation experiments at low temperatures were conducted. Also, the structures of many GBs were characterized using atomic resolution STEM to complete the comparison of the GB structures between samples subjected to oxidation heat-treatments at 1400°C and 1150°C. The kinetic data will be correlated with GB structures for understanding the effect of RE dopants in this technologically important temperature regime.

CHAPTER 2 BACKGROUND

This chapter provides a basic review and analysis of relevant prior research in the literature.

2.1 Effects of Reactive Elements on the Growth of Alumina Scales

Alumina scales form on the surface of Ni-based and Fe-based alumina forming alloys when the alloys are exposed at high operating temperatures in oxidizing atmosphere. The growth of alumina scales is ultimately responsible for the spallation failure of thermal barrier coatings (TBCs)[1,2,18]. Many studies have been done to understand the growth mechanisms of alumina scales, and on strategies for slowing down the growth rate of alumina scales[11,12,19–21].

The grown alumina scales are polycrystalline α-Al_2O_3[22,23]. Since lattice diffusion is so slow in alumina, the diffusion through alumina scales is dominated by grain boundary diffusion[24]. Alumina scales were believed to grow predominantly by O inward diffusion from inert Pt marker studies[25,26]. But more recent two-stage oxidation studies indicated that a considerable amount of Al outward diffusion occurred during scale growth[19,27–32]. Figure 2.1 shows the oxygen isotope profile after two-stage oxidation of an FeCrAl alloy at 1000°C first in $^{16}O_2$ for 2.5h, then in $^{18}O_2$ for 5h[30]. There is a large peak of ^{18}O present at the scale-gas interface. Part of the presence of ^{18}O was due to oxygen isotope exchange, but the majority of ^{18}O was believed to be due to new oxide formation from Al outward diffusion[10].

It has been found that the addition of reactive elements (e.g. Hf, Y, Zr) can effectively increase the oxidation resistance of alumina forming alloys[10,12,33,34]. Figure 2.2 shows Hf-doping and Zr-doping reduced the alumina scale growth rate by a factor of 10 during

the oxidation of a β-NiAl alloy at 1200°C[34]. Table 2.1 shows the summarized results on the effect of reactive element addition on oxidation rates[10]. Among all the studies, Hf was found to be one of the most effective elements that could slow down alumina scale growth rate[33]. Figure 2.3 shows the effects of various reactive elements and their combinations on the oxidation rate of FeCrAl alloys at 1200°C. 500ppm Hf-doped sample had the lowest oxidation rate.

Many researchers tried to understand the mechanisms of the effects of reactive elements on reducing growth rate of alumina scale. Two-stage oxidation experiments showed that RE doping effectively reduces Al outward diffusion but has little effect on O inward diffusion[10,27–32,35,36]. TEM studies showed that reactive elements segregate at GBs in alumina scales[37]. The mechanisms of Hf-doping on slowing down grain boundary transport in alumina is a topic of this investigation, and will be discussed in 5.2.

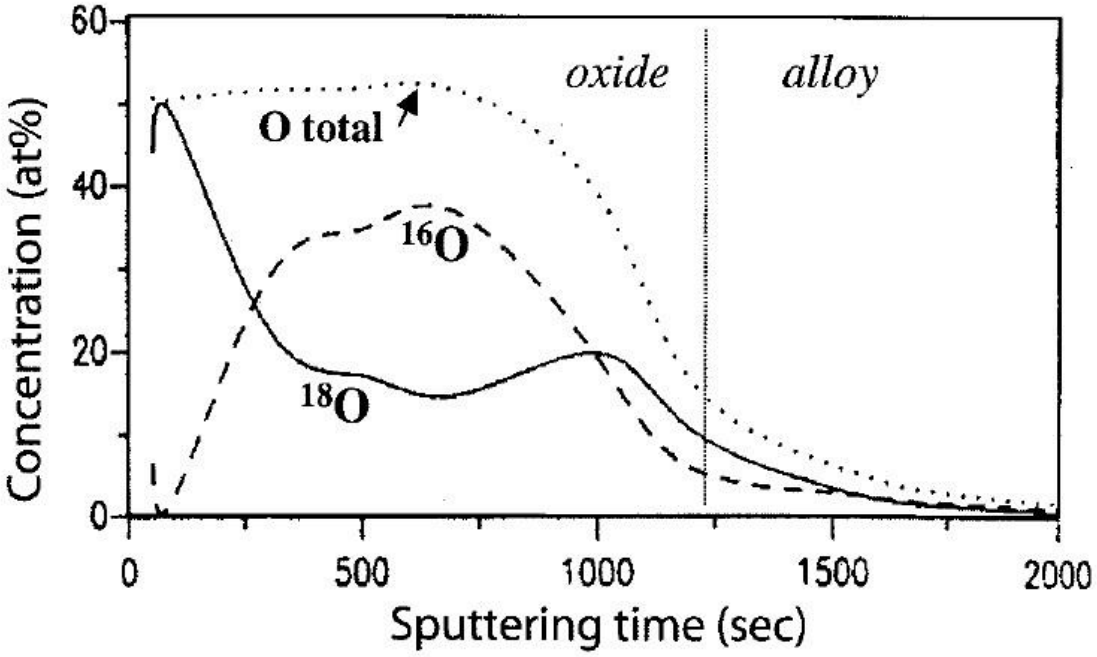

Figure 2.1 Oxygen isotope profile after two-stage oxidation of an FeCrAl alloy oxidized at 1000°C first in $^{16}O_2$ for 2.5h, then in $^{18}O_2$ for 5h[30].

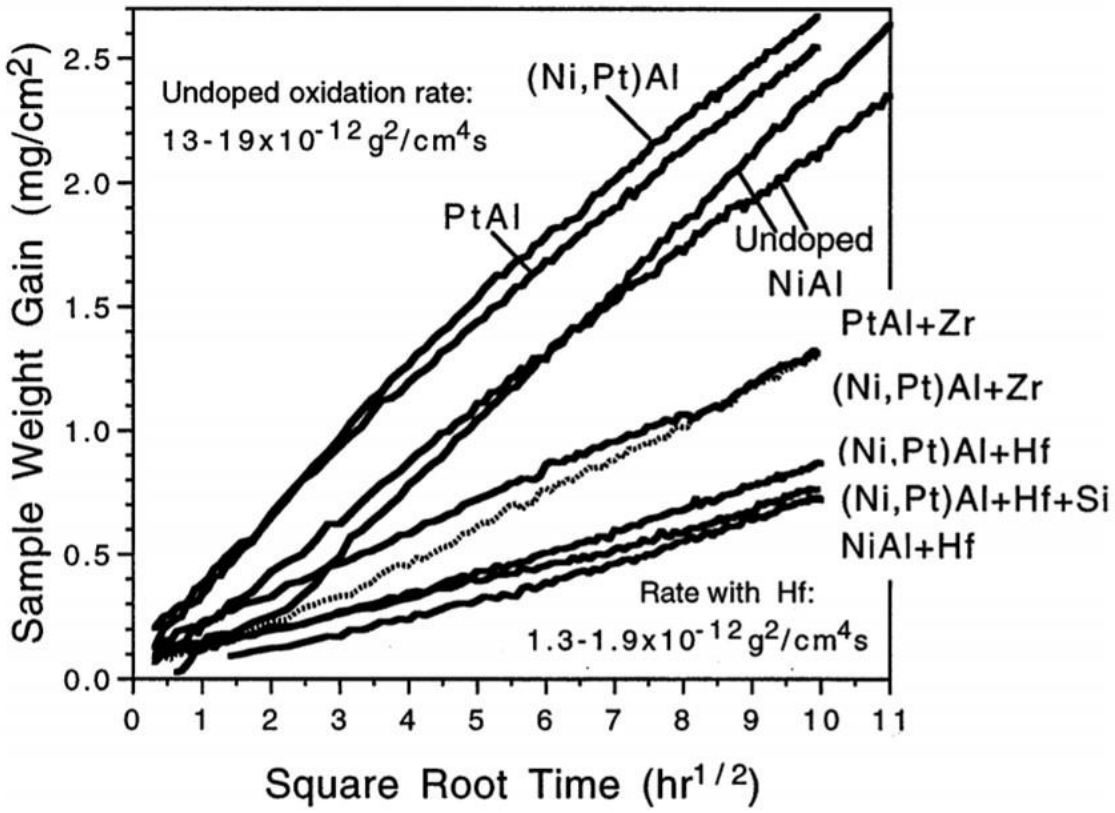

Figure 2.2 Isothermal weight gains at 1200°C plotted versus the square root of time[34].

Table 2.1 Effect of reactive element addition on oxidation rates[10].

Alloy system	Oxidation condition (°C)	Rate without RE	RE type	Rate with RE
NiAl	1200	$(1.4 \pm 0.4) \times 10^{-11}$	Ti, La, Zr, Hf, Y	$(8.0 \pm 4.1) \times 10^{-12}$
Ni_3Al		7.1×10^{-12}	Y	$(4.3 \pm 3.1) \times 10^{-12}$
Fe_3Al		$(1.3 \pm 0.2) \times 10^{-11}$	Hf, Zr, Y	$(4.9 \pm 2.4) \times 10^{-12}$
FeCrAl		$(1.8 \pm 0.6) \times 10^{-11}$	Nb, Ti, Sc, Hf, Gd, Ba, Nd, La, Zr, Y	$(7.1 \pm 2.8) \times 10^{-12}$
PtAl		$(1.6 \pm 0.4) \times 10^{-11}$	Zr	4.1×10^{-12}
FeCrAl	1200	7.8×10^{-12}	Y	4.1×10^{-12}
FeCrAl	1150	8.5×10^{-12}	Ti	2×10^{-13}
NiCrAl	1100	1.1×10^{-12}	Y, Hf	$(4.5 \pm 2.1) \times 10^{-13}$

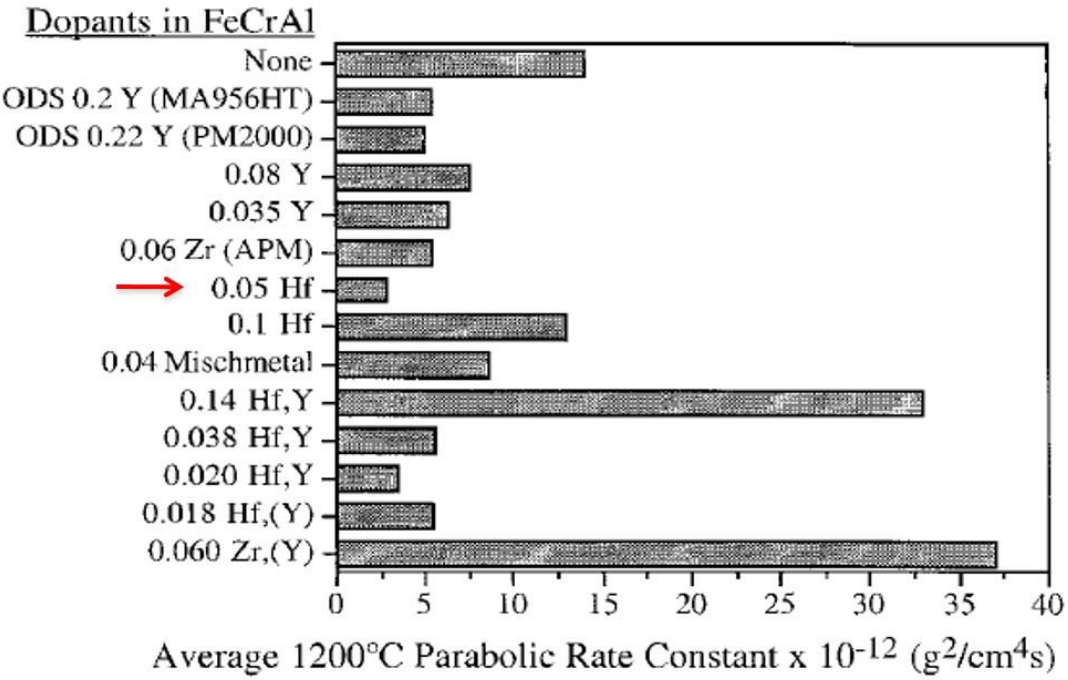

Figure 2.3 Oxidation rates for various commercial and laboratory FeCrAl compositions at 1200°C.

2.2 Wagner Oxidation Theory

The mechanisms and rates of oxidizing a metal, M, to a compound, M_aX_b, is described in this section according to the models developed by Wagner. The same analysis can be applied to reducing a compound, M_aX_b, to a metal, M. Wagner provided a theory for understanding oxidation of pure metals[38–40]. For an ionic compound M_aX_b, diffusion of cations, M^{z_m}, anions, X^{z_x} and electrons, e^-, were considered. Figure 2.4 shows a schematic diagram of the formation of an oxide, MO, according to Wagner's model. Several assumptions were made for the derivation. These charged particles were assumed to migrate independently of each other. The migration of these charged particles was assumed to control the rate of oxidation by assuming the reaction happened much faster than diffusion. It was also assumed that thermodynamic equilibrium was established at the oxidation front, the surface and throughout the oxidized region.

Since the diffusion of the charged particles is not equal, a separation of charges takes place across the oxidized region. The resulting space charge creates an electric field which opposes a further separation of charges, and a stationary state is reached for which no net electric current flows through the oxidized region. For each type of particle i (M^{z_m}, X^{z_x} and e^-), the flux is given by Eq. (2.1),

$$J_i = -\frac{D_i C_i}{RT}\left(\frac{d\mu_i}{dx} + z_i F \frac{d\varphi}{dx}\right) \qquad (2.1)$$

where D_i is the diffusivity, C_i is the concentration, R is the gas constant, T is the temperature, μ_i is the chemical potential, z_i is the charge, F is the Faraday constant and φ is the generated electrical potential. After applying the Nernst–Einstein Equation:

$$\frac{\sigma_i}{(z_i F)^2} = \frac{D_i C_i}{RT} \quad (2.2)$$

Eq. (2.1) can be expressed as:

$$J_i = -\frac{\sigma t_i}{(z_i F)^2}\left(\frac{d\mu}{dx} + z_i F \frac{d\varphi}{dx}\right) \quad (2.3)$$

Where σ is the total electrical conductivity and t_i is the transference number for species i.

Using the electrical neutrality relation and with the assumption that thermodynamic equilibrium was established at the oxidation front, the surface and throughout the oxidized region, the total flux of M_aX_b formed can be derived as:

$$J_{M_aX_b} = \frac{\sigma t_{ion} t_e}{b z_x^2 F^2} \frac{d\mu_x^0}{dx} \quad (2.4)$$

where t_{ion} is the total ionic transference number, t_e is the total electronic transference number and μ_x^0 is the chemical potential of species X at its neutral state. For oxides, X is oxygen. The chemical potential of oxygen can be calculated using oxygen partial pressure, P_{O_2}.

$$d\mu_0^0 = \frac{1}{2} RT d\ln P_{O_2} \quad (2.5)$$

And by assuming steady state is maintained through the oxides, Eq. (2.4) can be integrated over the thickness of the oxides, *l*.

$$J_{M_aO_b} = \frac{1}{l}\frac{RT}{8bF^2}\int_{P_{O_2}^{low}}^{P_{O_2}^{high}} \sigma t_{ion} t_e \, d\ln P_{O_2} \quad (2.6)$$

Eq. (2.6) can be expressed using cation and anion diffusivity by the Nernst-Einstein Equation.

$$J_{\mathrm{M}_a\mathrm{O}_b} = \frac{1}{l}\frac{C_{\mathrm{O}}}{2b}\int_{P_{\mathrm{O}_2}^{low}}^{P_{\mathrm{O}_2}^{high}} (\frac{z_m}{2}D_{\mathrm{M}} + D_{\mathrm{O}})t_e \, d\ln P_{\mathrm{O}_2} \qquad (2.7)$$

where C_{O} is the concentration of oxygen in the oxide, D_{M} and D_{O} are the effective diffusivities of cations and anions. For polycrystalline materials, in which grain boundary diffusion is much faster than lattice diffusion.

$$D_i = \frac{2\delta}{G}D_i^{GB} \qquad (2.8)$$

where δ is the width of GBs and G is the grain size. All grains are assumed to have size and cubic shape and all grain boundaries are assumed to have the same width to derive this equation.

The growth rate of the oxide is proportional to $J_{\mathrm{M}_a\mathrm{O}_b}$. Eq. (2.6) shows that the growth rate is determined by two factors. The first is the thermodynamic driving force, which is the gradient of P_{O_2} across the oxide. The second factor is the ionic conductivity and electronic conductivity which are both kinetic parameters of the material. It is worth noting that since the derivation above assumes that transport determines the overall oxidation process, the equation derived can also be applied to the reduction process which is determined by transport.

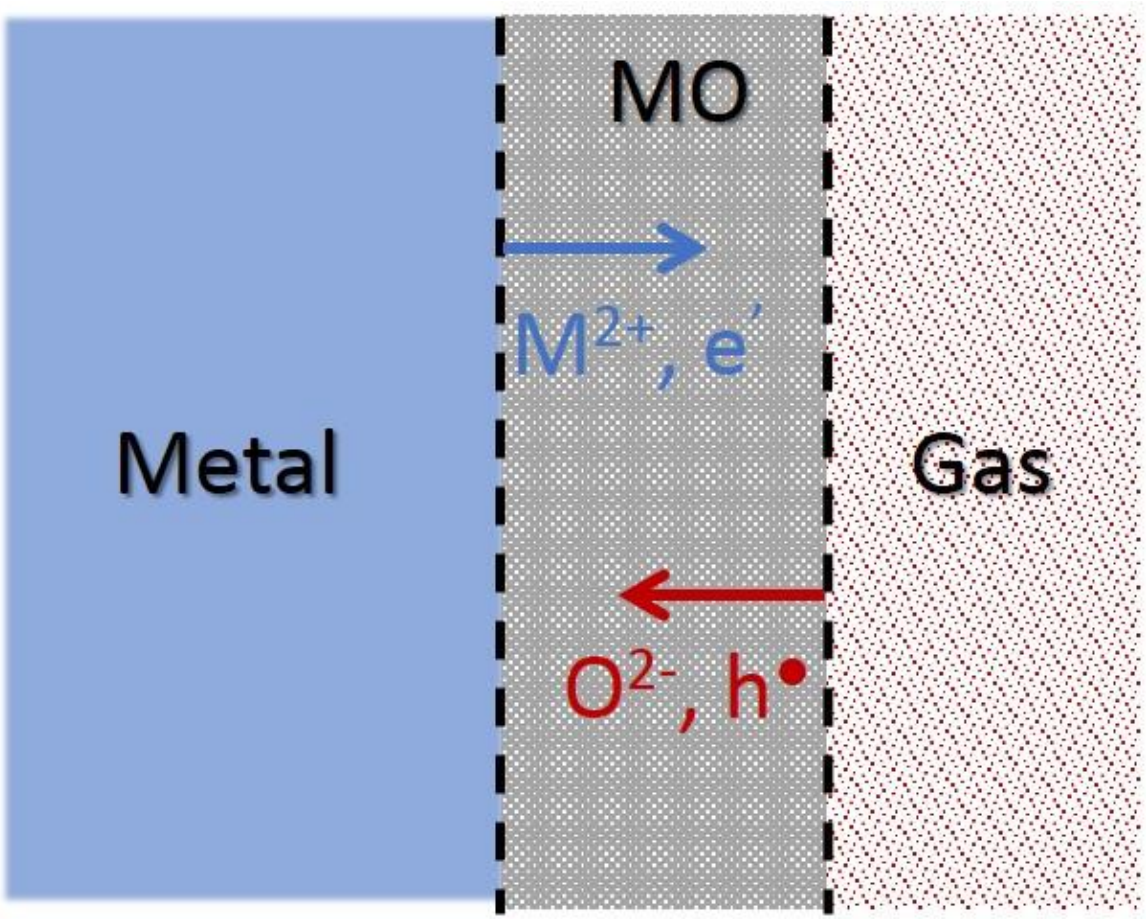

Figure 2.4 Schematic diagram of the formation of an oxide, MO, according to Wagner's model.

2.3 Electrical Conduction in Alumina

Electrical conductivity and ionic transference number in alumina at high temperature have been measured in both ceramics and in alloy-scale systems[41–47]. The total electrical conductivity in alumina generally falls into the same range, while there is a large discrepancy between the results of the ionic transference number in alumina.

The electromotive force (EMF) method has been used to determine ionic transference numbers in alumina. Under a P_{O_2} gradient, oxygen diffuses through alumina and generates an electrical potential across alumina, as mentioned in 2.2. It can be derived the relationship between the voltage measured across alumina, ΔV, and ionic transference number through Eq. (2.9).

$$\Delta V = \frac{RT}{4F} \int_{P_{O_2}^{low}}^{P_{O_2}^{high}} t_{ion}\, d\ln P_{O_2} \qquad (2.9)$$

By fixing $P_{O_2}^{low}$ on one side of alumina, and measuring ΔV under different $P_{O_2}^{high}$ on the other side, t_{ion} can be determined by Eq. (2.10).

$$t_{ion} = \frac{\partial(4F\Delta V/RT)}{\partial \ln P_{O_2}^{high}} \qquad (2.10)$$

Pappis and Kingery found that the total electrical conductivity of single-crystal and polycrystalline alumina were similar at temperature from 1300°C to 1750°C, and under oxygen partial pressure from 10^{-10} to 1[41]. Alumina exhibits p-type conductivity at high P_{O_2} and n-type conductivity at low P_{O_2}. Electronic conduction was believed to dominate the total conduction. An extrinsic defect model was applied to explain the results.

Kitazawa and Coble measured the electrical conductivity and ionic transference number in single-crystal and polycrystalline alumina[42]. They also found that total electrical conduction of single-crystal alumina and polycrystalline alumina behaved alike. From 1200°C to 1600°C, single-crystal alumina exhibited intrinsic electronic conduction under low and high P_{O_2}, and extrinsic ionic conduction under intermediate P_{O_2}, while polycrystalline alumina exhibited intrinsic electronic conduction over the whole temperature range. They attributed this difference to an enhanced electronic conductivity at grain boundaries in polycrystalline alumina. They also measured the ionic transference number in MgO-doped polycrystalline alumina at different temperatures under the same P_{O_2} gradient and at 1012°C under different P_{O_2} gradient. Figure 2.5A shows that electronic conduction became more predominant at higher temperature, and Figure 2.5B shows that at 1012°C, ionic transference number varied from 0.01 to 0.21 as P_{O_2} decreased from 10^{-9} to 10^{-15}. Their results indicate that even the ionic transference number in MgO-doped polycrystalline alumina depended on P_{O_2}, it was much smaller than electronic transference number at 1100°C and above.

Chen and Kroger measured the electrical conductivity and ionic transference number in Ni doped single-crystal alumina at 1500°C and 1600°C[43]. The total conductivity was within the range of the results Kitazawa and Coble measured, but about 2 orders of magnitude lower than Pappis and Kingery's results. They found that the ionic transference number is close to 1 under P_{O_2} below 10^{-3}.

There are also studies that measured the electrical properties of alumina scales. Sheasby and Jory found that alumina scales formed on a Pt-Al alloy behaved as a mixed conductor

(t_{ion}~0.5) down to 10^{-15}, and as a majority electronic conductor under lower P_{O_2} at 1100°C[44]. Nicolas-Chaubet et al. developed a formalism which allowed them to use potential-current curves at various P_{O_2} to determine the conductivity as a function of P_{O_2} [45]. They showed that alumina scales formed on a β-NiAl alloy behaved as an electronic conductor under P_{O_2} above 10^{-8}, and as an ionic conductor under P_{O_2} below 10^{-8} at 1100°C[46]. Balmain and Huntz adopted the formalism that Nicolas-Chaubet et al. developed and showed that the ionic transference number in alumina scales formed on a β-NiAl alloy increased from near 0 to 0.55 as P_{O_2} decreased from 1 to 10^{-14} at 1100°C[47]. These results were summarized in Figure 2.6.

The results in the literature show that there is no agreement on the value of ionic transference number in polycrystalline alumina. However, the results from Balmain and Huntz had a similar trend as the results from Kitazawa and Coble. They both found that the ionic transference number in polycrystalline alumina increased at lower P_{O_2} below 1100°C. Furthermore, Kitazawa and Coble found that the ionic transference number became much smaller than electronic transference number when temperature was above 1100°C.

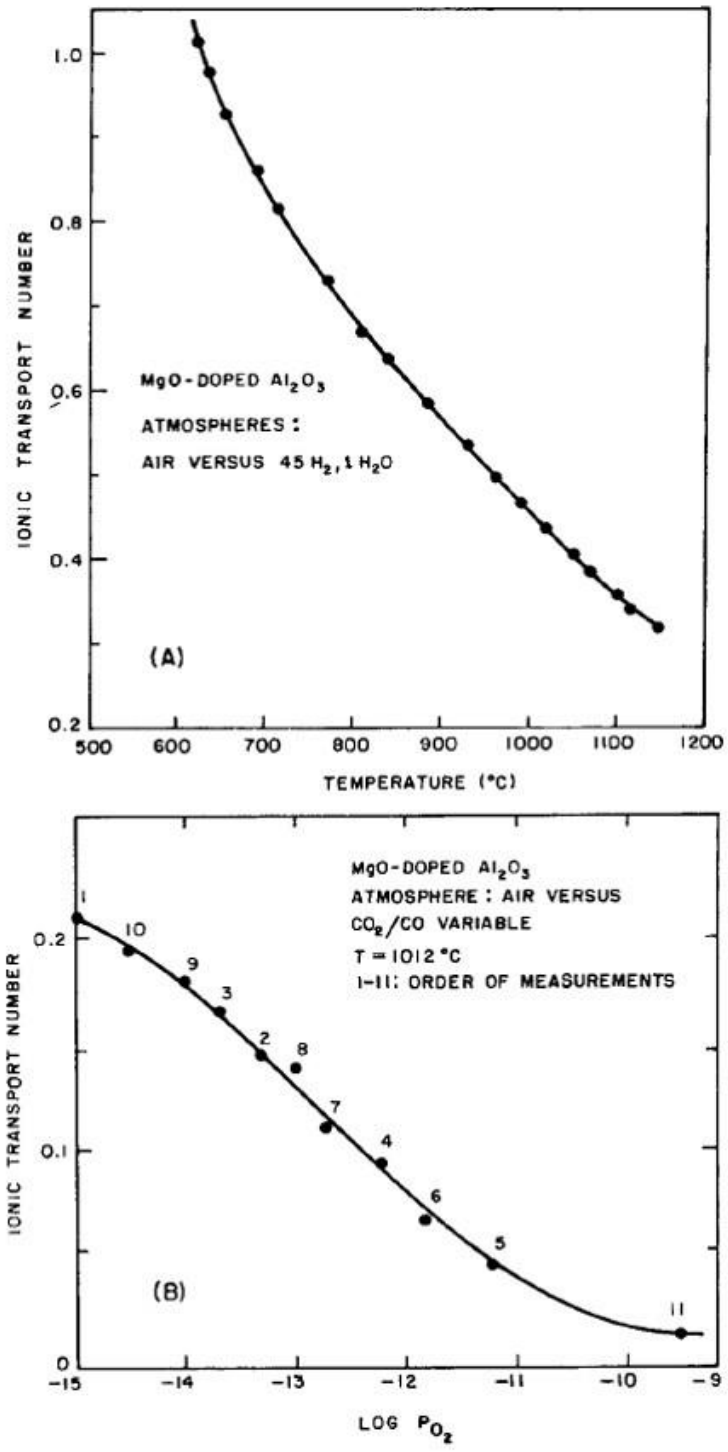

Figure 2.5 Dependence of ionic transference number on (A) temperature and (B) P_{O_2} in MgO-doped alumina[42].

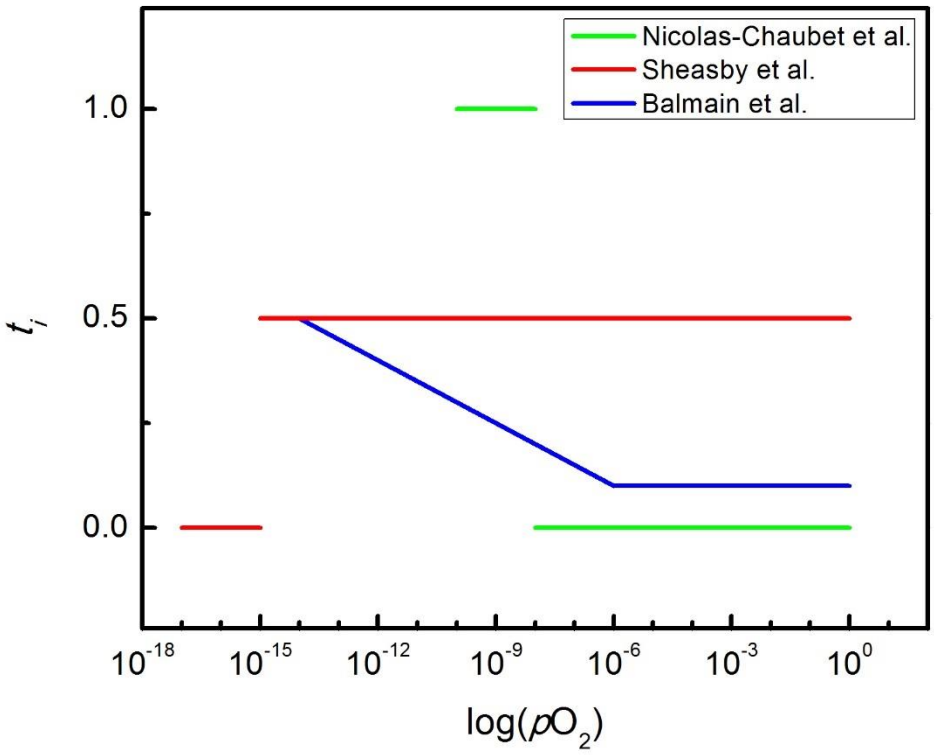

Figure 2.6 Dependence of ionic transference number in alumina scale on P_{O_2} measured in alloy-scale systems at 1100°C[44,46,47].

2.4 Point Defect Chemistry of Alumina

Point defect chemistry can be used to explain transport behavior in material phenomena[48]. The major types of intrinsic ionic defects in alumina are Schottky defects, aluminum and oxygen Frenkel defects. The formation of Schottky defects can be expressed by Eq. (2.11).

$$null = 2V_{\mathrm{Al}}''' + 3V_{\mathrm{O}}^{\cdot\cdot} \qquad (2.11)$$

where V_{Al}''' represents an aluminum vacancy and $V_{\mathrm{O}}^{\cdot\cdot}$ represents an oxygen vacancy. Kroger-Vink notation is used in this dissertation to describe point defects. Aluminum and oxygen Frenkel defects can be expressed by Eq. (2.12) and Eq. (2.13) respectively.

$$null = V_{\mathrm{Al}}''' + \mathrm{Al}_i^{\cdot\cdot\cdot} \qquad (2.12)$$

where $\mathrm{Al}_i^{\cdot\cdot\cdot}$ represents an aluminum interstitial.

$$null = V_{\mathrm{O}}^{\cdot\cdot} + \mathrm{O}_i'' \qquad (2.13)$$

where O_i'' represents an oxygen interstitial.

The formation energy of these defects has been studied by both experiments and theoretical calculation. Kroger et al. measured the concentration of Ti^{3+} and Ti^{4+} in Ti-doped alumina and the concentration of Fe^{2+} and Fe^{3+} in Fe-doped alumina to calculate the formation energy of Schottky defects and aluminum Frenkel defects[49–52]. Matsunaga et al.[53] and Hine et al.[54] used density functional theory (DFT) calculation to calculate the formation energies. Catlow et al.[55], Grimes[56] and Lagerlof et al.[57] also used empirical methods to calculate the formation energies. The results in the literature are summarized in Table 2.2. There is good agreement between the experimental data and the DFT calculations. The relative formation energies in alumina are Schottky < Al Frenkel <

O Frenkel. This indicates that V_{Al}''' and $V_{\mathrm{O}}^{\cdot\cdot}$ are the dominant intrinsic defects in undoped alumina.

The intrinsic electronic defects in alumina are electrons and holes. The formation of these two defects can be expressed by Eq. (2.14).

$$null = e' + h^{\cdot} \qquad (2.14)$$

Kroger et al.[52] used the value of 10.4eV as the band gap of alumina at 0K[58], while both Matsunaga et al.[53] and Hine et al.[54] used the value of 9.1eV as the band gap of alumina at 0K[59].

Chen and Kroger[43] also calculated the formation energies of intrinsic defects in Ni-doped alumina.

$$\frac{1}{2}\mathrm{O}_2 = \mathrm{O}_{\mathrm{O}}^{\times} + \frac{2}{3}V_{\mathrm{Al}}''' + 2h^{\cdot} \qquad (2.15)$$

The formation energy of Eq. (2.15), ΔH_p, is 11.72eV.

$$\mathrm{O}_{\mathrm{O}}^{\times} = \frac{1}{2}\mathrm{O}_2 \uparrow + V_{\mathrm{O}}^{\cdot\cdot} + 2e' \qquad (2.16)$$

The formation energy of Eq. (2.16), ΔH_n, is 15.36eV.

$$\mathrm{O}_{\mathrm{O}}^{\times} = \frac{1}{2}\mathrm{O}_2 \uparrow + \frac{2}{3}\mathrm{Al}_i^{\cdot\cdot\cdot} + 2e' \qquad (2.17)$$

The formation energy of Eq. (2.17), $\Delta H_{n'}$, is 14.91eV.

Using formation energy, the concentration of each defect at a given temperature can be calculated by assuming the formation entropy is 0.5meV/K for each defect and 2meV/k for O_2[48,60].

Besides point defects, defect complexes and associates have also been reported to be important in alumina[61,62]. The formation of defect clusters could reduce the

concentration of individual point defects, and the overall transport can be determined by defect clusters.

Table 2.2 Schottky and Frenkel formation energies in alumina.

	Formation Energy per defect (eV)		
	Schottky (ΔH_S)	O Frenkel ($\Delta H_{F\text{-}O}$)	Al Frenkel ($\Delta H_{F\text{-}Al}$)
Kroger et al.	3.83	-	4.45
Matsunaga et al.	4.01	6.52	4.95
Hine et al.	4.05	6.61	4.48
Catlow et al.	5.14	8.27	7.09
Grimes et al.	5.86	5.79	6.30
Lagerlof et al.	5.17	4.87	6.59

2.5 Grain Boundary Diffusion in Alumina

Many researchers have studied grain boundary diffusion in alumina and there are still several critical unanswered questions. First, due to the difficulty of conducting Al isotope tracer diffusion experiments, the data of Al GB diffusivity is scarce. The relative magnitude between Al GB diffusivity and O GB diffusivity is unclear. Creep indicated that aluminum GB diffusion is slower than oxygen GB diffusion[63], while two-stage oxidation experiments showed that Al outward diffusion is comparable with O inward diffusion[10].

Second, although the data on O GB diffusion is extensive, there is a large discrepancy of several orders of magnitude between the results[24]. The discrepancy is not only due to different experimental conditions, but also comes from the different methods used to extract the data. O GB diffusivities calculated from oxidation experiments are usually larger than those extracted from isotope exchange with SIMS measurement.

Third, although the variability of O GB diffusivities have been noticed[64,65], the details on how a GB structure affects the Al and O diffusivity is still unknown.

Regardless of these open questions, it is widely agreed that doping can effectively change O and Al GB diffusivities in alumina. Y-doping has been found to reduce both O and Al GB diffusion in alumina by SIMS study[66], oxidation work[10] and creep tests[63]. A recent study using ^{26}Al isotope showed that Al GB diffusion is the same in undoped alumina and Y-doped alumina[67]. Their results contradict these many previous studies, which may be caused by problems during the production and determination of ^{26}Al[24].

Recent high temperature oxygen permeation experiments[5–9] showed oxygen GB diffusivity depends on P_{O_2} in both undoped and doped alumina. The authors used an

intrinsic point defect model to explain their results, an analysis that is contradictory to traditional thinking. As a highly stochiometric compound, the concentration of intrinsic nonstoichiometric generated defects is so low that the defect concentration in alumina should be determined by the impurity level. Using the formation energy reported by Kroger et al.[52], at the experimental condition of the oxygen permeation experiments, the oxygen vacancy concentration generated due to intrinsic is at the level of 0.01ppm, which is extremely low compared to the impurity level in the purest alumina powder, which is about 50ppm. The viability of applying an intrinsic model to grain boundary transport will be discussed in 5.1.4.2. Kitaoka et al.'s results also showed that Hf-doping has no effect on O GB diffusion[5–9], which conflicts with conventional wisdom and is a topic of this investigation.

2.6 Grain Boundary Complexions in Alumina

A grain boundary complexion is defined as an interfacial material or strata that is in thermodynamic equilibrium with its abutting phase(s)[68]. Grain boundaries exhibit phase-like behavior in which their structure, chemistry and properties may change discontinuously at critical values of thermodynamic parameters such as temperature, pressure and chemical potential. Therefore, grain boundaries can be treated as thermodynamically stable interfacial states. To differentiate these interfacial states from bulk phases, the term "complexion" has been introduced.

Dillon and Harmer studied grain growth behavior in alumina over a large range of temperatures and chemistries, and categorized different GBs in alumina into six discrete types of complexions with dramatically different GB mobilities and different corresponding structures[69]. Figure 2.7 shows the six distinct regimes of GB mobility in alumina associated with the six discrete corresponding complexions. Figure 2.8 shows examples of the grain boundary structures of the six types of complexions. They concluded that abnormal grain growth is the result of the coexistence of two or more different complexions. They found that Nd-doped alumina showed abnormal grain growth above 1500°C, and the GBs between small and small grains were type I complexion while the GBs along the abnormally large grains were type III complexion. Since complexion III has a much faster mobility than complexion I, abnormal grain growth occurred in the system.

Cantwell et al. reviewed the history and theory of grain boundary complexion transitions, their role in materials processing and their effect on materials properties[68]. They also summarized the techniques to characterize grain boundary complexions. Broadly speaking,

the techniques can be divided into direct characterization techniques, which permit visualization of the grain boundary structure and chemistry as well as quantification of compositional profiles across the grain boundary, and indirect characterization techniques, which measure changes in properties that depend upon grain boundary structure and chemistry, e.g. mobility, diffusivity, cohesive strength, and electrical and thermal properties. No single method, whether direct or indirect, can fully characterize a grain boundary complexion. The best approach to characterizing grain boundary complexion transitions is to use a combination of techniques.

Complexions can undergo transitions, and complexion transitions are the root cause of a wide variety of materials phenomena, such as abnormal grain growth, GB embrittlement and activated sintering[68,70–73]. By better understanding and controlling GB complexion transitions, it will be possible to advance the science of GB complexion engineering and develop new materials with novel behavior and dramatically improved properties.

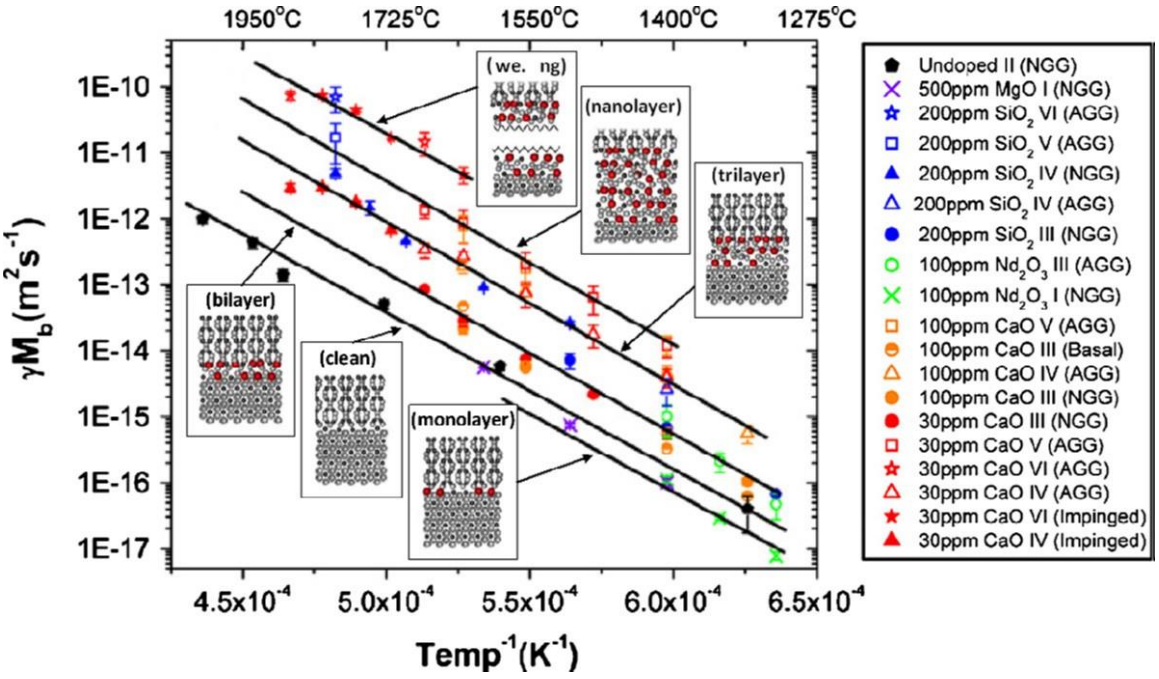

Figure 2.7 Grain boundary mobility in doped and undoped alumina, showing six distinct regimes of mobility corresponding to the six discrete complexions which are shown schematically. The grain boundary mobility were plotted versus inverse temperature for undoped, 30 ppm calcia-doped, 100 ppm calcia-doped, 200 ppm silica-doped, 100 ppm neodymia-doped and 500 ppm magnesia-doped alumina[69].

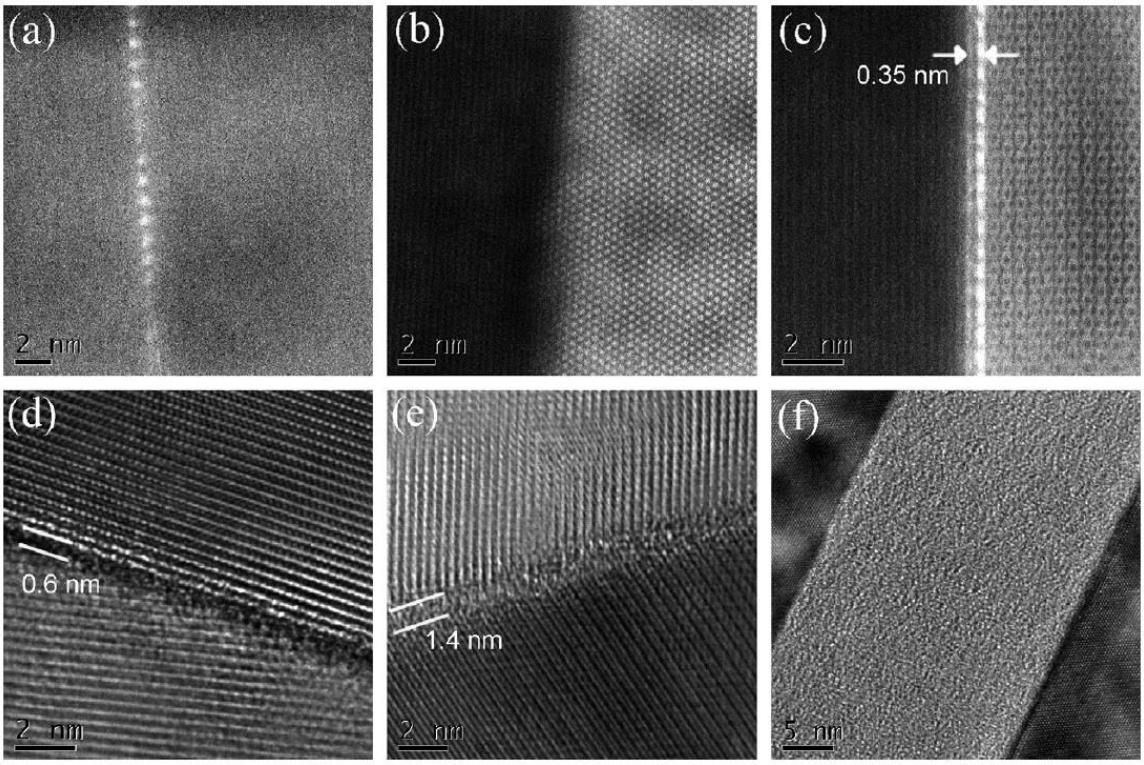

Figure 2.8 High-angle annular dark-field scanning transmission electron micrographs of the six corresponding complexions shown Figure 2.7. (a) complexion I, (b) complexion II and (c) complexion III, and high-resolution transmission electron micrographs of (d) complexion IV, (e) complexion V and (f) complexion VI. Complexions I, II and III are not directly differentiable by HRTEM. Bright spots in the HAADF-STEM images indicate the presence of neodymium. Complexion I shows sub-monolayer adsorption, complexion II shows no segregation and complexion III shows bilayer adsorption where the width of the boundary is 0.35 nm. Complexion IV shows a 0.6 nm disordered layer (multi-layer adsorption), complexion V is a ~1.5 nm intergranular film and complexion VI contains a thicker wetting intergranular film that may have arbitrary thickness with complexion at the liquid/solid interfaces[69].

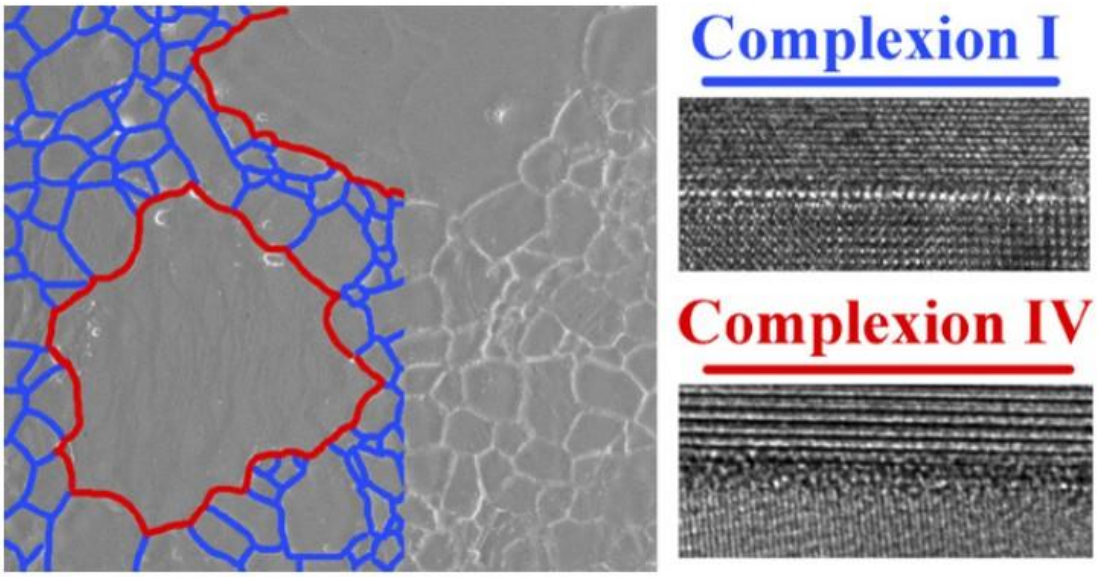

Figure 2.9 Schematic showing grain boundaries traced with colors corresponding to their complexion types[69].

CHAPTER 3 STATEMENT OF PURPOSE

The purpose of this study is to understand the grain boundary transport mechanisms associated with oxidation behavior in alumina. The current work studied the effect of oxygen partial pressure on the grain boundary transport in alumina, and the effect of Hf-doping on the grain boundary transport in alumina at different temperatures.

There are two objectives of the first part of the current study. The first is to determine the dependence of grain boundary transport on oxygen partial pressure in alumina. The second is to understand how oxygen partial pressure and point defect chemistry affects grain boundary transport in alumina. This will be accomplished by measuring transport in polycrystalline alumina under P_{O_2} from 10^{-10} to 10^{-18}, and comparing the measured results with predictions from different point defect models.

The objectives of the second part of this study are determining the effect of Hf-doping on the oxidation behavior in alumina at different temperatures, and understanding the mechanism by which Hf-doping retards grain boundary transport in alumina. Oxidation rates will be measured at different temperatures. Grain boundary structures in Hf-doped alumina will be characterized and correlated with the results.

CHAPTER 4 EXPERIMENTAL PROCEDURE

This chapter describes the experimental techniques and procedures employed to prepare the samples and acquire the data. It includes powder processing, sample preparation and microstructure characterization. The aim of this chapter is to provide adequate procedural details for an independent researcher to reproduce the experimental results.

4.1 Labware Cleaning

For all the powder or samples with different composition, different sets of labware were used to avoid cross contamination. The labware which had contact with any powder or sample during the processing steps were cleaned before being used. The cleaning was conducted in a clean room. Chemicals were used in a fume hood (Hamilton Laboratory Solutions, Manitowoc, WI) to clean the labware. The cleaning procedure is listed below:

1. The labware was rinsed with deionized (D.I.) water, which is purified tap water by Thermo Scientific™ Barnstead™ E-Pure™ filter (Thermo Fisher Scientific, Waltham, MA) with resistivity above 10×1023Ω·cm. Kimwipes (Kimberly-Clark, Irving, TX) were sued to wipe off any substance on the surface.
2. The labware was soaked in aqua regia (a mixture of 3 parts hydrochloride aid (Merck Millipore, Billerica, MA) and 1 part nitric acid (Merck Millipore, Billerica, MA)) for 1h to remove inorganic contamination. For the labware which were used to contain powder, only their inside surfaces were cleaned. The used aqua regia was poured into a glass bottle for waste disposal and the bottle was labeled. All the lids of the containers with aqua regia were kept ajar because this acid evolves gas that may cause a closed container to rupture.

3. The labware was rinsed with D. I. water three times and soaked in D. I. water for 12h to remove residual aqua regia.
4. The labware was soaked in trichloroethylene (Alfa Aesar, Tewksbury, MA) for 6h to remove organic contamination. The used trichloroethylene was poured into a glass bottle for waste disposal and labeled.
5. The labware was soaked in acetone (Pharmco-Aaper, Brookfield, CT) for 6h to remove residual trichloroethylene. The used acetone was poured into a sink with water tap on.
6. The labware was soaked in ethanol (Decon Laboratories, Inc., King of Prussia, PA) for 6hr to remove residual acetone. The used ethanol was poured into a sink with tap water on.
7. The labware was rinsed with D. I. water three times and soaked in D. I. water for 6h to remove residual ethanol.
8. The labware was dried in a clean room with Kimwipes wrapped to avoid contamination.

The cleaned labware were stored in Ziploc® bags (S. C. Johnson & Son, Racine, WI) for future use.

4.2 Powder Processing

Procedures such as doping, and drying were performed inside a clean room. 250ml low-density polyethylene (LDPE) bottles (Thermo Fisher Scientific, Waltham, MA) were used as containers for milling powder due to their translucency for visibility and chemical resistance to organic solvents and aqua regia. Alumina milling balls (Union Process, Akron,

OH) with 99.9% purity and 3mm diameter were used as milling media. High purity alumina milling media was used because it is known that some of the milling media is incorporated in the powder during milling. PTFE strainers, PTFE funnels and 1000ml PTFE jars (Savillex, Eden Prairie, MN) were used for transferring and containing powder due to their translucency for visibility and chemical resistance to organic solvents and aqua regia. Magnetic stir bars coated by PTFE (Thermo Fisher Scientific, Waltham, MA) were used during drying to assure the uniformity of mixing. 200 proof ethanol (Decon Laboratories, Inc., King of Prussia, PA) was used for powder mixing.

4.2.1 Alumina-Nickel Spinel Composite

$NiAl_2O_4$ doped Al_2O_3 powder was prepared by mixing NiO powder (Alfa Aesar, Tewksbury, MA) with 99.998% purity and Al_2O_3 powder (AKP-HP, Sumitomo Chemical Co., Ltd., Tokyo, Japan) with 99.995% purity and average particle size of 0.45μm. 1.5wt% NiO powder was added to yield 0.5vol% Ni on reduction, the metal content utilized previously in the Ni-marker particle experiments[15,16]. NiO powder was first ball milled in ethanol for 24h to reduce its particle size. About 30vol% milling balls were added to the bottle. Then Al_2O_3 powder was added to the bottle and milled for another 24h to break agglomerates and get a uniform mixture. After that, the slurry was poured into a PTFE jar with a magnetic stir bar. A PTFE strainer was used to separate the milling balls from the slurry. The bottle and the milling balls were rinsed three times using 200 proof ethanol, which was collected into the PTFE jar containing the slurry. The PTFE jar was then put on a hot plate with stirring and low heat on. A filter paper (GE Healthcare Bio-Sciences, Pittsburgh, PA) was put on top of the jar to avoid contamination from the environment but

allow ethanol to evaporate. The whole setup was placed in the fume hood in the clean room. Once the powder was dry, it was collected into a Ziploc bag, which was then put into a second Ziploc bag. A marble rolling pin and cutting board were used to roll over the bags to break soft agglomerates. The powder was then placed in an alumina crucible (CoorsTek, Inc., Golden, CO) with 99.8% purity, which was embed in pure alumina powder in a larger alumina crucible to reduce contamination from the box furnace. The crucibles were placed in a box furnace (L & L Special Furnace Co., INC., Aston, PA) and the powder was calcined at 750°C for 6h. Calcining the powder removed unevaporated ethanol and any organics that may have been picked up from the lab-ware or the atmosphere. The calcined powder was again placed in double Ziploc bags and rolled to break up any agglomerates that formed during calcination. At this point, the powder was ready for consolidation and sintering.

4.2.2 Hf-doped Alumina-Nickel Composite

$HfO(NO_3)_2$ (Alfa Aesar, Tewksbury, MA) with 99.9% purity was used to prepare HfO_2 doped samples. 500ppm $HfO(NO_3)_2$ in molar fraction was added to compare the results with previous works[16]. This step was conducted right after adding alumina powder into the milling bottle. The sample was dried and calcined by following the same procedure as mentioned in 4.2.1.

4.3 Sintering

In order to obtain different microstructure, different sintering methods were used. Alumina-$NiAl_2O_4$ composites were sintered in air to maintain the oxidized form of Ni. Cold isostatic pressing (CIP) and pressureless sintering was used to sinter these samples. HfO_2 doped

alumina-Ni composites were sintered in a reducing atmosphere to obtain metallic Ni dispersed in the samples. The formation of Ni in the samples required the sintering temperature to be below 1455°C, the melting temperature of Ni. At this temperature, one of the assisted sintering methods, Sparks plasma Sintering (SPS), was used to sinter these samples.

4.3.1 Cold Isostatic Pressing and Pressureless Sintering

The $NiAl_2O_4$ doped Al_2O_3 powder was cold isostatic pressed first to achieve higher packing density and better packing homogeneity. High packing density shortens the densification time. Inhomogeneity could result in large pores, which could remain in the microstructure during the sintering process. The calcined powder was first formed into a pellet using a set of alumina die and punches. Then the pellet was put into a nitrile glove (VWR International, LLC., Radnor, PA), which was then put into a natural latex rubber bag (Trexler Rubber Company Inc., Ravenna, OH). After that, the rubber bag was vacuumed and sealed. The sealed rubber bag was put into the cold isostatic press (Fluitron, Inc., Ivyland, PA) and held at about 277 MPa (40,000 psi) for 10 min. After the press, the pellet was taken out of the rubber bag and the glove carefully to avoid contact with the pressing oil.

The pellet was placed into an alumina crucible and sintered in a 1700 Series box furnace (CM Furnaces Inc., Bloomfield, N.J.). The pellet was put in a double crucible assembly as mentioned in 4.2.1. A new set of crucibles were used to avoid the contamination between furnaces. The assembly was placed in a box furnace for sintering. The furnace was set to ramp up at 5°C/min to 1600°C, hold at 1600°C for 5 h, and ramp down at 5°C/min to room temperature.

4.3.2 Spark Plasma Sintering

SPS applies both pressure and electric field to samples to assist sintering. It could effectively reduce the sintering temperature and time to achieve dense microstructure with relatively small grain size. SPS Model 10-4 (Thermal Technology Inc., Santa Rosa, CA) was used in this study. Graphite dies (Thermal Technology Inc., Santa Rosa, CA) with 20mm inside diameter and 50 mm outside diameter plus a pyrometer hole were used. The operation procedure of the SPS is showed below:

1. A piece of graphite foil (Alfa Aesar, Ward Hill, MA) with 99.8% purity was wrapped to just cover the inside surface of a graphite die. The use of the graphite foil could avoid diffusion bonding between the powder and the die, and allow the die to last longer.
2. A graphite punch was inserted into the die. A circular graphite foil was placed on the surface of the punch for the same purpose mentioned in step 1.
3. The die was then filled with powder. The optimized amount of powder was between 6g to 8g for alumina. The number was based on the calculation from the desired sample thickness. After cutting off the contaminated surfaces, 2-3mm thickness was left. The reason for sintering a relatively thin sample is to avoid nonuniform stress field developing in the sample, which may result in nonuniform microstructure in the sample.
4. A second piece of circular graphite foil was placed on top of the powder. Another graphite punch was used to manually press the powder so both punches had parts inside the die. Figure 4.1 shows a schematic diagram of the assembly.

5. The assembly was then pressed in a uniaxial hydraulic press at 50MPa. This step was to assure that the assembly could be pressed up to 50MPa in SPS. A uniaxial hydraulic press with a safety cover should be used.
6. The assembly was then covered with a graphite foam to reduce heat loss during the heat treatment. The foam should not cover the hole in the die, which was used for temperature reading.
7. The assembly was then placed into the SPS and its position was adjusted so the hole in the die aligned with the pyrometer. An initial load of 10MPa was applied.
8. The chamber was vacuumed to a pressure below 7×10^{-3}Pa (5×10^{-5} Torr). Then 5% H_2-N_2 mixture was flowed through the chamber before starting the program.
9. The temperature was set to ramp up to 650°C and hold for 3 h in the flowing gas. $NiAl_2O_4$ was reduced to Ni in the reducing atmosphere. At the end of the holding stage, the flowing gas was closed and the chamber was vacuumed again.
10. After the holding stage, the temperature was set to ramp up to 1400°C, and the pressure was set to ramp up to 40 MPa at the same time. The temperature and pressure was held for 15 min, and then ramped down quickly to room temperature and 10 MPa, which was the initial condition.

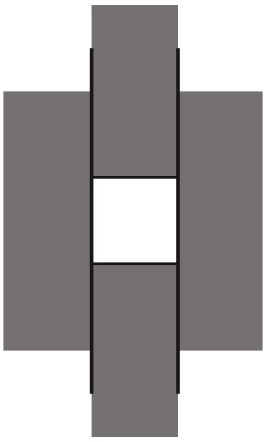

Figure 4.1 Schematic diagram of the assembly of powder in an SPS die set.

4.4 Cutting, Polishing and Cleaning

Most samples needed to be cut, polished and cleaned for further analysis.

4.4.1 Cutting

Samples were cut into small pieces for characterization and further heat treatment. Cutting was performed using a high-speed saw (Struers Inc., Cleveland, OH) fitted with a diamond-coated blade (Norton | Saint-Gobain Abrasives, Worcester, MA). For all the as-sintered samples, a layer with about 2mm thickness was cut off from the top, bottom and sides to remove the region which may have been contaminated from the heat treatment process. Then the samples were cut into rectangular pieces with dimension of 3mm × 3mm × 2mm approximately.

4.4.2 Polishing

Samples were polished prior to heat treatments in which surface effect needs to be eliminated, including oxidation, reduction and GB groove annealing. Polishing is also necessary before characterizing samples in microscopes.

Samples were first mounted using epoxy, which was a mixture of 10 parts resin and 1 part hardener (Pace Technologies, Tucson, AZ) in weight. Then the mounts were placed under vacuum until there were no bubbles in the epoxy. The bubbles in the epoxy would form pores on the polishing surfaces of the cured epoxy. These pores could be sinks for particles, and bring large particles into the next steps and harm the polishing results. After vacuum, the mounts were placed in a hood for 24h for curing. The curing time can be

shortened by placing the mounts in an oven for 8h at 100°C. Once the mounts were cured, the samples were polished following the procedure below:

1. The edges of samples were beveled first to avoid damage to the polishing cloth.
2. 3 samples were assembled on a holder for an automatic polisher, Saphir 550 (Mager Scientific, Inc., Dexter, MI).
3. 400-grit SiC paper was used to grind samples to remove the epoxy on the surface of samples and damaged surface layer due to cutting. The goal of each step of grinding and polishing is to remove the damage from the previous step. Switching to the next step using smaller abrasive particles was undertaken when there were no signs of improvement in the surface quality under an optical microscope using the current step. After each step, the samples were cleaned under running water using cotton and dried under a hand dryer to prevent cross contamination between each step.
4. Then samples were polished on a no nap polishing cloth, MD-DAC (Struers Inc., Cleveland, OH), with 15µm diamond suspension, followed by using 9µm, 3µm and 1µm diamond suspension (WENDT DUNNINGTON, Royersford, PA). Different polishing cloths were used for suspensions with different particle sizes to avoid cross contamination.
5. Vibrating polishing was followed for samples which needed to be characterized using EBSD, a technique that needs a better polishing quality of surfaces. A vibratory polisher, Vibromet 1(Buehler Ltd., Lake Bluff, IL), was used with 0.05µm colloidal silica (Remet, Utica, NY) to produce a better surface quality.

After polishing, mounts were immersed in boiled water for 20min to soften the epoxy. Then samples were taken out using tweezers carefully without damaging the polished surface.

4.4.3 Cleaning

The polished samples were placed in glass bottles with acetone and cleaned in an ultrasonic cleaner for 30min. This step was repeated by using ethanol and D.I. water. After cleaning, samples were dried under an I.R. lamp in the clean room.

4.5 Annealing

Samples were annealed at different conditions by using different furnaces. The CM box furnace was used to anneal samples in air. A M60 furnace (Centorr/Vacuum Industries, Nashua, NH) was used to anneal samples in reducing atmosphere by flowing 5% H_2-N_2 mixture. A Lindberg/Blue M™ 1700°C Tube Furnace (Lindberg/MPH, Riverside, MI) was used to conduct both oxidation and reduction experiments.

4.5.1 Oxidation

The setup of the tube furnace is illustrated in Figure 4.2. HfO_2 doped Al_2O_3-Ni samples were placed in an alumina crucible, which was then put on an alumina rectangular tray. The assembly was slid into the tube furnace using a taper ruler. The samples were placed at the center of the furnace. A type B thermocouple (OMEGA Engineering, INC., Norwalk, CT) was placed at the same position to measure the temperature. Prior to starting the program, the tube was pumped down to below 20mtorr and filled by extra dry pure O_2 (AIRGAS, INC., Radnor, PA). This step was repeated twice. Then pure O_2 was flowed in

at around 200cm^3/min. The annealing was conducted in the temperature range of 1095°C to 1400°C.

It took several months to oxidize samples at 1095°C, 1120°C and 1150°C. These samples were put into the furnace at different locations while annealing samples at 1150°C to save experimental time. The locations were chosen based on a temperature-location profile measured before the runs. The samples were placed at the exact position carefully. When the annealing at 1150°C was finished, the samples were taken out and the annealing at 1120°C and 1095°C was continued.

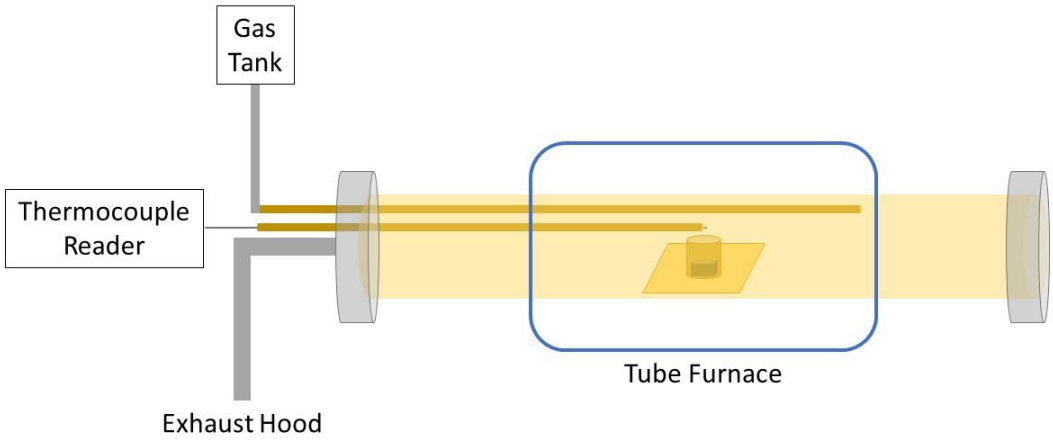

Figure 4.2 Schematic diagram of the setup of the tube furnace for oxidation and reduction experiments.

4.5.2 Reduction

Al_2O_3-$NiAl_2O_4$ samples were reduced at 1400°C using the same setup of the tube furnace as mentioned in 4.5.1. Different gas mixtures were used to create reducing atmospheres with different P_{O_2}.

For each gas mixture, P_{O_2} was determined by thermodynamic calculation using composition provided by the manufacturers. At 1400°C, the annealing temperature, the following two reactions were both assumed to reach equilibrium.

$$2H_2 + O_2 = 2H_2O \quad (4.1)$$

$$2CO + O_2 = 2CO_2 \quad (4.2)$$

The P_{O_2} was calculated by solving the following two equations simultaneously.

$$K_{H_2\text{-}H_2O} = \frac{P_{H_2O}}{P_{H_2}^2 \cdot P_{O_2}} \quad (4.3)$$

$$K_{CO\text{-}CO_2} = \frac{P_{CO_2}}{P_{CO}^2 \cdot P_{O_2}} \quad (4.4)$$

$K_{H_2\text{-}H_2O}$ and $K_{CO\text{-}CO_2}$ are the equilibrium constants of reactions (4.1) and (4.2). At 1400°C, $K_{H_2\text{-}H_2O}$=3.84×10^9 and $K_{CO\text{-}CO_2}$=6.20×10^8 respectively[60]. By assuming the amount of O_2 reacted in (4.1) and (4.2) is x and y respectively, the amount of each gas can be calculated in terms of x, y and the initial composition. Then these numbers were substituted into Eq. (4.3) and (4.4) to calculate the equilibrium P_{O_2}. It can be proved that the solution exists and is unique. When the amount of one component was too low to be measured, the

maximum amount was given by the manufacturer. In this case, the maximum and minimum P_{O_2} of that gas were both calculated using the limiting condition. The average of the maximum and minimum was used as the P_{O_2} for that gas, and the half of the difference between the maximum and minimum was used as the error. Table 4.1 lists the composition of each gas mixture used for reduction experiments and its corresponding P_{O_2} at 1400°C.

Table 4.1 Composition and equilibrium P_{O_2} at 1400°C for each gas mixture used for reduction experiments.

	H_2	O_2	H_2O	CO	CO_2	P_{O_2}
5% H_2 in N_2	4.82%	<0.2ppm	6.1ppm	0.17ppm	<0.1ppm	$(4.5\pm0.4)\times10^{-18}$
5% H_2-15ppmO_2 in N_2	5%	12.5ppm	0.94ppm	<0.1ppm	<0.1ppm	$(7.0\pm0.1)\times10^{-17}$
6600ppmH_2-20ppmO_2 in N_2	6570ppm	16.8ppm	0.68ppm	<0.1ppm	<0.1ppm	$(7.2\pm0.1)\times10^{-15}$
700ppmH_2-20ppmO_2 in N_2	700ppm	16.4ppm	0.59ppm	0	0.1ppm	$(6.5\pm0.1)\times10^{-13}$
100ppm H_2-20ppm O_2 in N_2	106ppm	21.5ppm	0.73ppm	<0.1ppm	0.35ppm	$(1.3\pm0.1)\times10^{-10}$
200ppm CO-50ppm CO_2 in N_2	<2ppm	0.3ppm	1.0ppm	201ppm	47ppm	$(9.2\pm0.2)\times10^{-11}$

4.6 Characterization

Various characterization techniques were used to obtain properties of samples for further analysis. This section explains the experimental procedure while the results will be shown in the next chapter.

4.6.1 Density Measurement

Two methods were used to determine the density of samples. Archimedes' method was used for samples with weight higher than 10g. The measurement error is negligible for heavier samples. An imaging method was used for lighter samples.

Archimedes' method measured the bulk density, ρ, of samples. A microbalance (H51 Metier, Switzerland) was used to measure all the weights that were used to calculate ρ. First, a sample was dried thoroughly and its dry weight, W_d, was measured first. Then the sample was emerged into D.I. water with 0.01% Brij (Thermo Fisher Scientific, Waltham, MA) in a glass beaker (Corning Inc., Corning, NY). The addition of Brij reduced the surface energy of water and allow water to go into the open pores of the sample easier. The beaker was then put into a desiccator and vacuumed for 3h. This step also helped the water go into the open pores of the sample. After that, the immersion weight of the sample, W_i, was measured while the sample was tied by a very thin and light finishing string. The sample was then taken out of the water and immediately wiped with of a piece of wet Kimwipe. This was meant to remove water from the surface of the sample while keeping the water within the open pores. Then the wet weight of the sample, W_w, was measured. The temperature of the water was recorded to calculate the density of the water. The bulk

density of the sample was calculated by Eq. (4.5). The relative density of the sample was calculated by dividing the bulk density by the theoretical density of alumina, 3.97g/cm^3.

$$\rho = \frac{W_d}{W_w - W_i}\rho_{H_2O} \qquad (4.5)$$

For a small sample, the measurement error in Archimedes' method was relatively large. The imaging method was used to calculate sample density for small samples. The sample was polished at least down to 1μm. Then 10 SEM images were taken from different areas of the polished surface. After that, ImageJ was used to pick out all the pores in each image and calculate the area fraction of the pores for that image. The average and the standard deviation of the fraction for all the 10 images was used as the average porosity and the error of the sample[74].

4.6.2 Grain Size Measurement

The Linear Intercept Method was used to measure the grain size of the samples in oxidation and reduction experiments. After oxidation or reduction, the surface of samples showed apparent GB grooves, which could be used to identify the position of GBs. 10 SEM images were taken from different areas for each sample. Each image was then superimposed by 10 lines with same length, *l*, but random orientation and position. Figure 4.3 shows an example of an SEM image superimposed by 10 random lines for grain size measurement. The number of GBs that intercepts each line, n_i, was counted. ASTM Standard Test Methods for determining average grain size has a different definition of intercepts. But the method used by previous studies[15,16] was adopted in order to compare the results directly. For each sample, at least 500 intercepts were counted totally for statistical consideration. The average grain size, *G*, and its error, Δ*G*, were calculated using Eq. (4.6) and Eq. (4.7).

$$G = \frac{\sum_i \frac{1.5l}{n_i + 1}}{100} \quad (4.6)$$

$$\Delta G = \sqrt{\frac{\sum_i (\frac{1.5l}{n_i + 1} - G)^2}{99}} \quad (4.7)$$

1.5 was used as a conversion factor to estimate the spatial diameter based on 2-D measurement by assuming grains are spheres with the same size[75].

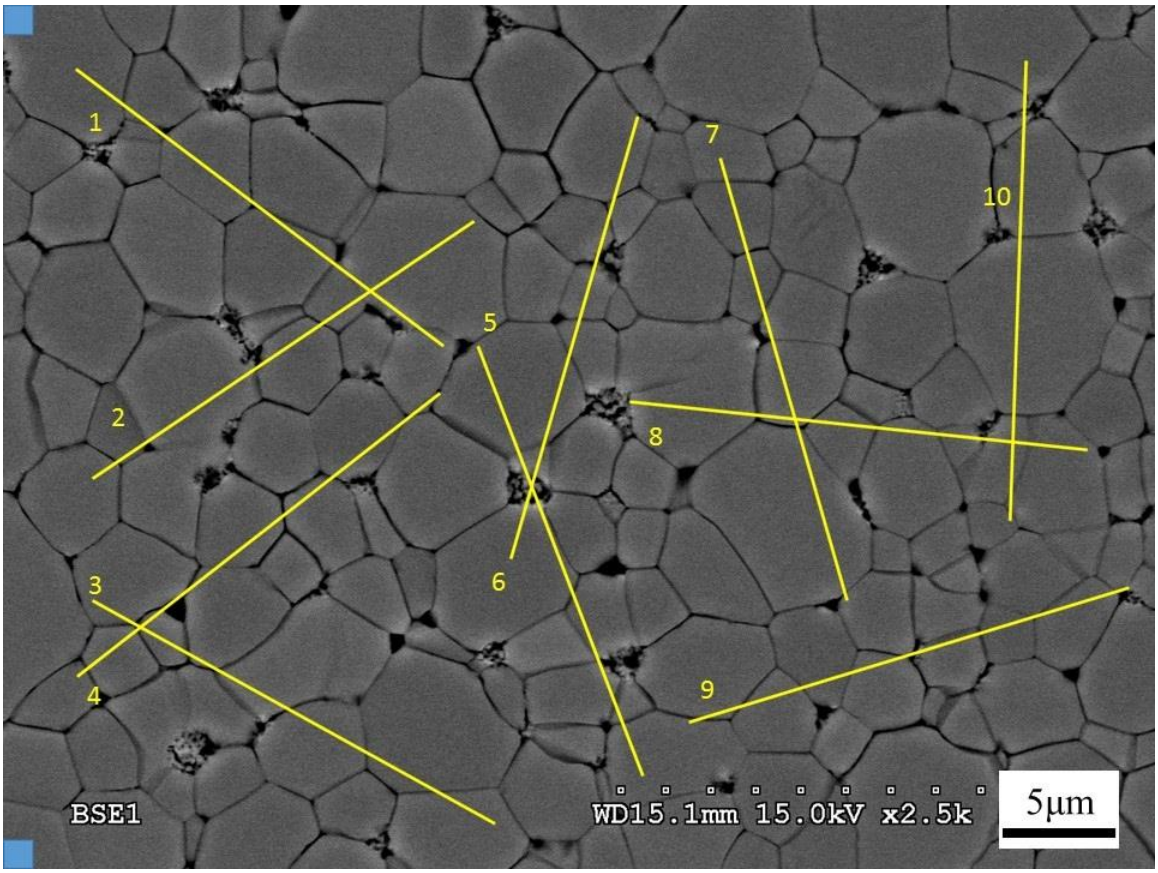

Figure 4.3 SEM backscattered electron (BSE) image of the surface of a sample superimposed by 10 random lines for grain size measurement.

4.6.3 Diffusion Depth Measurement

After oxidation or reduction, the diffusion depth was measured for each sample. First, a sample was cut along the direction perpendicular to the polished surface. The as-cut surface, which is the cross-section of the sample, was polished by following the procedure mentioned in 4.4.2. The geometry is shown in Figure 4.4. Then the polished surface was looked at in SEM to measure the diffusion depth. About 10 images were taken for each sample along the edge shared by the polished cross section and the polished surface. To increase the accuracy of the measurement, each image was divided into several regions. The number of regions varies from 2 to 5, depending on the length of the region shown in the image. For each sample, at least 30 regions were examined to calculate the diffusion depth. In each region, two lines were drawn so that there were no reacted particles above the top line, and all the particles were reacted below the bottom line. In a few regions, the positions of the two lines were switched, which means that there were no particles between the two lines. Then the distances between the two lines to the edge of the sample were measured by using ImageJ[76], and the average of the two distances, x_i, was used as the diffusion depth for this region. The average diffusion depth, x, and its error, Δx, were calculated using the following equations.

$$x = \frac{\sum_i x_i}{N} \qquad (4.8)$$

$$\Delta x = \sqrt{\frac{(x_i - x)^2}{N - 1}} \qquad (4.9)$$

where N is the number of the regions that has been examined for the sample.

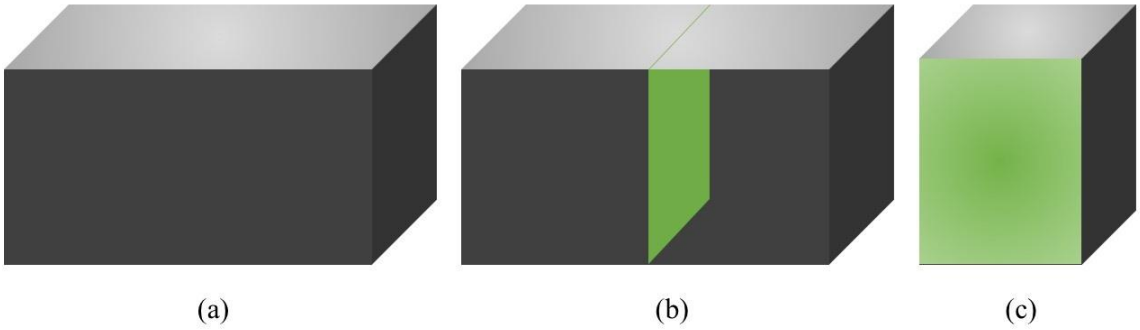

Figure 4.4 Schematic diagram showing the procedure of sample preparation for diffusion depth measurement. The top surface of the sample was polished before annealing. (a) After annealing; (b) Cut across the polished surface; (c) Polish the cross section.

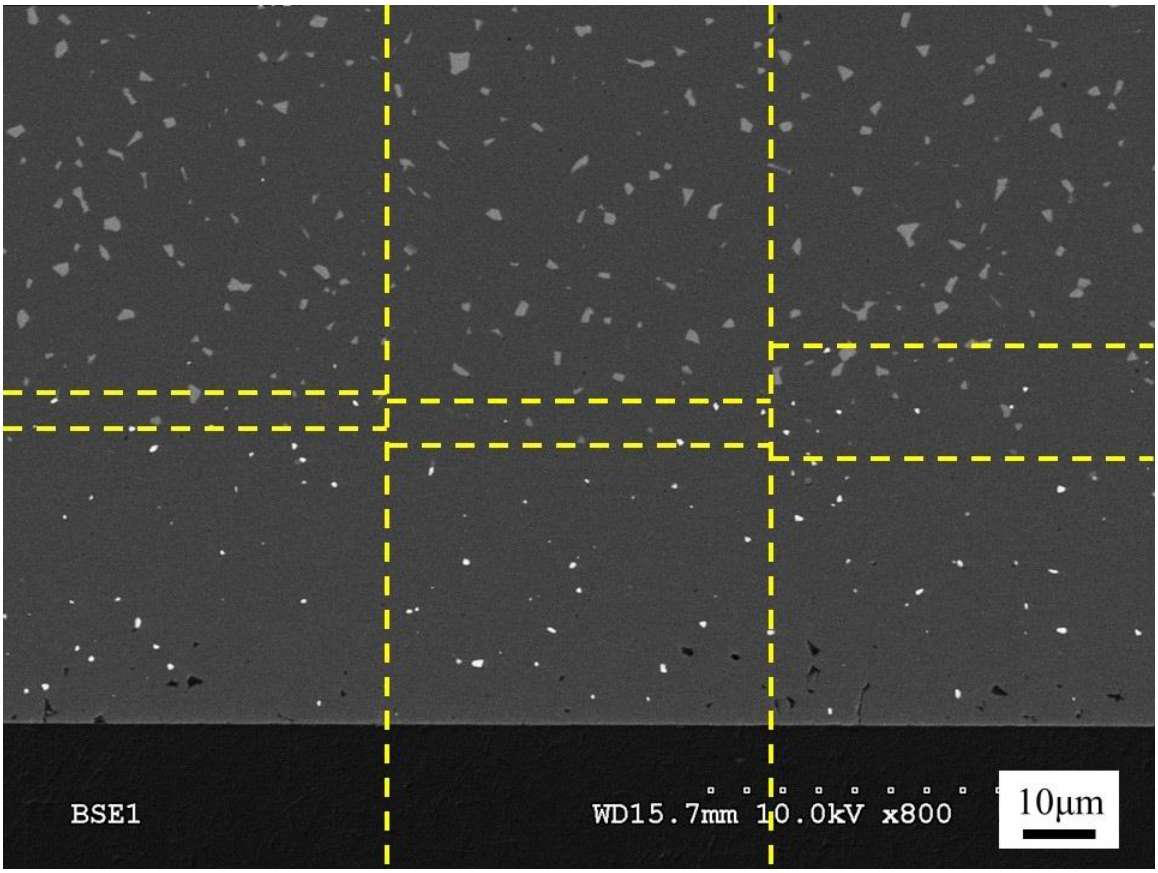

Figure 4.5 SEM image of a cross section of a sample divided into 3 regions for diffusion depth measurement.

4.6.4 TEM Sample Preparation by FIB

TEM samples were prepared using a focused ion beam (FIB) (Scios™ DualBeam™, FEI, Hillsboro, OR) and NanoMill® (Model 1040, E.A. Fischione Instruments, Inc. Export, PA). The FIB was used to mill samples using Ga ions at 30kV and 5kV to make lamella shape sample for TEM. The NanoMill® was used to clean the damage on the samples from FIB. The main procedure is described as below:

1. A layer of platinum with about 2μm thickness was deposited on an area of interest. The platinum layer protected the part of the sample underneath from ion beam milling.
2. Two trenches were made on each side of the Pt using high current. A lamella was left between the trenches. Each side of the lamella was cleaned using lower current.
3. A J-cut was performed to prepare for the lift-out of the lamella. A complete cut through the sample is important for the next step.
4. The lamella was attached to the needle using Pt deposition. After that, the lamella was cut off from the sample and lifted out with the needle.
5. The lamella was attached to a molybdenum grid using Pt deposition. After that, the lamella was cut off from the needle.
6. Both sides of the lamella were cleaned alternatively until the lamella was electron transparent. Lower current and voltage of ions were used as the lamella became thinner. A sample with thickness less than 100nm is ideal for TEM characterization.
7. The grid was taken out of the FIB and put in the NanoMill®. After both sides of the sample were cleaned using Ar ions, the sample was ready for TEM characterization.

Figure 4.6 illustrates the steps involved in the preparation of TEM sample by FIB.

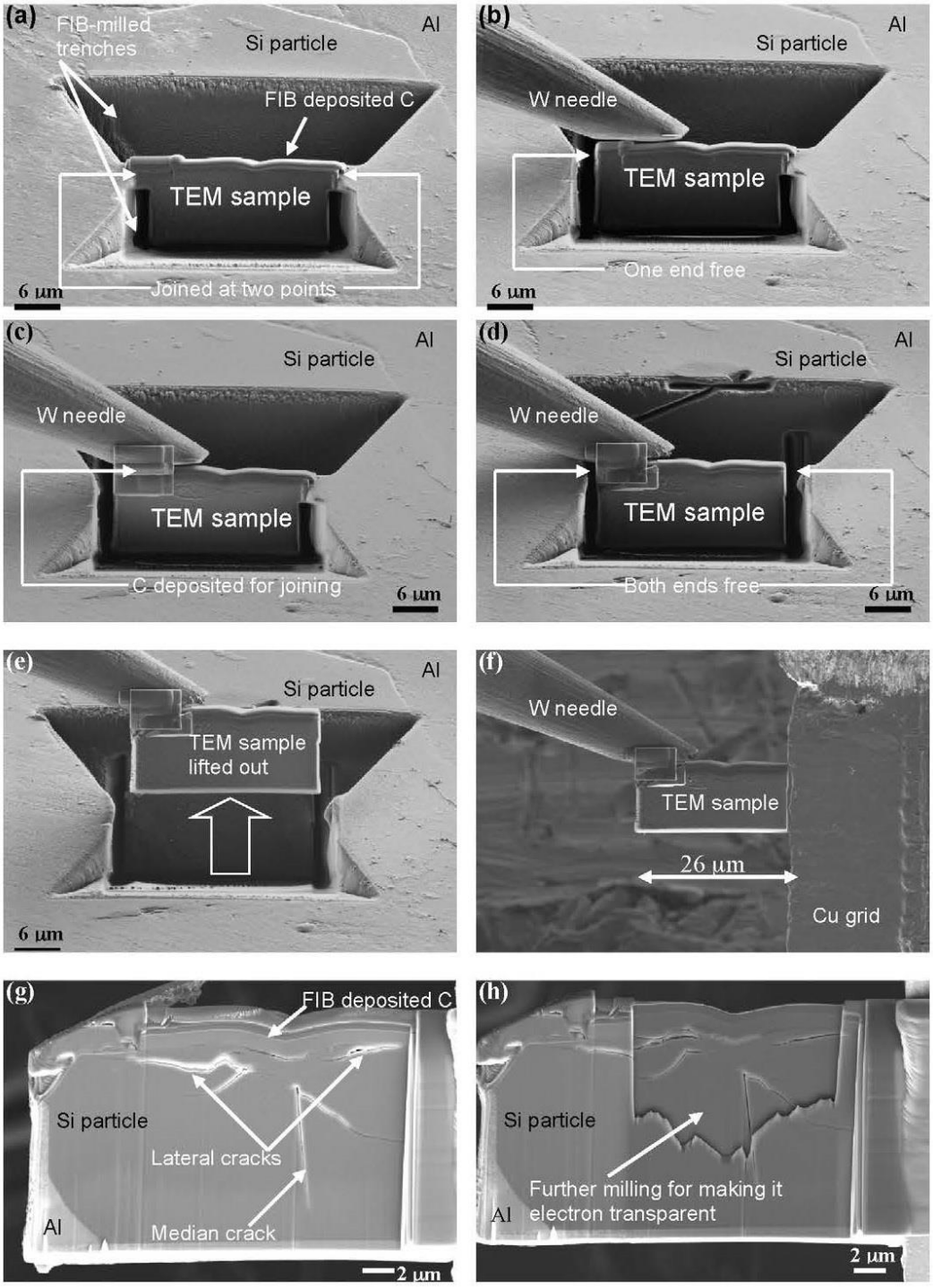

Figure 4.6 SEM images illustrating the steps involved in the preparation of TEM sample by FIB[77]. (a) Make two trenches; (b) Insert needle; (c) Attach the lamella to the needle; (d) Cut off the lamella from the sample; (e) lift out the needle with the lamella; (f) Attach the lamella to the grid; (g) Cut off the lamella from the needle; (g) Thin the lamella.

4.6.5 Grain Boundary Characterization by TEM

Grain boundary structures were characterized by using a JEOL 2000FX (JEOL USA, Inc., Peabody, MA) and JEM-ARM200F (JEOL USA, Inc., Peabody, MA). They were both operated at 200kV. JEM-ARM200F was equipped with a spherical aberration corrector, and has atomic resolution. TEM samples were checked by using JEOL 2000FX, and the structural and chemical information were characterized by using JEM-ARM200F.

In order to get the structural information of a GB, the sample was tilted to satisfy two conditions. The GB was closer to the edge-on condition, in which there was no projection of the adjacent grains on the GB. And one adjacent grain of the GB was tilted to a zone-axis condition, in which a lattice image could be obtained from the grain. Once these two conditions were both satisfied, images were taken to record the structure of this GB. High-Angle Annular Dark-Field (HAADF) STEM Imaging technique was used to study the segregation behavior of Hf at grain boundaries in alumina. This imaging technique is very sensitive to heavier elements. The scale of the HAADF image is proportional to the square of the atomic number of the elements. Hf (Z=72) can be easily detected in Al (Z=13) lattices.

To get the chemical information of a GB, the sample was tilted to the condition that GB satisfied the edge-on condition. After that, EDS was taken from the GB.

CHAPTER 5 RESULTS AND DISCUSSION

This chapter describes the experimental results and their implications. There are two parts in this chapter. The first is about the effect of oxygen partial pressure on the grain boundary transport in alumina (section 5.1). The second is about the effect of Hf-doping on the oxidation behavior in alumina. It focuses on the effect of Hf-doping at different temperatures. These results are described in section 5.2.

5.1 Effect of Oxygen Partial Pressure on Grain Boundary Transport in Alumina

The effect of P_{O_2} on GB transport in alumina was studied. This section shows the setup of the experiments used to measure the transport rate, the results of the reduction rates at different P_{O_2}, and the discussion about whether point defect chemistry could be applied to explain GB transport in polycrystalline alumina.

5.1.1 Experiment Setup

In order to measure the transport in alumina over a large range of P_{O_2}, reduction experiments, instead of oxidation experiments, were conducted. Figure 5.1 shows the schematic diagram of the experimental procedure. A dense alumina sample with Ni spinel particles was sintered first. The sample was then annealed in a reducing atmosphere. During reduction, $NiAl_2O_4$ particles were reduced to metallic Ni particles as shown in Eq. (5.1).

$$NiAl_2O_4 = Ni + Al_2O_3 + \frac{1}{2}O_2 \qquad (5.1)$$

By measuring the reduction depth, x, as a function of annealing time, the reduction rate constant was obtained. The experiments were conducted at 1400°C under six different reducing atmospheres with P_{O_2} from 1.3×10^{-10} to 4.5×10^{-18}. The detailed P_{O_2} information is shown in 4.5.2. Under each P_{O_2}, samples were annealed for different times to obtain the kinetic results.

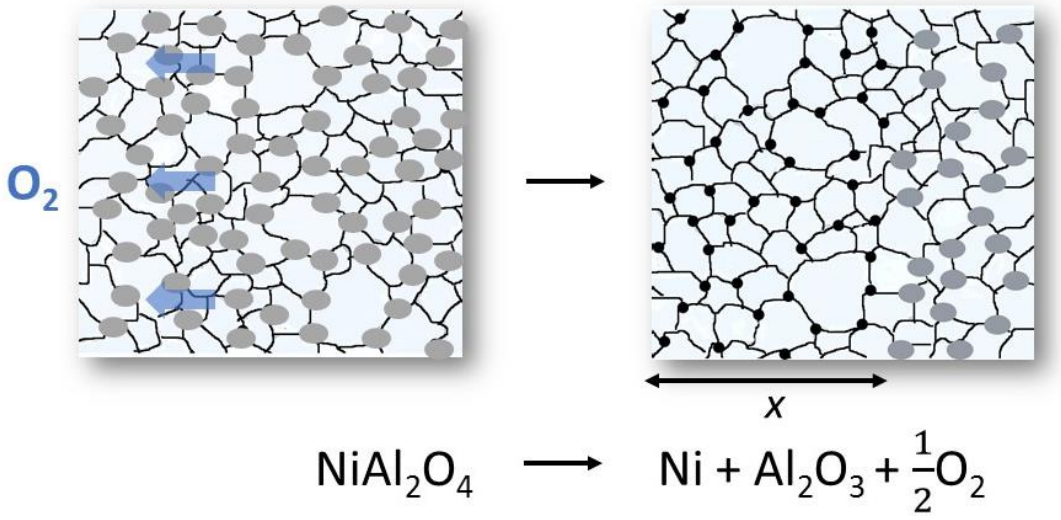

Figure 5.1 Schematic diagram of the reduction experiments.

5.1.2 Microstructure

Figure 5.2 shows an SEM image of an as-sintered sample. Before reduction, all the second phases were spinel particles, which were uniformly distributed in the alumina matrix. The volume fraction and the average size of the spinel particles were determined using a series of SEM images. The measured volume fraction was 3%, which is the same as the fraction calculated from the doping level. The average size of the spinel particles was 1μm.

Figure 5.3 shows an SEM image of the surface of a sample after reduction under $P_{O_2}=7.2\times10^{-15}$ for 10h. No abnormal grain growth behavior was seen in any of the samples in the reduction experiments. The average grain size for each sample at different annealing conditions is listed in Table 5.1. Minimal grain growth was observed during annealing at 1400°C. The grain sizes of all the samples were very close. For a given P_{O_2}, the representative grain size was taken as the average of the final gran size values for samples annealed for different times – these are listed in Table 5.2.

After reduction, spinel particles which were on the surfaces developed microporosity. Figure 5.4 shows an SEM image of a spinel particle that had undergone reduction. As confirmed by EDS, the bright dots are Ni particles. At the surface, the whole spinel particle was exposed to the reduction atmosphere, and there may be nucleation at multiple sites within the spinel particle, which could be a possible reason for the formation of this porous microstructure. Among the Ni particles formed after reduction, most of them were observed on GBs. This is probably because that the interfacial energy of a Ni particle at a GB is smaller than the interfacial energy of a Ni particle in the alumina lattice since there is more mismatch of alumina lattice at GBs.

Figure 5.5 shows SEM images of different samples annealed at 1400°C for 5h under different atmospheres. Compared with undoped alumina, the samples containing Ni spinel second phase exhibit deeper grain boundary grooves under both atmospheres. Furthermore, both undoped alumina and Ni spinel doped alumina samples have deeper grain boundary grooves following annealing in a reducing atmosphere compared to an oxidizing atmosphere. These observations are possibly due to the process of cation inward diffusion during reduction. Under low P_{O_2} condition, aluminum interstitials, $Al_i^{\cdot\cdot\cdot}$, may form on the surface by following Eq. (2.17). The aluminum interstitials at GBs diffuse inward and results in the deeper grooves. It is also possible that Ni spinel doping and atmosphere changed the surface energy and grain boundary energy of alumina, and resulted in different dihedral angles at the interface of grain boundary and surface.

Figure 5.6 shows an SEM image of the cross section of a sample reduced at 1400°C under $P_{O_2}=4.5\times10^{-18}$ for 5h. The reduction front can be easily located due to the distinct BSE contrast between spinel particles and Ni particles. In the region between the surface and the reduction front, Ni spinel particles were reduced to metallic Ni particles, which are shown as bright particles in the image. Compared with the porous microstructure formed on the surface after reduction, these solid Ni particles were formed inside samples. This may be because for a spinel particle at the GB, the transformation will start at the GB that is closest to the surface and move across during reduction. Ahead of the reduction front, Ni spinel particles maintained their oxidized form, which are shown as the particles in grey color. The reduction depth was measured to calculate the rate constant.

The magnified image of the reduction front shows that most of the spinel particles were fully reduced. This indicates that diffusion determines the overall reduction process, by following the analysis for oxidation experiments[15,78]. If reduction reaction determined the overall process, which means the rate of reduction reaction is lower than the rate of diffusion, partially reduced particles would be seen at different locations in the reduced region. If the rate of reduction reaction was comparable with the rate of diffusion, partially reduced particles would be seen near the reduction front. But both two cases were not consistent with the experimental results.

Figure 5.6 also shows that there is a higher degree of porosity in the reduced region compared to the non-reduced region. And there are much more pores near the surface of the sample. These pores could be formed during cutting and polishing when the Ni particles were pulled out. Assuming pull-out was not the reason for these pores, the formation of the pores could be due to the volume shrinkage from $NiAl_2O_4$ to Al_2O_3 and Ni. Based on molar volume of $NiAl_2O_4$ (39.34cm^3/mol), Ni (6.59cm^3/mol) and Al_2O_3 (25.55cm^3/mol)[60], the volume shrinks 18% from reducing $NiAl_2O_4$ to Ni and Al_2O_3. However, since much more pores were located near the surface, cation inward diffusion is more reasonable to explain the phenomena, which is consistent with the observations of GB grooving discussed above. During reduction, the sample lost O_2 as described in Eq. (5.1). This can be achieved by oxygen vacancies inward diffusion or/and aluminum interstitials inward diffusion. The discussion in 2.4 shows that oxygen interstitials and oxygen molecules are not favored in alumina. If oxygen vacancies outward diffusion was the only mechanism, the porosity would be uniform across the reduced region since aluminum ions stayed at their sites all

the time. The higher porosity near the surface is consistent with aluminum interstitials inward diffusion during reduction.

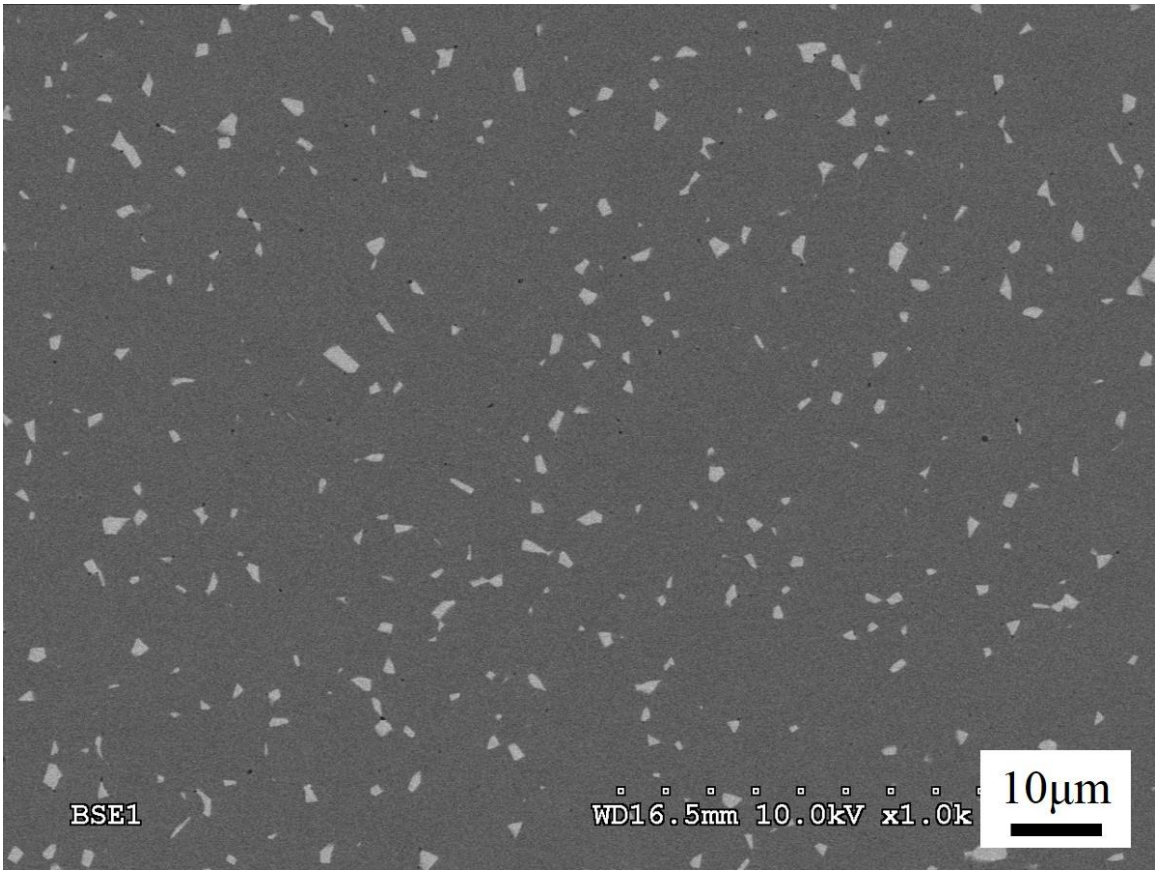

Figure 5.2 SEM BSE image of Ni spinel doped alumina sample sintered at 1600°C for 5h.

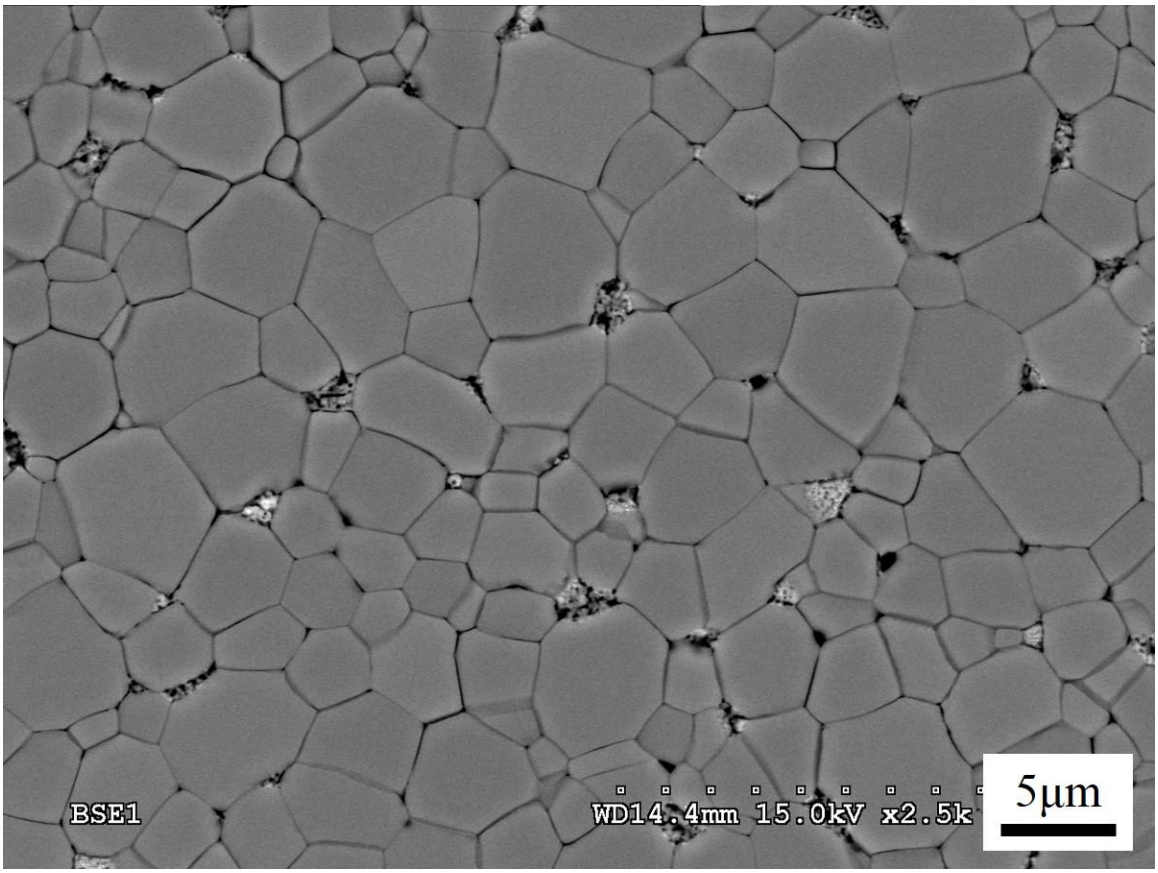

Figure 5.3 SEM BSE image of the surface of a sample reduced at 1400°C under $P_{O_2}=7.2\times10^{-15}$ for 10h.

Table 5.1 Grain sizes of samples after reduction under different P_{O_2} for different times.

P_{O_2}	Time (h)	G (um)
$(4.5\pm0.4)\times10^{-18}$	0.0	4.8±0.8
	4.1	4.8±0.8
	9.1	4.8±0.9
	19.1	4.7±0.8
$(7.0\pm0.1)\times10^{-17}$	0.0	4.6±0.7
	3.5	4.5±0.7
	8.5	4.6±0.9
	13.5	4.7±0.8
$(7.2\pm0.1)\times10^{-15}$	0.0	4.5±0.8
	3.5	4.8±0.8
	8.5	4.7±0.9
	15.5	4.7±0.8
$(6.5\pm0.1)\times10^{-13}$	0.0	4.5±0.8
	3.5	4.6±0.8
	8.5	4.7±0.8
	11.5	4.7±0.8
$(1.3\pm0.1)\times10^{-10}$	0.0	4.6±0.8
	4.2	4.5±0.8
	9.2	4.7±0.8
	19.2	4.6±0.9
$(9.2\pm0.2)\times10^{-11}$	0.0	4.8±0.8
	3.9	4.7±0.8
	8.9	4.9±0.9
	18.9	4.8±0.8

Table 5.2 Average grain sizes of samples after reduction under each P_{O_2}.

P_{O_2}	Average G (μm)
$(4.5\pm0.4)\times10^{-18}$	4.8±0.8
$(7.0\pm0.1)\times10^{-17}$	4.6±0.8
$(7.2\pm0.1)\times10^{-15}$	4.7±0.8
$(6.5\pm0.1)\times10^{-13}$	4.6±0.8
$(1.3\pm0.1)\times10^{-10}$	4.6±0.8
$(9.2\pm0.2)\times10^{-11}$	4.8±0.8

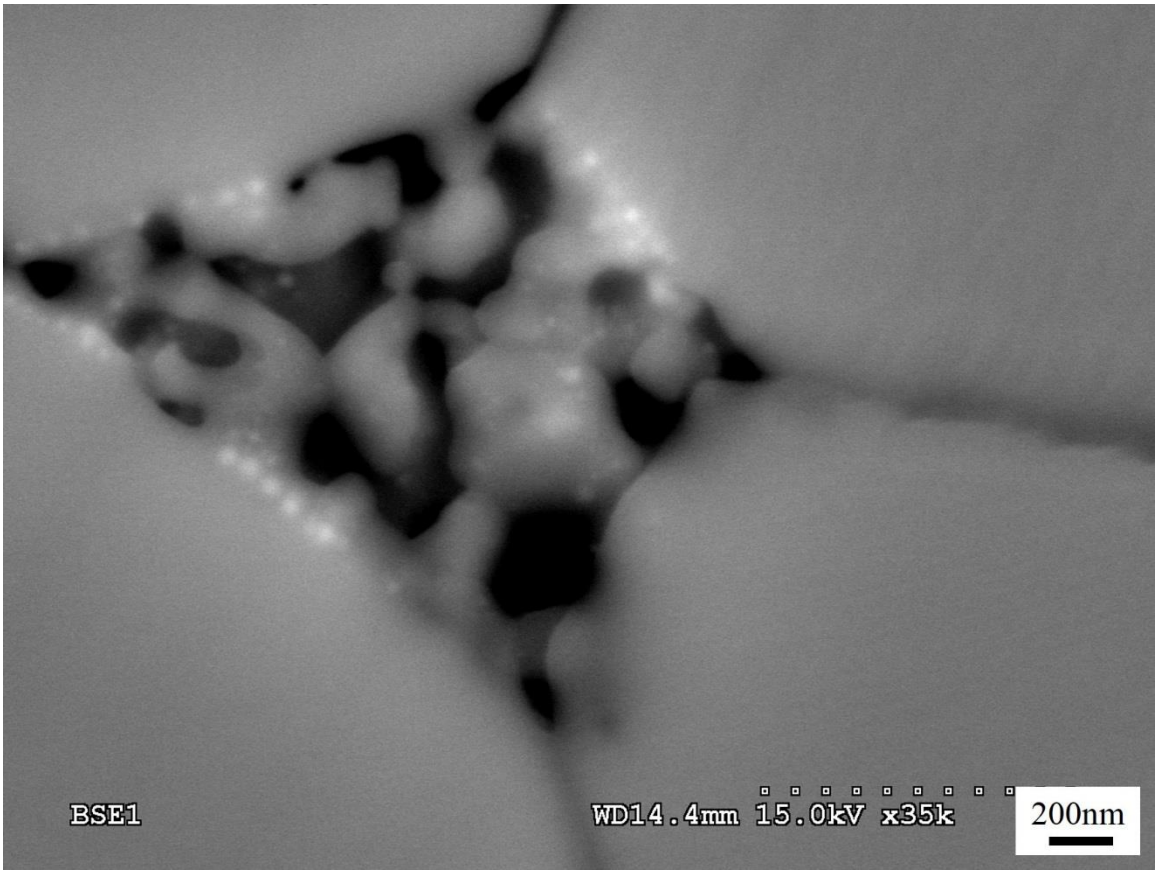

Figure 5.4 SEM BSE image of a reduced spinel precipitate in a sample reduced at 1400°C under $P_{O_2}=7.2\times10^{-15}$ for 10h.

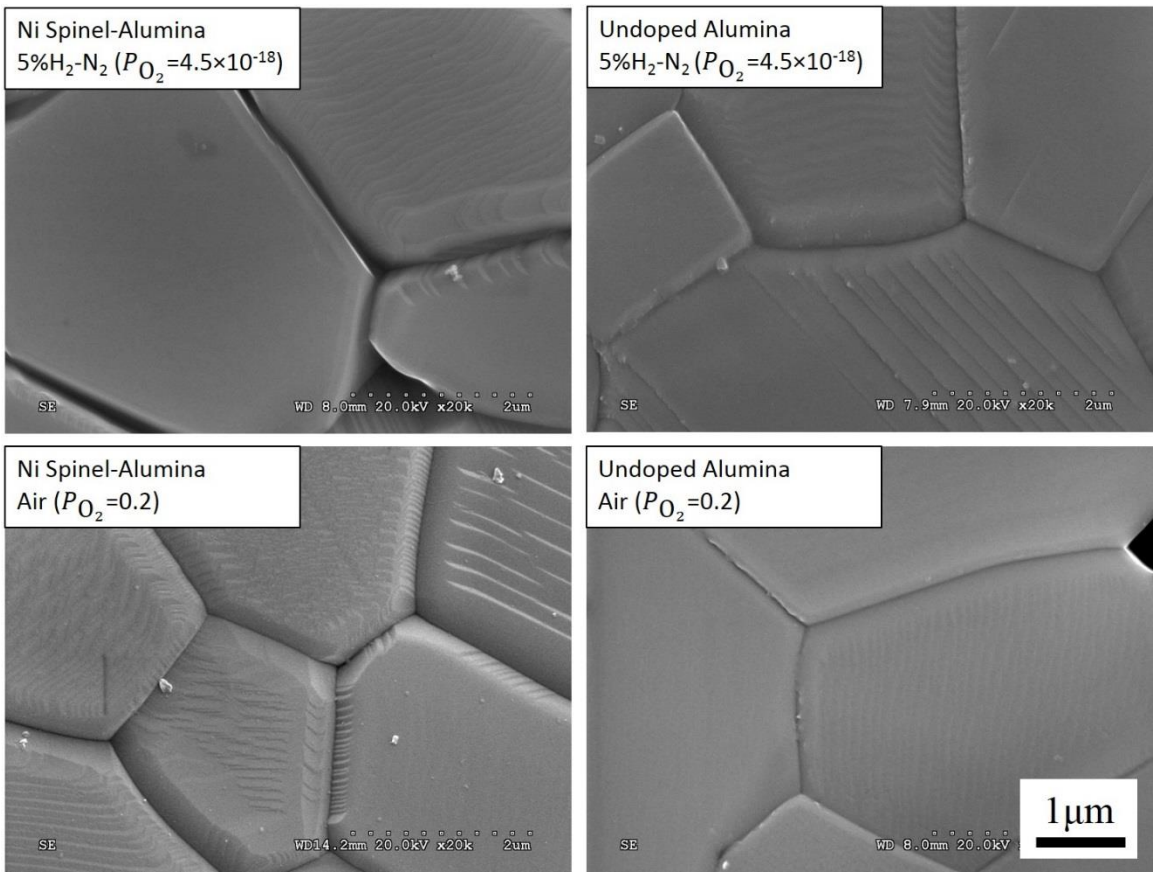

Figure 5.5 SEM images of spinel containing and undoped alumina samples annealed at 1400°C for 5h under different atmospheres.

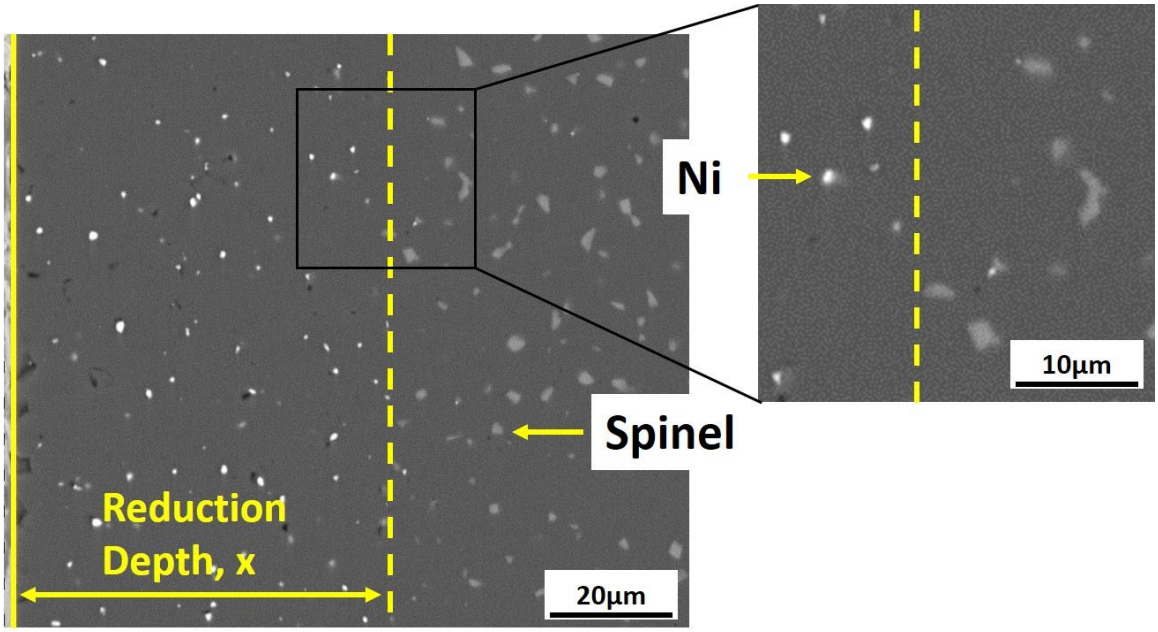

Figure 5.6 SEM BSE images of the cross section of a sample reduced at 1400°C under P_{O_2}=4.5×10^{-18} for 10 h.

5.1.3 Reduction Rates

Under each P_{O_2}, the reduction depth was measured as a function of annealing time. Figure 5.7 shows the plot of the square of the reduction depth versus reduction time for two different gas chemistries, but similar P_{O_2}. The linear relationship is consistent with diffusional transport as the rate controlling process. The rate constant under each P_{O_2} is the slope of each line, which can be calculated by Eq.(5.2).

$$x^2 = kt \qquad (5.2)$$

where *x* is the reduction depth and *t* is the reduction time and *k* is the rate constant. Although all the samples in the reduction experiments have very similar grain size, Eq. (5.3) was used to calculate the corrected rate constant to compare between different samples based on Eq. (2.7) and (2.8).

$$k_c = k \times G \qquad (5.3)$$

where k_c is the corrected rate constant and *G* is the average grain size. In the discussion, rate constant refers to the corrected rate constant.

Table 5.3 shows the corrected rate constants under these two P_{O_2}. The small difference between the corrected rate constants indicates that the chemistry of the gas mixture has minimal effect on the reduction rates. For a direct comparison, only the results under the P_{O_2} controlled by hydrogen and oxygen gas mixtures were used for future analysis and discussion.

Figure 5.8 shows the plot of the square of the reduction depth versus reduction time under the five P_{O_2} controlled by hydrogen and oxygen gas mixtures. Linear relationship

was observed under each P_{O_2}. Table 5.4 shows the corrected rate constants under different P_{O_2}. Figure 5.9 shows the plot of corrected rate constant under different P_{O_2}.

It is worth to note that the data points in Figure 5.8 were corrected using data from short annealing experiments under each P_{O_2}. The correction removed the effect of the ramping temperature and the deviation of furnace temperature from the setting temperature on the reduction, and allowed the data to be compared only in terms of annealing time. The details of the correction will be shown in Appendix A.

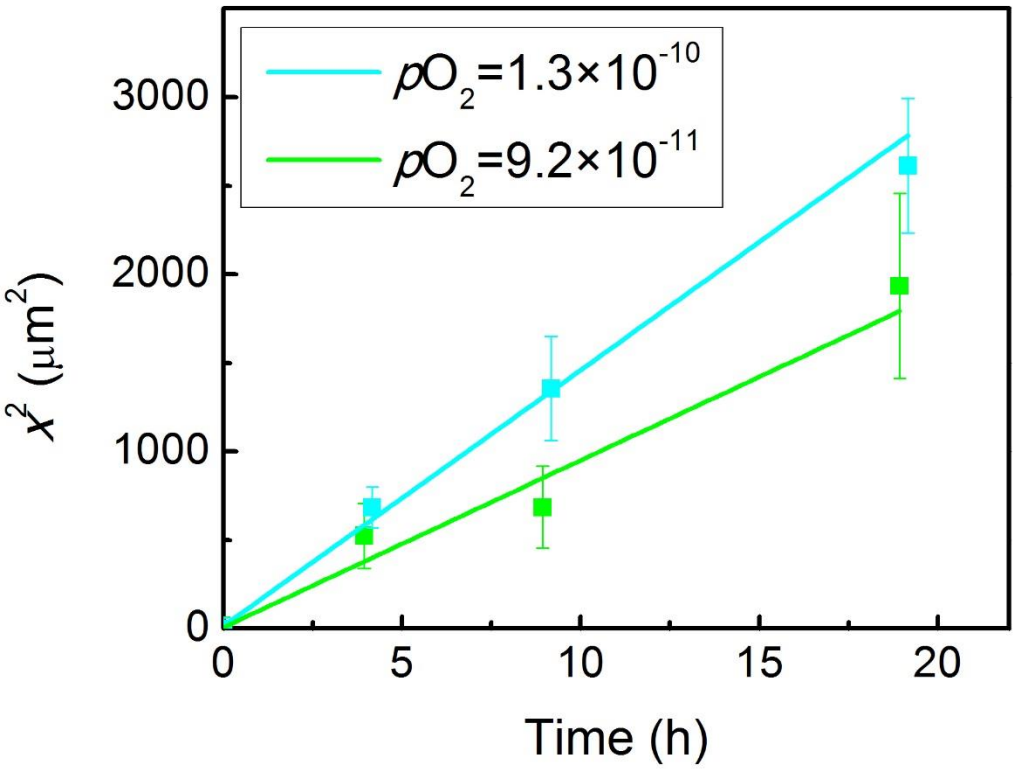

Figure 5.7 Plot of the square of the reduction depth versus reduction time under P_{O_2}=1.3×10^{-10} (controlled by H_2 and O_2 mixture) and P_{O_2}=9.2×10^{-11} (controlled by CO and CO_2 mixture).

Table 5.3 Corrected rate constants under $P_{O_2}=1.3\times10^{-10}$ (controlled by H_2 and O_2 mixture) and $P_{O_2}=9.2\times10^{-11}$ (controlled by CO and CO_2 mixture).

Gas Mixture	P_{O_2}	k_c **(m²/s)**
100ppm H_2 - 20ppm O_2 in N_2	1.3×10^{-10}	$(1.9\pm0.4)\times10^{-19}$
200ppm CO - 50ppm CO_2 in N_2	9.2×10^{-11}	$(1.3\pm0.3)\times10^{-19}$

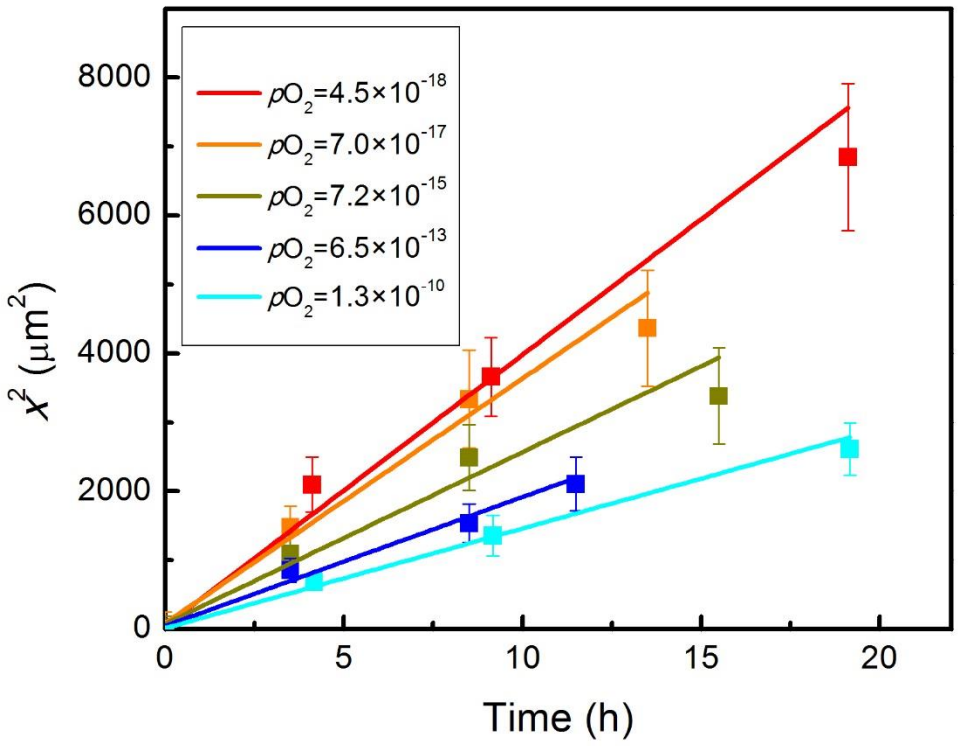

Figure 5.8 Plot of the square of the reduction depth versus reduction time under five different P_{O_2}.

Table 5.4 Corrected rate constants under five different P_{O_2}.

P_{O_2}	k_c (m²/s)
$(4.5\pm0.4)\times10^{-18}$	$(5.3\pm0.3)\times10^{-19}$
$(7.0\pm0.1)\times10^{-17}$	$(4.6\pm1.0)\times10^{-19}$
$(7.2\pm0.1)\times10^{-15}$	$(3.3\pm0.7)\times10^{-19}$
$(6.5\pm0.1)\times10^{-13}$	$(2.5\pm0.5)\times10^{-19}$
$(1.3\pm0.1)\times10^{-10}$	$(1.9\pm0.4)\times10^{-19}$

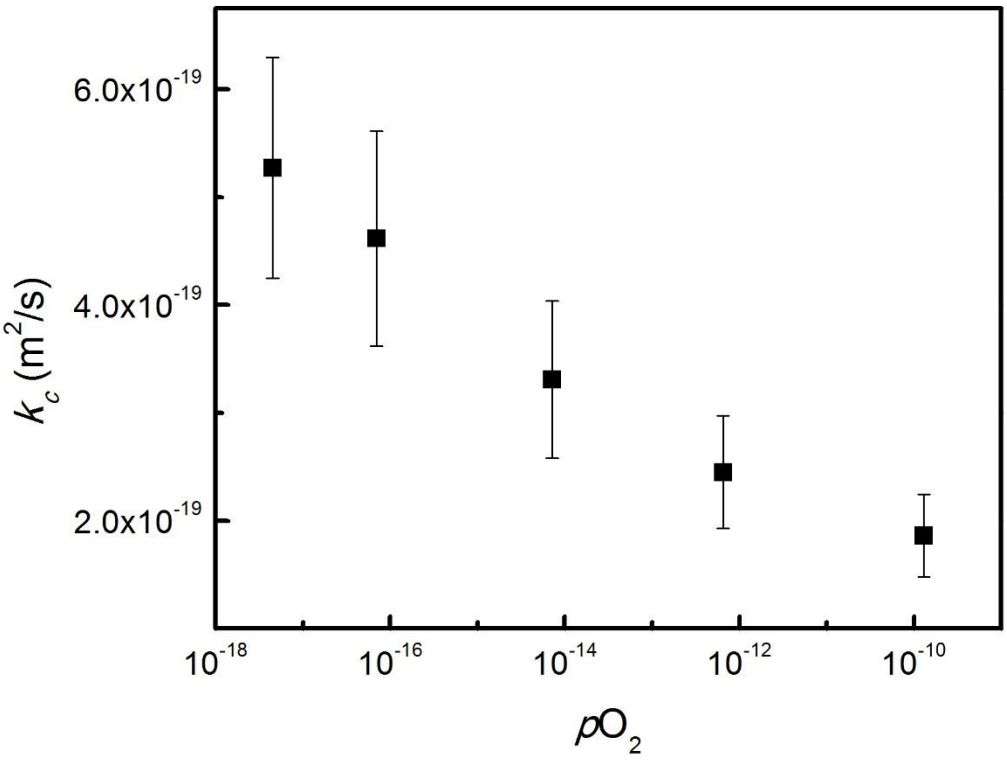

Figure 5.9 Plot of corrected rate constants under different P_{O_2}.

5.1.4 Discussion

Based on the results, several topics will be discussed. 5.1.4.1 discusses how P_{O_2} affects grain boundary transport in alumina. 5.1.4.2 discusses whether point defect models can be applied to explain grain boundary transport behavior in alumina. 5.1.4.3 compares the reduction k_c with the oxidation k_c from previous studies.

5.1.4.1 Dependence of the Kinetics of Grain Boundary Transport on Oxygen Partial Pressure

To understand the dependence of reduction rates on P_{O_2}, a quantitative expression of k_c measured in the experiments under P_{O_2} needs to be established. Eq. (2.6) shows how the flux of oxide formed is determined. Based on Eq. (5.1), the flux is

$$J_{NiAl_2O_4} = \frac{f_{NiAl_2O_4}}{V_{NiAl_2O_4}} \frac{dl}{dt} \qquad (5.4)$$

where $f_{NiAl_2O_4}$ is the volume fraction of $NiAl_2O_4$ particles inside the sample, $V_{NiAl_2O_4}$ is the molar volume of $NiAl_2O_4$, l is the reduction depth and t is the reduction time. Substituting Eq. (5.4) into Eq. (2.6), the expression of k_c is described by Eq. (5.5).

$$k_c = 2l\frac{dl}{dt}G = G\frac{V_{NiAl_2O_4}}{f_{NiAl_2O_4}}\frac{RT}{4F^2}\int_{P_{O_2}^{low}}^{P_{O_2}^{high}} \sigma t_{ion} t_e \, d\ln P_{O_2} \qquad (5.5)$$

From Eq. (5.5), it can be seen that any dependence of k_c on the oxygen partial pressure can in principle be attributed to two different mechanisms. First, the P_{O_2} inside the sample, which in reduction experiments is the $P_{O_2}^{high}$, is fixed by the equilibrium between metallic nickel and spinel. Based on results in the literature, this was taken as 4.7×10^{-8}, which is the

equilibrium P_{O_2} between Ni, $NiAl_2O_4$ and Al_2O_3[79,80]. It follows, therefore, that the lower the value of the external P_{O_2} ($P_{O_2}^{low}$), the greater the P_{O_2} gradient, and hence the larger the driving force for the reduction experiments. Second, the oxygen partial pressure can also affect $\sigma t_{ion} t_e$ by changing the concentrations of defect species or charge carriers within alumina GBs, assuming ionic diffusion in alumina GBs is conducted by the migration of defect species. The situation is complex because either ionic or electronic transport could be rate limiting, and there are multiple possibilities in terms of the dominant defect species or charge carrier. For example, assuming ionic transport is rate limiting, under highly reducing conditions the predominant defect species responsible for transport could be either oxygen vacancies or aluminum interstitials. Furthermore, the concentration of such defects would depend on whether the material is exhibiting nonstoichiometric behavior or not.

To calculate the dependence of $\sigma t_{ion} t_e$ on P_{O_2}, k_c needs to be fit with $\ln P_{O_2}$ by a function. With the function, $\sigma t_{ion} t_e$ can be calculated from Eq. (5.6).

$$\sigma t_{ion} t_e = \frac{4F^2 f_{NiAl_2O_4}}{RTGV_{NiAl_2O_4}} \frac{\partial (k_c)}{\partial \ln P_{O_2}} \qquad (5.6)$$

A linear fit between k_c and $\ln(P_{O_2})$ was achieved with R^2 value of 0.94. The good linear fit suggests that $\sigma t_{ion} t_e$ is independent of P_{O_2}. In other words, the effect of P_{O_2} on k_c is mainly due to the driving force, $\ln(P_{O_2}^{high})$-$\ln(P_{O_2}^{low})$, the difference of oxygen chemical potential on each side of the sample. Figure 5.10 shows the ratio between k_c and the driving force of the transport, $\ln(P_{O_2}^{high})$-$\ln(P_{O_2}^{low})$, under each P_{O_2}. A horizontal line can be drawn to fit the data within error.

Balmain and Huntz measured the electrical conductivity and ionic transference number of the alumina scale during the growth of alumina scale on a β-NiAl alloy[47]. Their results showed that k_c is proportional to $P_{O_2}^{-0.03}$ under the P_{O_2} range from 10^{-14} to 10^{-6}. This relation is close to $P_{O_2}^{0}$, as the current work suggested.

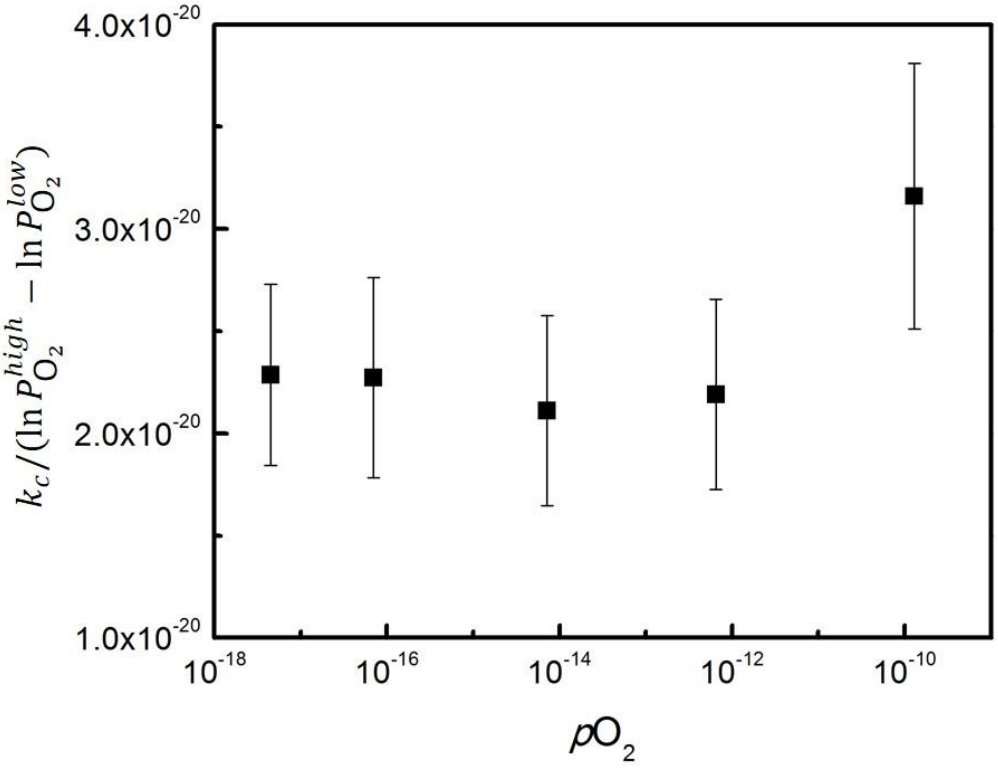

Figure 5.10 The ratio between k_c and the driving force of the transport, ln($P_{O_2}^{high}$)-ln($P_{O_2}^{low}$), under each P_{O_2}.

5.1.4.2 Feasibility of Applying Point Defect Chemistry Models to Explain Grain Boundary Transport in Alumina

Point defect models are first assumed to be able to explain the transport behavior of polycrystalline alumina to examine whether point defect models can explain grain boundary transport in alumina. Wagner oxidation theory will be used to establish the relationship between point defect concentration and transport in alumina.

During reduction, the slower diffusion species between electronic carriers and ions determines the overall transport. It can be seen from Eq. (5.5) in another form.

$$k_c = 2l\frac{dl}{dt}G = G\frac{V_{NiAl_2O_4}}{f_{NiAl_2O_4}}\frac{RT}{4F^2}\int_{P_{O_2}^{low}}^{P_{O_2}^{high}}\frac{\sigma_{ion}}{\frac{t_{ion}}{t_e}+1}d\ln P_{O_2} \qquad (5.7)$$

Eq. (5.7) shows that when $t_{ion} \ll t_e$, k_c is mainly determined by σ_{ion}. Similarly, when $t_e \ll t_{ion}$, k_c is mainly determined by σ_e. As shown in 2.3, there is no agreement about the value of t_{ion} in alumina. In order to address the current topic, the two limiting cases will be considered.

By way of illustrating the analytical approach employed in this study, the case where it is assumed that ionic transport is rate limiting, and that transport is occurring by oxygen vacancies will be considered. The same analysis can be applied to the conditions that the diffusion of aluminum, electrons or holes determines the overall transport. When ionic diffusion is rate limiting, Eq. (5.7) can be simplified to Eq. (5.8) using Eq. (2.2), and Eq. (2.8).

$$k_c = 2l\frac{dl}{dt}G = \frac{2V_{\mathrm{NiAl_2O_4}}}{f_{\mathrm{NiAl_2O_4}}}\int_{P_{O_2}^{low}}^{P_{O_2}^{high}} (\delta D_O^{GB} C_O^{GB} + \frac{9}{4}\delta D_{\mathrm{Al}}^{GB} C_{\mathrm{Al}}^{GB})\, d\ln P_{O_2} \qquad (5.8)$$

Oxygen diffusivity can be expressed by oxygen vacancy diffusivity using Eq. (5.9).

$$D_O^{GB} C_O^{GB} = D_{V_O^{\cdot\cdot}}^{GB} C_{V_O^{\cdot\cdot}}^{GB} \qquad (5.9)$$

where $D_{V_O^{\cdot\cdot}}^{GB}$ is the oxygen vacancy GB diffusivity and $C_{V_O^{\cdot\cdot}}^{GB}$ is the oxygen vacancy concentration at GB. Since $D_{V_O^{\cdot\cdot}}^{GB}$ is independent of oxygen vacancy concentration, it is constant over the P_{O_2} gradient. Eq. (5.8) can be further simplified to Eq. (5.10).

$$k_c = 2l\frac{dl}{dt}G = \frac{2V_{\mathrm{NiAl_2O_4}}}{f_{\mathrm{NiAl_2O_4}}}\delta D_{V_O^{\cdot\cdot}}^{GB}\int_{P_{O_2}^{low}}^{P_{O_2}^{high}} C_{V_O^{\cdot\cdot}}^{GB}\, d\ln P_{O_2} \qquad (5.10)$$

The dependence of $C_{V_O^{\cdot\cdot}}^{GB}$ on P_{O_2} is determined by point defect models. By considering how $C_{V_O^{\cdot\cdot}}^{GB}$ depends on P_{O_2} using point defect models, the dependence of k_c on P_{O_2} can be calculated. Two distinct models that both assume ionic transport is rate limiting, and transport is occurring by oxygen vacancies will be considered first. Then, this analysis will be applied to all the other possible point defect models.

5.1.4.2.1 Oxygen Vacancy-Extrinsic Model

For the oxygen vacancy ($V_O^{\cdot\cdot}$)-extrinsic model, oxygen vacancies are the rate-limiting species and their concentration, $C_{V_O^{\cdot\cdot}}^{GB}$, is determined by an extrinsic factor, which is the concentration of $\mathrm{Ni}_{\mathrm{Al}}'$ as the major impurity in this study. The nickel ions are assumed to occupy aluminum sites so that the corresponding point defect is $\mathrm{Ni}_{\mathrm{Al}}'$. This model has been used to explain point defect chemistry in alumina traditionally since the concentration of

intrinsic defects in alumina is believed to be much lower than the concentration of impurities. For this model, Eq. (5.11) describes the defect chemistry reaction.

$$2\mathrm{NiO} \xrightarrow{\mathrm{Al_2O_3}} 2\mathrm{Ni}'_{\mathrm{Al}} + 2\mathrm{O}_{\mathrm{O}}^{\times} + V_{\mathrm{O}}^{\cdot\cdot} \qquad (5.11)$$

$C_{V_{\mathrm{O}}^{\cdot\cdot}}^{GB}$ equals to half of the concentration of $\mathrm{Ni}'_{\mathrm{Al}}$. By substituting this relationship into Eq. (5.10), the dependence of k_c on P_{O_2} can be expressed by Eq. (5.12).

$$k_c \propto (\ln P_{\mathrm{O}_2}^{high} - \ln P_{\mathrm{O}_2}^{low}) \qquad (5.12)$$

where $P_{\mathrm{O}_2}^{high}$ is the equilibrium P_{O_2} for Eq. (5.1) inside the sample, which is 4.7×10^{-8}, and $P_{\mathrm{O}_2}^{low}$ is the P_{O_2} of the reducing atmosphere outside the sample. Based on this expression, the predicted ratio of k_c values compared to k_c at $P_{\mathrm{O}_2}=1.3\times10^{-10}$, $k_c/k_c(P_{\mathrm{O}_2}=1.3\times10^{-10})$, was calculated. The results are shown in Table 5.5.

5.1.4.2.2 Oxygen Vacancy-Intrinsic Model

For the oxygen vacancy ($V_{\mathrm{O}}^{\cdot\cdot}$)-intrinsic model, oxygen vacancies are the rate-limiting species and their concentration, $C_{V_{\mathrm{O}}^{\cdot\cdot}}^{GB}$, is determined by an intrinsic factor, which is P_{O_2}. This is also the point defect model Kitaoka et al. used to explain the transport behavior of undoped alumina and doped alumina[5–9]. Eq. (5.13) describes the defect chemistry reaction.

$$\mathrm{O}_{\mathrm{O}}^{\times} \xrightarrow{\mathrm{Al_2O_3}} V_{\mathrm{O}}^{\cdot\cdot} + \frac{1}{2}\mathrm{O}_2 \uparrow + 2e' \qquad (5.13)$$

It follows that the dependence of $C_{V_{\mathrm{O}}^{\cdot\cdot}}^{GB}$ is given by Eq. (5.14).

$$C_{V_{\mathrm{O}}^{\cdot\cdot}}^{GB} \propto P_{\mathrm{O}_2}^{-1/6} \qquad (5.14)$$

By substituting Eq. (5.14) into Eq. (5.10), the dependence of k_c on P_{O_2} can be expressed by Eq. (5.15).

$$k_c \propto (P_{O_2}^{high\,-\frac{1}{6}} - P_{O_2}^{low\,-\frac{1}{6}}) \qquad (5.15)$$

Based on this expression, the predicted ratio, $k_c/k_c(P_{O_2}=1.3\times10^{-10})$, was calculated. The results are shown in Table 5.5.

5.1.4.2.3 Oxygen Vacancy-Extrinsic Model vs. Oxygen Vacancy-Intrinsic Model

The predictions from the oxygen vacancy-extrinsic model and the oxygen vacancy-intrinsic model were compared with the experimental results. The results are shown in Table 5.5, and presented graphically in Figure 5.11. It is clear that the oxygen vacancy-extrinsic model is consistent with the experimental results, while the oxygen vacancy-intrinsic model is not. Note that because intrinsic defects are more likely to be dominant at higher temperature, the situation may be different at higher temperatures. Nonetheless, it is clear that at 1400°C or lower temperatures, the point defect model Kitaoka et al.[5–9] used to explain their results can't be applied to alumina scales.

This result is also consistent with the calculated oxygen vacancy concentration under the experimental conditions of the current study. Table 5.6 shows the calculated oxygen vacancy concentration in undoped alumina at 1400°C based on defect formation energies reported by Kroger et al.[43,52]. It can be seen that under $P_{O_2}=1\times10^{-18}$, the oxygen vacancy concentration is at the level of 0.001ppm in undoped alumina. In the current study, there was Ni^{2+} present in the samples. Though there is no data about the solubility of Ni^{2+} in

alumina, it is reasonable to assume the solubility is more than 1ppm. Kroger et al. showed that there was 6.6ppm (in weight, 5.7ppm in molar) Ni present in a Ni-doped single crystal alumina[43]. A recent atom probe tomography study showed that there was about 700ppm Ni present in the grains of a Ni-doped alumina sample. It is clear that there were more oxygen vacancies formed from impurities than from intrinsic (P_{O_2}) under the experimental conditions of the current study. In other words, the oxygen vacancy concentration is determined by the impurity level instead of P_{O_2}, which is consistent with the oxygen vacancy-extrinsic model.

Heuer et al.[20] claimed that thermally grown alumina scales are "remarkably free of impurities", and that the oxygen vacancy concentration is determined by P_{O_2} in alumina scales inspired from the results of the high temperature oxygen permeation experiments Kitaoka et al. reported[5–9]. However, results from literature contradict Heuer's claims. In Heuer's paper[20], he cited a reference about an atom probe tomography (APT) study on alumina scales[81]. The reference concluded that alumina scales formed at temperatures above 1000°C were free from impurities. But in that paper, samples were counted as "free of impurities" when their concentrations were less than 1000ppm. Impurities present in the scales with concentration less than 1000ppm were not quantitatively measured. Actually, the results in this paper showed that Ni segregated at interfaces between a FeCrAl alloy and the scale grown on it, and there were Ni dispersed in the scale as well. This paper also showed the existence of Fe, Cr and Ni in a scale grown on a Ni-based alloy. Other APT studies also showed the existence of impurities in alumina scales[82–86]. Seidman et al. studied an alumina scale grown on a single crystal Ni-based superalloy at 1000°C-1200°C

by APT and TEM, and found Cr, Ni, Co, Ru and refractory metal (RM) elements (Hf, Ta, W, Re) present in the scale[82]. Stiller et al. found Fe^{2+}, Fe^{3+} Cr^{2+} and Cr^{3+} in an alumina scale grown on an FeCrAl alloy at 1100°C by APT[83,86]. Marquis et al. used ATP to find Zr, Hf, Y, Si and Ti in alumina scales grown in two TBCs at 1100°C[84,85]. Both TBCs had Ni-based alloys as the bond coat layers, and yttria-stabilized zirconia as the top coat layers. TEM observations and EDS measurements showed the presence of reactive elements (Zr, Y, Hf) at GBs in alumina scales grown on different alumina forming alloys (FeCrAl, MCrAlYHfSi, Ni-based alloy, Fe-based alloys and β-NiAl) from 1000°C-1500°C [37,87–89]. Moreover, a secondary neutral mass spectrometry (SNMS) study showed there were about 1at% Fe and Cr in the alumina scale grown on a FeCrAl alloy at 900-1100°C[30]. From the studies on the chemistry of alumina scales by different methods, it can be seen that the claim that alumina scales are "remarkably free of impurities" lacks support.

Based on the defect formation energies reported by Kroger et al.[43,52], the oxygen vacancy concentration in pure alumina is extremely low at the condition when alumina scales form. During the formation of an alumina scale, the oxygen vacancy concentration is highest in the alumina scale at the interface between the alloy and the scale, where P_{O_2} is the lowest. There is no direct way to measure this P_{O_2}, but several studies calculated the activities of Al at the interfaces for different alloys and used the thermodynamics of alumina formation to calculate the P_{O_2} at the interfaces[4,90–92]. Table 5.7 lists the temperatures and P_{O_2} at the scale-alloy interfaces reported in the literature, and the calculated oxygen vacancy concentrations in undoped alumina at the corresponding

conditions. At the temperatures and P_{O_2} when alumina scales form, the oxygen vacancy concentrations in undoped alumina are less than 0.01ppm, which is much less than the impurity levels in the alumina scales. This means that the transport in alumina scales is independent of P_{O_2}, which is consistent with the results of current study.

Recent high temperature oxygen permeation experiments by Kitaoka et al.[5–9] at 1650°C suggested a dependence of grain boundary diffusivities on P_{O_2} in both undoped alumina and doped alumina, which was interpreted using the oxygen vacancy-intrinsic model. In their experiments to study the oxygen GB diffusion, the annealing temperature was 1650°C and the annealing P_{O_2} was from 1×10^{-12} to 1×10^{-5}. Among these conditions, the lowest P_{O_2} was 1×10^{-12}, however, the oxygen vacancy concentration in undoped alumina is only 0.038ppm at 1650°C under $P_{O_2}=1\times10^{-12}$ calculated using the defect formation energies reported by Kroger et al.[43,52]. As described in the paper, the alumina powder used in the permeation experiments has >99.99% purity, therefore, the oxygen vacancy concentration determined by P_{O_2} was *much lower* than the impurity level in their samples. Accordingly, we contend that the oxygen vacancy-intrinsic model is not applicable, especially for the doped alumina samples. The dependence of permeation rates on P_{O_2} that Kitaoka et al. observed could not be explained at this time. Roberts reported that during high temperature oxygen permeation, impurities could diffuse out from GBs in alumina and pores formed in the samples[93]. The concentration of impurities would be P_{O_2} dependent, and the interactions of impurities at high temperatures may balance their extrinsic effects and result in the intrinsic behavior Kitaoka et al. observed.

5.1.4.2.4 Considerations of Other Possible Point Defect Models

So far, only the two models that assume ionic transport is rate limiting, and transport is occurring by oxygen vacancies have been considered. As mentioned in 5.1.4.1, either ionic or electronic transport could be rate limiting, and there are multiple possibilities in terms of the dominant defect species or charge carrier. Also, the concentration of such defects would depend on whether the material was exhibiting intrinsic or extrinsic behavior. Following the analysis of the two models mentioned above, other possible scenarios will be considered here.

To consider other scenarios, Brouwer diagrams were used to represent how the concentration of a point defect depends on P_{O_2}. A Brouwer diagram shown as Figure 5.12 was drawn for Ni-doped alumina, in which oxygen vacancies are assumed to be the dominant ionic defects to compensate Ni'_{Al}. The Figure 5.13 shows a Brouwer diagram drawn for Ni-doped alumina in which aluminum interstitials are assumed to be the dominant ionic defects to compensate Ni'_{Al}. The numbers labeled in the diagrams represent the exponents of the power functions of P_{O_2} to describe defect concentrations. The letters labeled in the diagrams represent different scenarios corresponding to different models. For example, B represents the oxygen vacancy-intrinsic model considered above, and the number -1/6, which is next to A, represents the relation in Eq. (5.14).

Both Figure 5.12 and Figure 5.13 have four regions. The outer two regions in each diagram represent intrinsic behavior of alumina, while the middle two regions are impurity controlled. For each diagram, the rightmost region was not considered since the P_{O_2} range for this region is quite high, which does not match the experimental conditions of the current study. Without knowing whether electronic diffusion or ionic diffusion determines

the transport and the diffusivities of each species, both the dominant ionic defect and electronic defect were considered as possible rate limiting species in different P_{O_2} ranges in Figure 5.12 and Figure 5.13. The results are summarized in Table 5.8. Since oxygen vacancy-extrinsic model is consistent with experimental results, the predictions from other models were compared with both experimental results and the predictions from the oxygen vacancy-extrinsic model. The comparison results are shown graphically in Figure 5.14-Figure 5.21. The scales of the y-axis in some of these graphs are different.

After considering all the scenarios, predictions from model C, E, F, H and K are close to experimental results. Among them, model C and K assume ionic diffusion is rate limiting and the concentrations of the dominant ionic defects are determined by impurity level. Model E and F both assume electronic diffusion is rate limiting and the dominant species are holes. Model H assumes aluminum vacancies diffusion is rate limiting and the concentrations of aluminum vacancies are determined by P_{O_2}.

But results in the literature show that model E, F and H could not represent the real condition. Based on the formation energies of defects from Kroger et al.[43,52], a quantitative Brouwer diagram was drawn based on the data reported from Kroger et al[43,52], shown as Figure 5.22. The concentration of $Ni'_{Al}$was assumed to be 100ppm to calculate the diagram. The diagram shows that under the P_{O_2} condition used in the current reduction experiments, oxygen vacancies are the dominant ionic defects and electrons are the dominant electronic carriers. So model E, F and H are not applicable to the explain the results of the current study.

In summary, this part of discussion showed that oxygen vacancy-intrinsic model cannot explain grain boundary transport in alumina. Among all the possible scenarios, oxygen vacancy-extrinsic model is consistent with the experimental results and the results reported in the literature.

It is worth to note that although the oxygen vacancy-extrinsic model is consistent with experimental results, how lattice point defects affect defects in grain boundaries in polycrystalline alumina is still not clear. Grain boundaries are much more disordered than lattice, the concentrations of defects at GBs are expected to be much higher than those in the lattice. The experimental results and the above analysis suggests that the concentration of defects at grain boundaries in alumina are fixed by impurities. To understand the quantitative relationship between impurity level and the concentrations of defects at GBs, more studies need to be done.

Table 5.5 The predicted ratio of the k_c values compared to k_c at P_{O_2}=1.3×10^{-10}, $k_c/k_c(P_{O_2}$=1.3×10^{-10}), calculated for both the oxygen vacancy-extrinsic model and the oxygen vacancy-intrinsic model. Ratios obtained from the experimental data are included for comparison. (Both models assume ionic diffusion is rate limiting and that oxygen vacancies are the dominant ionic defects.)

$P_{O_2}^{low}$	$V_O^{\cdot\cdot}$-Extrinsic Impurity Model		$V_O^{\cdot\cdot}$-Intrinsic Nonstoichiometry Model		Experimental Results
	$\ln P_{O_2}^{high} - \ln P_{O_2}^{low}$	$\frac{k_c}{k_c(P_{O_2} = 1.3\times10^{-10})}$	$P_{O_2}^{high^{-\frac{1}{6}}} - P_{O_2}^{low^{-\frac{1}{6}}}$	$\frac{k_c}{k_c(P_{O_2} = 1.3\times10^{-10})}$	$\frac{k_c}{k_c(P_{O_2} = 1.3\times10^{-10})}$
4.5×10^{-18}	23.1	3.9	761.6	27.4	2.8±0.3
7.0×10^{-17}	20.3	3.5	475.9	17.1	2.5±0.3
7.2×10^{-15}	15.7	2.7	210.9	7.6	1.8±0.3
6.5×10^{-13}	11.2	1.9	90.8	3.3	1.3±0.3
1.3×10^{-10}	5.9	1.0	27.8	1.0	1.0±0.3

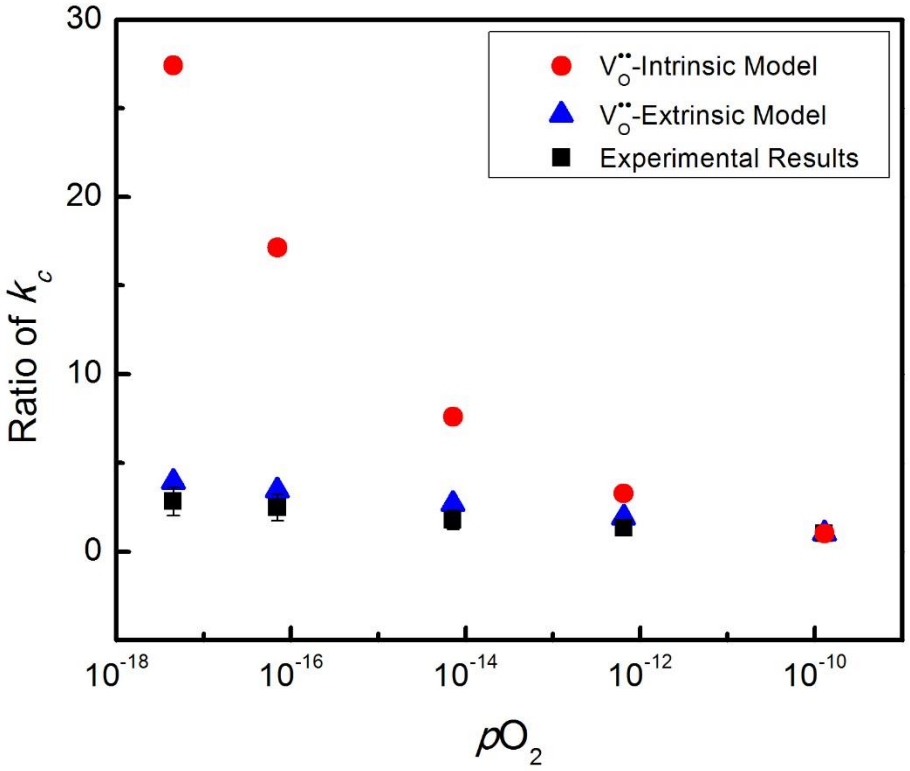

Figure 5.11 Graph of k_c ratios, $k_c/k_c(P_{O_2}=1.3\times10^{-10})$, as a function of external P_{O_2}. Experimental results and predictions from the oxygen vacancy-extrinsic model and the oxygen vacancy-intrinsic model are depicted. Both models assume ionic diffusion is rate limiting and that oxygen vacancies are the dominant ionic defects.

Table 5.6 Calculated defect concentrations from different defect types in alumina at 1400°C. The defect formation enthalpies were from Kroger et al.[43,52]. The formation entropy was assumed to be 0.5meV/K for each defect and 2meV/k for O_2[48,60].

Defect Type	Defect Reaction	ΔH (eV)	ΔS (meV)	Defect Concentration
Schottky	$\text{null} = 2V'''_{\text{Al}} + 3V^{\cdot\cdot}_{\text{O}}$	19.15	2.5	$[V^{\cdot\cdot}_{\text{O}}]=1.2\times10^{-9}$, $[V'''_{\text{Al}}]=8\times10^{-10}$
Al-Frenkel	$\text{null} = V'''_{\text{Al}} + \text{Al}_i^{\cdot\cdot\cdot}$	8.9	1.0	$[V'''_{\text{Al}}]=[\text{Al}_i^{\cdot\cdot\cdot}]=1.3\times10^{-11}$
Electronic	$\text{null} = e' + h^{\cdot}$	10.35	1.0	$n=p=8\times10^{-14}$
Intrinsic Nonstoichiometry	$\text{O}^{\times}_{\text{O}} = \frac{1}{2}\text{O}_2\uparrow + V^{\cdot\cdot}_{\text{O}} + 2e'$	15.36 (Ni-doped)	2.5	$[V^{\cdot\cdot}_{\text{O}}]=3.8\times10^{-9}$ ($P_{\text{O}_2}=1\times10^{-18}$)

Table 5.7 Temperatures and P_{O_2} at the scale-alloy interfaces reported in the literature[4,90–92], and the calculated oxygen vacancy concentrations in undoped alumina at the corresponding conditions. Oxygen vacancy concentrations were calculated based on defect formation energies reported by Kroger et al.[43,52].

Reference	Temperature	P_{O_2}	$[V_O^{\cdot\cdot}]$
Smialek et al.	1000	1.8×10^{-31}	7.1×10^{-12}
	1100	1.9×10^{-28}	6.7×10^{-11}
	1200	7.9×10^{-26}	4.6×10^{-10}
	1300	1.5×10^{-23}	2.5×10^{-09}
	1400	1.5×10^{-21}	1.1×10^{-08}
Ramanarayanan et al.	1100	5×10^{-28}	5.7×10^{-11}
Young et al.	1200	3.1×10^{-25}	3.7×10^{-10}
	1250	6.3×10^{-24}	8.4×10^{-10}
	1300	1.0×10^{-22}	1.8×10^{-9}
Chatterjee et al.	1100	1.7×10^{-19}	2.2×10^{-12}
	1200	2.4×10^{-18}	2.6×10^{-11}

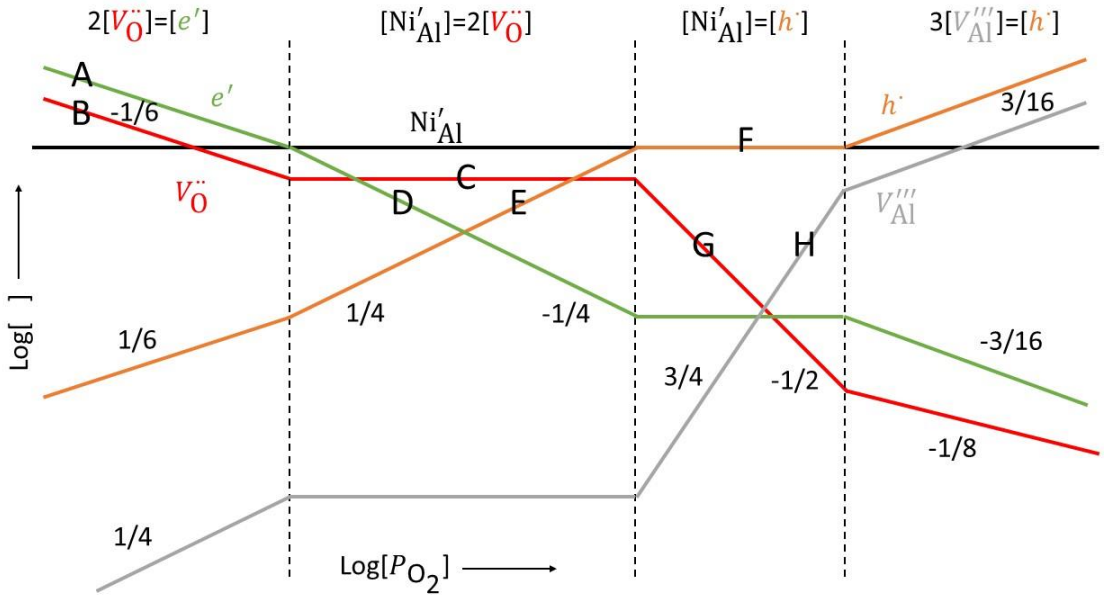

Figure 5.12 Brouwer diagram for Ni-doped alumina with assumption that oxygen vacancies are the dominant ionic defects to compensate Ni'_{Al}.

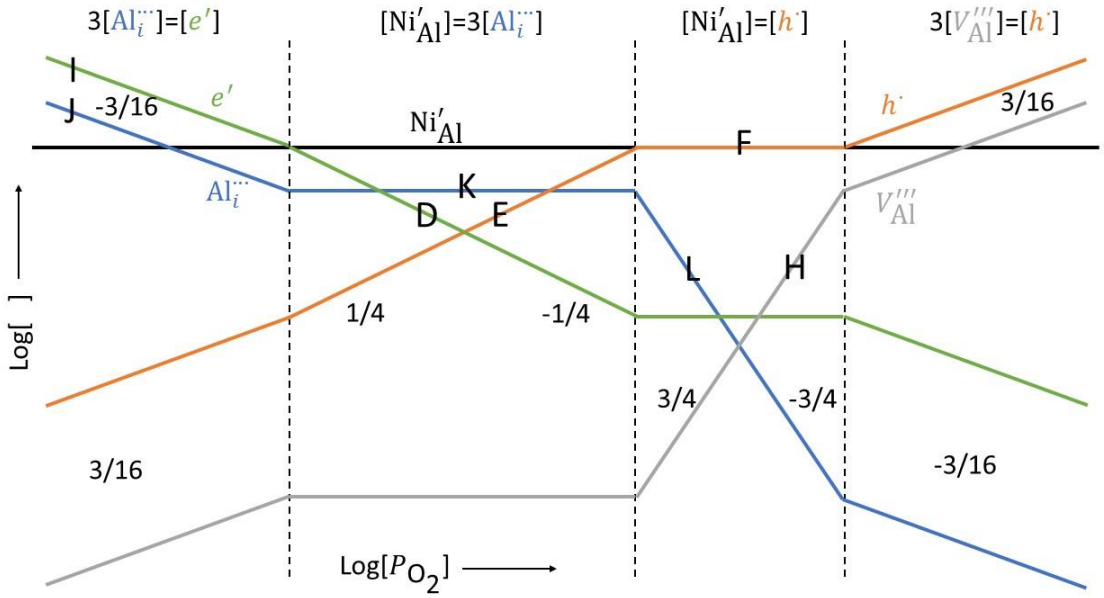

Figure 5.13 Brouwer diagram for Ni-doped alumina with assumption that aluminum interstitials are the dominant ionic defects to compensate Ni'_{Al}.

Table 5.8 Summary of all possible models. For each model, the corresponding letter in Figure 5.12 and Figure 5.13, the rate-limiting species, whether the concentration of the rate-limiting species depend on impurity or P_{O_2}, the corresponding figure, and whether the prediction is consistent with the experimental results are listed.

Model	Rate-limiting Species	Impurity vs. P_{O_2}	Corresponding Figure	Consistency with Experimental Results
A	e'	P_{O_2}	Figure 5.14	NO
B	$V_O^{\cdot\cdot}$	P_{O_2}	Figure 5.14	NO
C	$V_O^{\cdot\cdot}$	Impurity	Figure 5.15	YES
D	e'	P_{O_2}	Figure 5.16	NO
E	$h^{\cdot}$	P_{O_2}	Figure 5.17	YES*
F	$h^{\cdot}$	Impurity	Figure 5.15	YES*
G	$V_O^{\cdot\cdot}$	P_{O_2}	Figure 5.18	NO
H	$V_{Al}^{'''}$	P_{O_2}	Figure 5.19	YES*
I	e'	P_{O_2}	Figure 5.20	NO
J	$Al_i^{\cdot\cdot\cdot}$	P_{O_2}	Figure 5.20	NO
K	$Al_i^{\cdot\cdot\cdot}$	Impurity	Figure 5.15	YES
L	$Al_i^{\cdot\cdot\cdot}$	P_{O_2}	Figure 5.21	NO

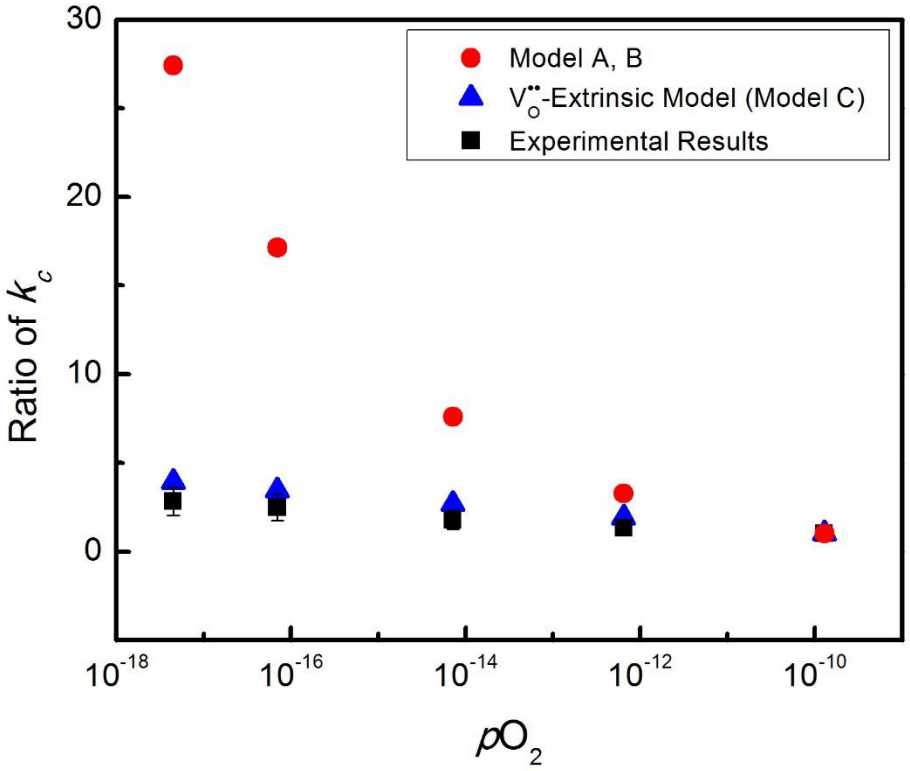

Figure 5.14 Graph of k_c ratios, $k_c/k_c(P_{O_2}=1.3\times10^{-10})$, as a function of external P_{O_2}. Experimental results and predictions from the oxygen vacancy-extrinsic model, model A and B are depicted. Model A assumes electrons are rate-limiting species, and their concentration is determined by P_{O_2}. Model B assumes oxygen vacancies are rate-limiting species, and their concentration is determined by P_{O_2}.

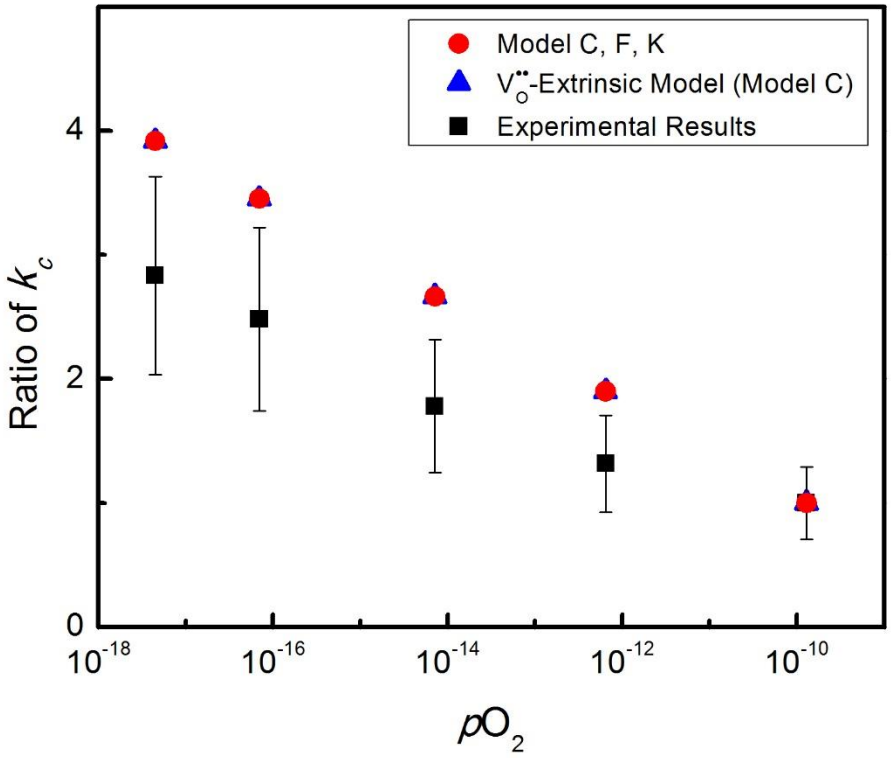

Figure 5.15 Graph of k_c ratios, $k_c/k_c(P_{O_2}=1.3\times10^{-10})$, as a function of external P_{O_2}. Experimental results and predictions from the oxygen vacancy-extrinsic model, model C, F and K are depicted. Model C assumes oxygen vacancies are rate-limiting species, and their concentration is determined by impurities. Model F assumes holes are rate-limiting species, and their concentration is determined by impurities. Model K assumes aluminum interstitials are rate-limiting species, and their concentration is determined by impurities.

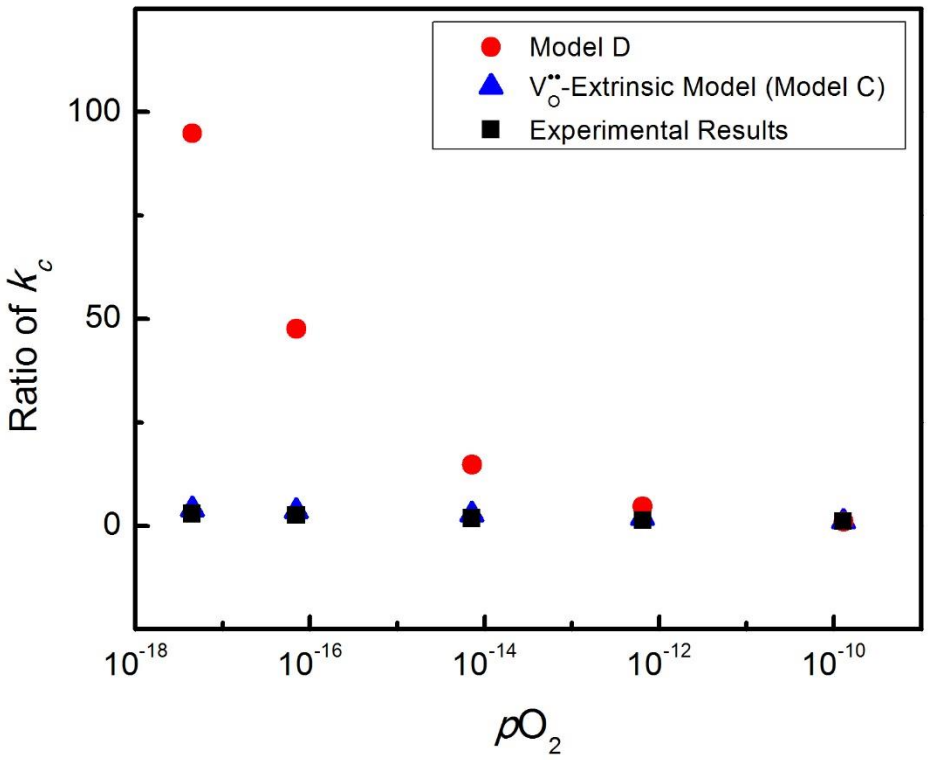

Figure 5.16 Graph of k_c ratios, $k_c/k_c(P_{O_2}=1.3\times10^{-10})$, as a function of external P_{O_2}. Experimental results and predictions from the oxygen vacancy-extrinsic model and model D are depicted. Model D assumes electrons are rate-limiting species, and their concentration is determined by P_{O_2}.

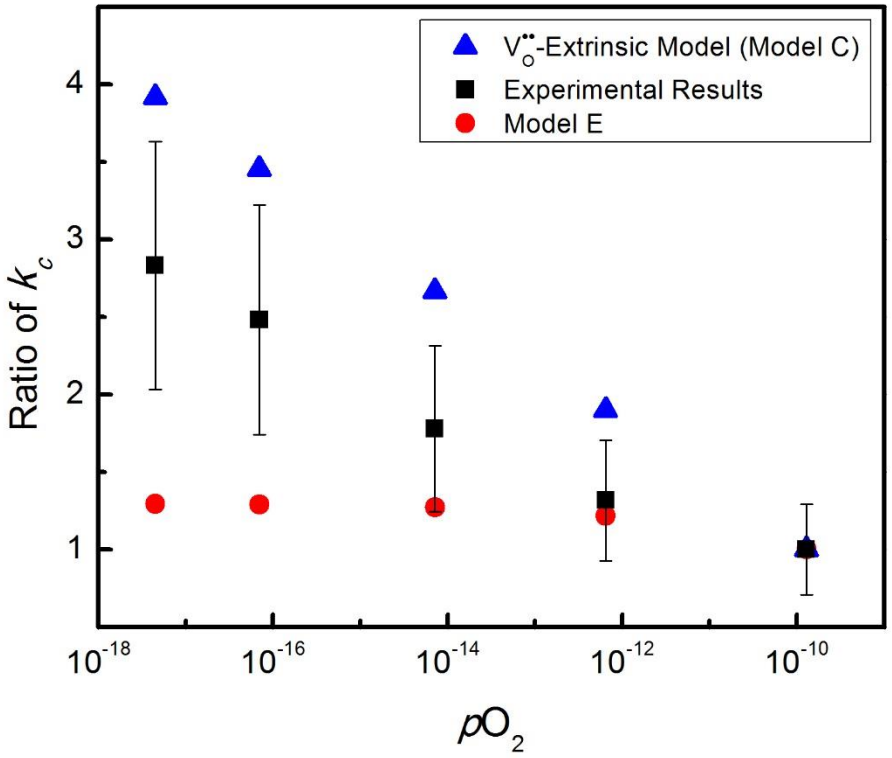

Figure 5.17 Graph of k_c ratios, $k_c/k_c(P_{O_2}=1.3\times10^{-10})$, as a function of external P_{O_2}. Experimental results and predictions from the oxygen vacancy-extrinsic model and model E are depicted. Model E assumes holes are rate-limiting species, and their concentration is determined by P_{O_2}.

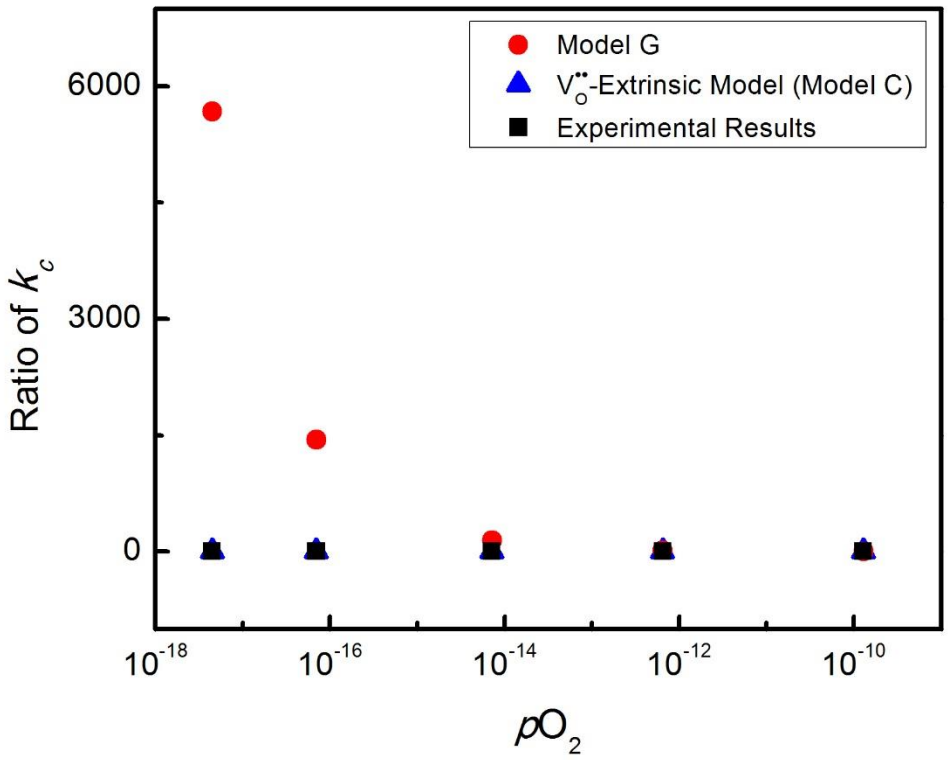

Figure 5.18 Graph of k_c ratios, $k_c/k_c(P_{O_2}=1.3\times10^{-10})$, as a function of external P_{O_2}. Experimental results and predictions from the oxygen vacancy-extrinsic model and model G are depicted. Model G assumes oxygen vacancies are rate-limiting species, and their concentration is determined by P_{O_2}.

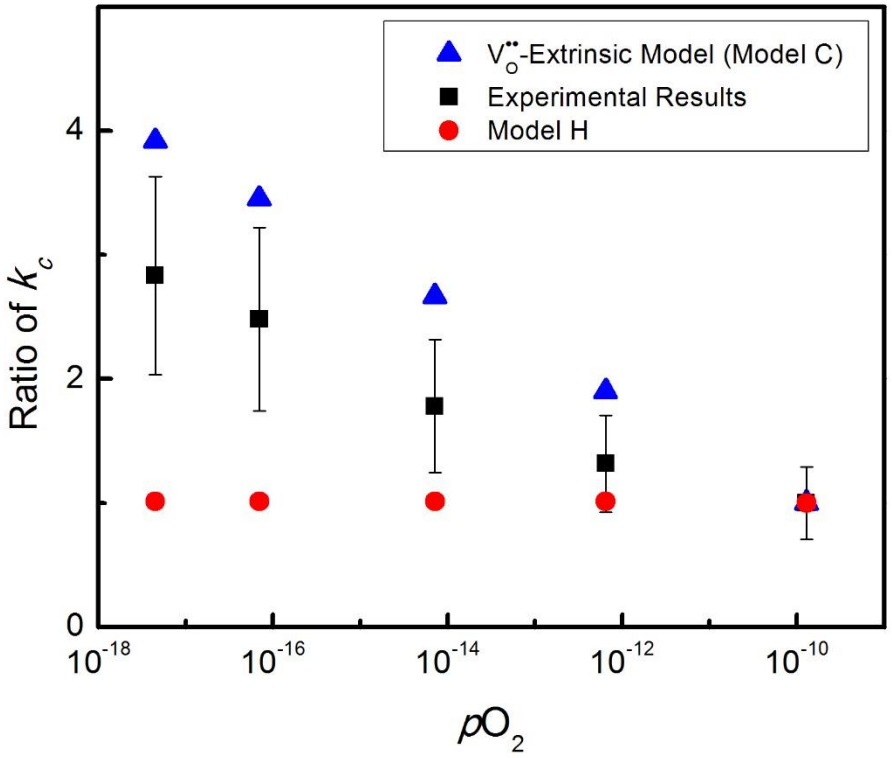

Figure 5.19 Graph of k_c ratios, $k_c/k_c(P_{O_2}=1.3\times10^{-10})$, as a function of external P_{O_2}. Experimental results and predictions from the oxygen vacancy-extrinsic model and model H are depicted. Model H assumes aluminum vacancies are rate-limiting species, and their concentration is determined by P_{O_2}.

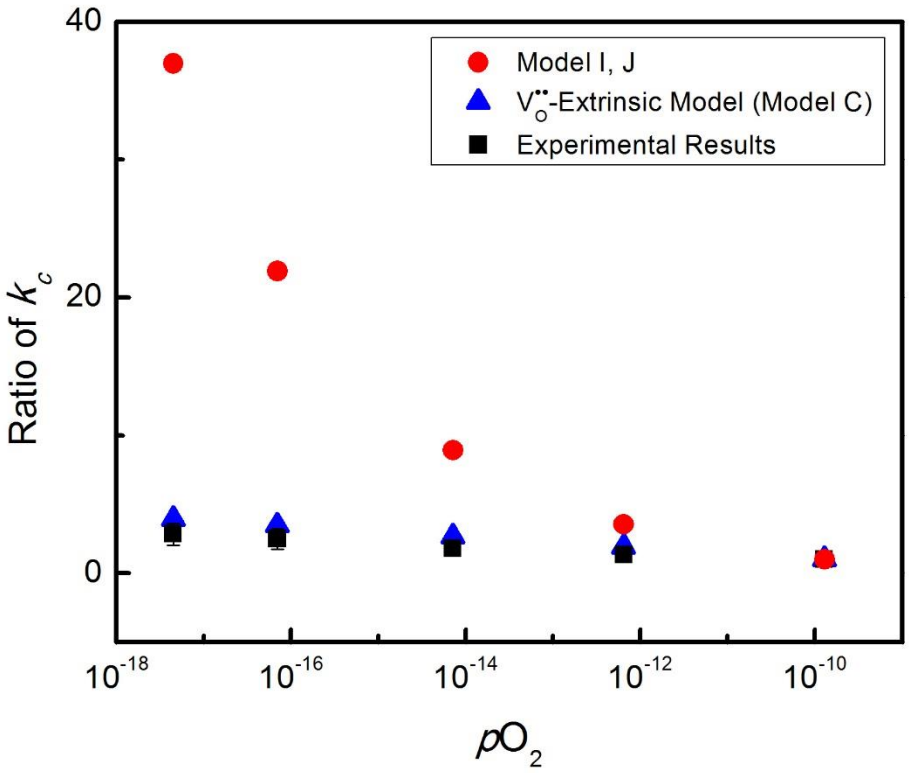

Figure 5.20 Graph of k_c ratios, $k_c/k_c(P_{O_2}=1.3\times10^{-10})$, as a function of external P_{O_2}. Experimental results and predictions from the oxygen vacancy-extrinsic model, model I and J are depicted. Model I assumes electrons are rate-limiting species, and their concentration is determined by P_{O_2}. Model J assumes aluminum interstitials are rate-limiting species, and their concentration is determined by P_{O_2}.

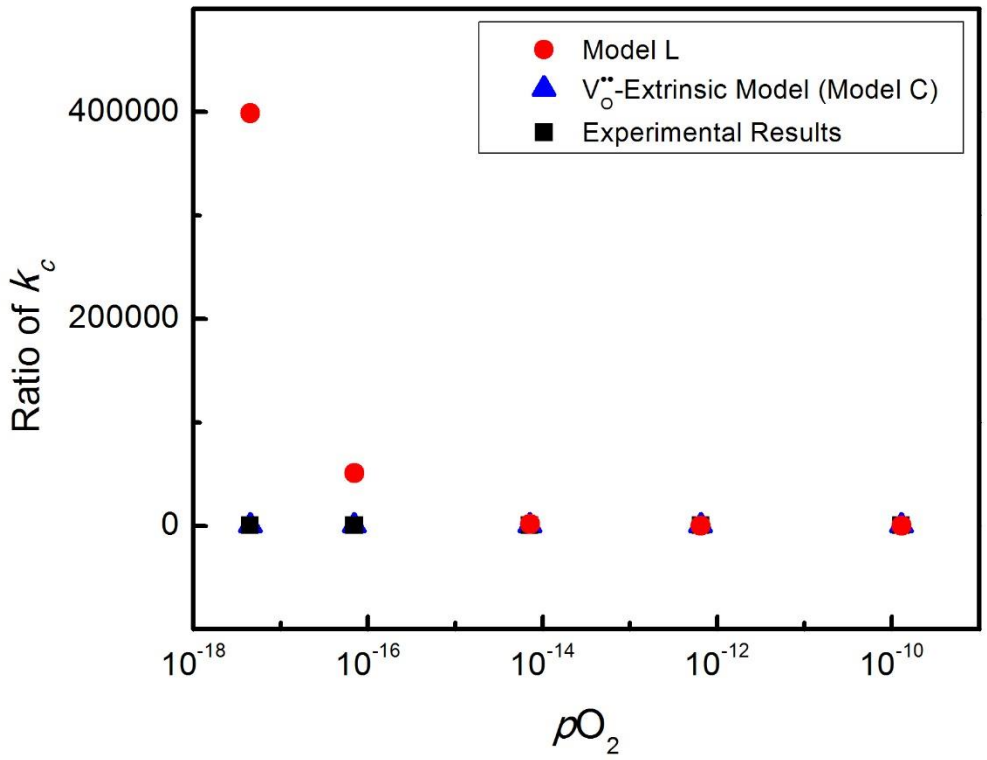

Figure 5.21 Graph of k_c ratios, $k_c/k_c(P_{O_2}=1.3\times10^{-10})$, as a function of external P_{O_2}. Experimental results and predictions from the oxygen vacancy-extrinsic model and model L are depicted. Model L assumes aluminum interstitials are rate-limiting species, and their concentration is determined by P_{O_2}.

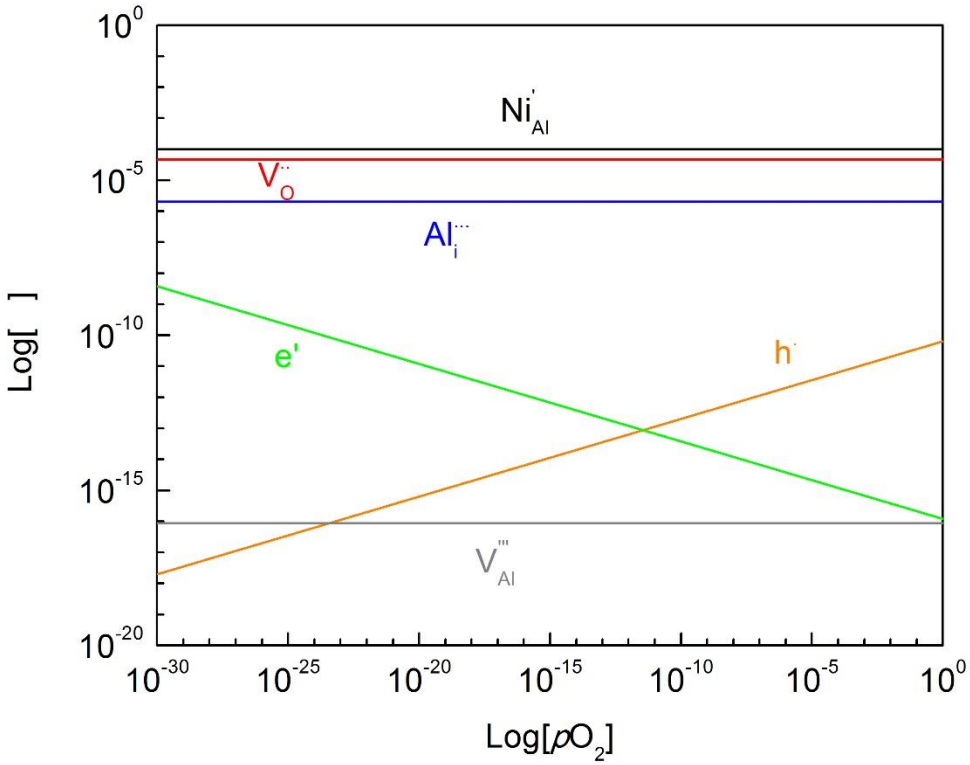

Figure 5.22 Brouwer diagram for Ni-doped alumina. The numbers were calculated using the formation energy of defects from Kroger et al[43,52] as formation enthalpy and using 0.5meV/K for each defect and 2meV/k for O_2 as formation entropy.[48,60] The solubility of Ni in alumina is assumed to be 100ppm for the calculation.

5.1.4.3 Comparison of k_c between Reduction Experiments and Oxidation Experiments

The corrected rate constants measured in reduction experiments were also compared with the rate constants measured in oxidation experiments. Table 5.9 shows the oxidation rate constants of undoped, 500ppm Y-doped and 500ppm Hf-doped alumina samples oxidized at 1400°C along with the reduction rate constants of undoped alumina samples reduced at 1400°C under P_{O_2}=7.2×10^{-15}. The data of undoped (oxidation) and 500ppm Y-doped (oxidation) is from Cheng et al.[15]. The reason to compare the oxidation rate constants with reduction rate constant under P_{O_2}=7.2×10^{-15} is that the driving force for these two conditions are quite similar. To calculate the driving force for oxidation experiments, $P_{O_2}^{low}$ was taken as 4.7×10^{-8}, which is the equilibrium P_{O_2} for Ni, $NiAl_2O_4$ and Al_2O_3 at 1400°C used as $P_{O_2}^{high}$ for reduction experiments. The oxidation k_c of undoped samples is 5 times larger than the reduction k_c, while the oxidation k_c of Y-doped and Hf-doped samples are smaller than the reduction k_c.

The discrepancy between the undoped samples under oxidation and reduction is unknown. One possible explanation is that since Ni outward diffusion left pores inside the oxidized samples, these pores provided fast path for oxygen diffusion and increase the oxygen chemical potential gradient, which helped oxygen diffuse inward and result in a higher k_c during oxidation. Another possible explanation is that under oxidation and reduction conditions, the oxidation state of Ni is different, which had different effects on GB transport in alumina. During oxidation, Ni was at its oxidized form in the oxidized region. Cheng et al. showed that the presence of Ni^{2+} at GBs increased oxidation k_c[94].

During reduction, Ni was at its metallic form in the reduced region, in which GB transport may not be promoted as much as the region having Ni^{2+}. Also, the driving force in oxidation experiments may be much larger than the calculated values in Table 5.6. Since the sample was sintered initially in an SPS at a very low P_{O_2} condition, the P_{O_2} inside the sample was lower than 4.7×10^{-8}, the P_{O_2} at the Ni particles while they were oxidizing. The larger driving force could explain that the oxidation rate was faster than reduction rate. More oxidation experiments on undoped samples under different P_{O_2} are needed to explain the discrepancy.

Figure 5.23 shows the ratio between k_c and the driving force of these samples. The value of the ratio represents the kinetics of the transport by assuming the kinetics is independent of P_{O_2}. Y-doping and Hf-doping effectively reduce the transport rate, which will be discussed further below.

Table 5.9 Corrected rate constants of different samples with similar driving force. The data of undoped (oxidation) and 500ppm Y-doped (oxidation) is from Cheng et al.[15].

Sample	k_c (m²/s)	$\ln P_{O_2}^{high} - \ln P_{O_2}^{low}$
Undoped (reduction P_{O_2}=7.2×10^{-15})	(3.3±0.7) ×10^{-19}	15.7
Undoped (oxidation P_{O_2}=1.0)	(1.6±0.2) ×10^{-18}	16.9
500ppm Y-doped (oxidation P_{O_2}=1.0)	(3.1±0.6) ×10^{-19}	16.9
500ppm Hf-doped (oxidation P_{O_2}=1.0)	(2.3±0.6) ×10^{-19}	16.9
500ppm Hf-doped (oxidation P_{O_2}=1.0×10^{-3})	(1.4±0.4) ×10^{-19}	10.0

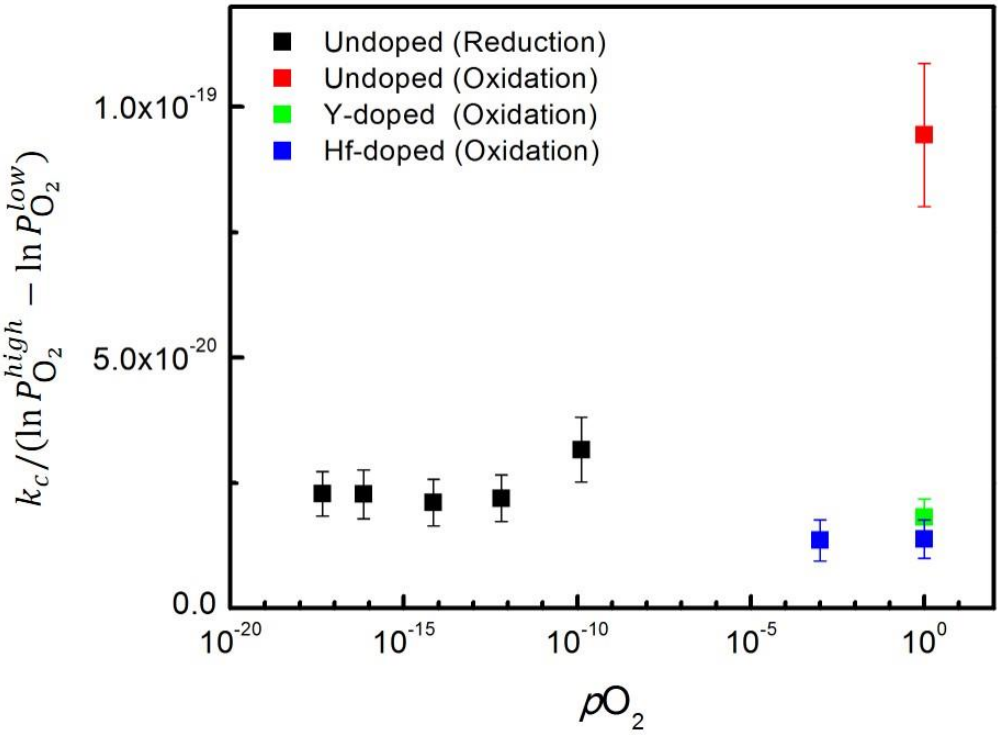

Figure 5.23 The ratio between k_c and the driving force of the transport, ln($P_{O_2}^{high}$)-ln($P_{O_2}^{low}$), as a function of P_{O_2}under different conditions.

5.2 Effect of Temperature on Grain Boundary Transport in HfO_2 Doped Alumina-Ni Samples

We next examine the dependence of the rate constants in Hf-doped alumina-Ni samples on temperature and grain boundary structures. The mechanism leading to the decrease in the grain boundary diffusivity and the correlation between kinetic properties and grain boundary structures will be discussed.

5.2.1 Microstructure

Figure 5.24 shows an SEM image of an as-sintered 500ppm Hf-doped alumina-Ni sample. There are two kinds of particles uniformly distributed in the alumina matrix. The larger ones are Ni particles with average particle size of 0.5μm, and the smaller ones are HfO_2 particles with average particle size of 0.1μm. The volume fraction of the Ni particles is 0.5%, which is as same as the targeting volume fraction from doping.

Figure 5.25 shows an SEM image of the surface of a 500ppm Hf-doped alumina-Ni sample oxidized at 1400°C for 5h. The bright particles on the surface are Ni spinel particles. There are also Ni spinel particles at the triple junctions and grain boundaries. The average area fraction of these particles is about 10%. If all the spinel particles were formed from the Ni particles on the surface, the area fraction should be 3%. This indicates that there was Ni outward diffusion in Hf-doped samples. Grain growth is minimal during oxidation. There was no abnormal grain growth observed in oxidized samples. Table 5.10 shows the average grain size of samples after oxidation at each temperature.

Figure 5.26 shows the comparison of the surfaces of an undoped alumina-Ni sample and a 500ppm Hf-doped alumina-Ni sample oxidized at 1300°C for 6h. There were relatively

fewer Ni spinel particles formed on the surface of the Hf-doped sample. This result suggests that Hf-doping effectively retards the outward diffusion of Ni.

Figure 5.27 shows an SEM image of the cross section of a 500ppm Hf-doped alumina-Ni sample oxidized at 1400°C for 5h. The oxidation front can be easily located due to the distinguished contrast of Ni spinel particles and Ni particles. In the region between the surface and the oxidation front, Ni spinel particles were formed, as shown in grey color. On the other side of the front, Ni particles maintained their metallic form, as shown in bright color. The magnified image at the oxidation front shows most oxidized particles were fully oxidized. This indicates that diffusion determines the overall oxidation process. The oxidation depth was measured to calculate the rate constant. Figure 5.27 also shows porosity in the oxidized region. The formation of the pores was due to the Ni outward diffusion, which is consistent with the observation of the Ni spinel particles on the surface of the samples after oxidation.

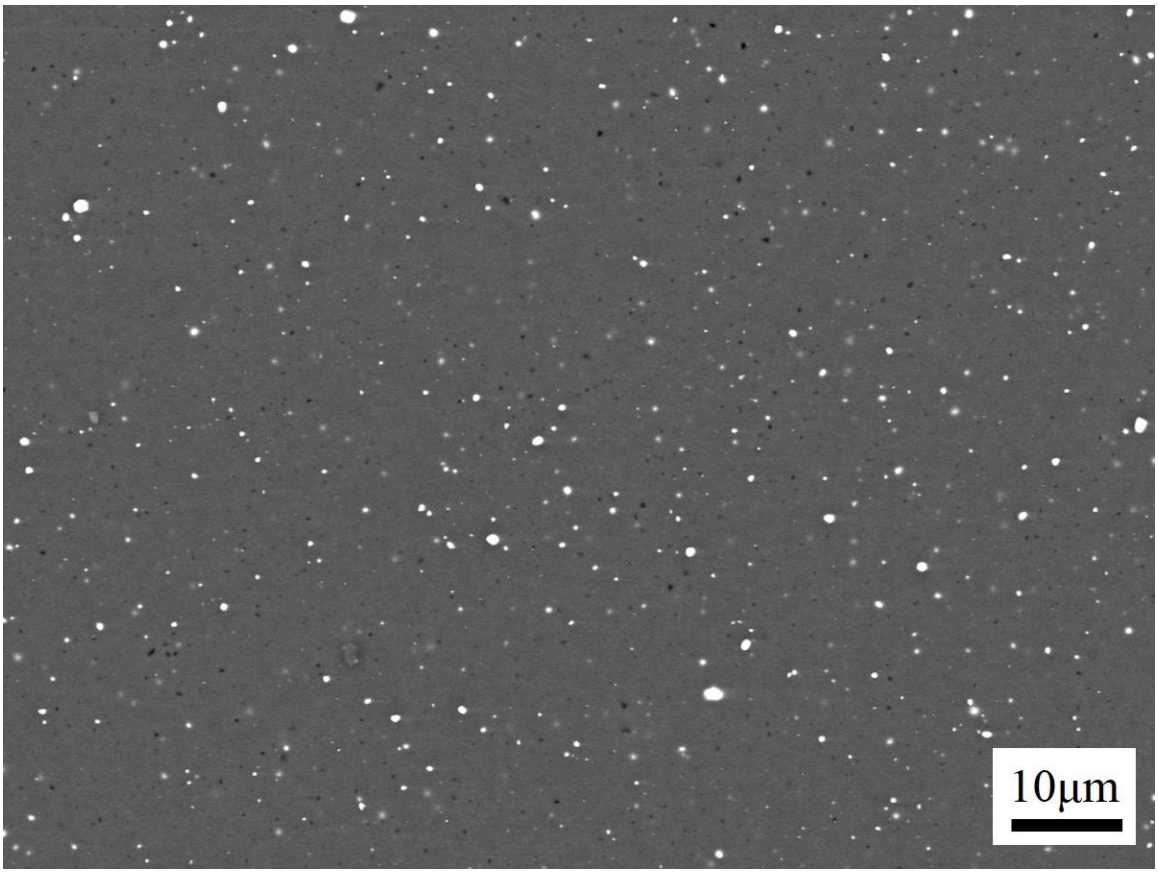

Figure 5.24 SEM image of a 500ppm Hf-doped alumina-Ni sample sintered at 1400°C in SPS.

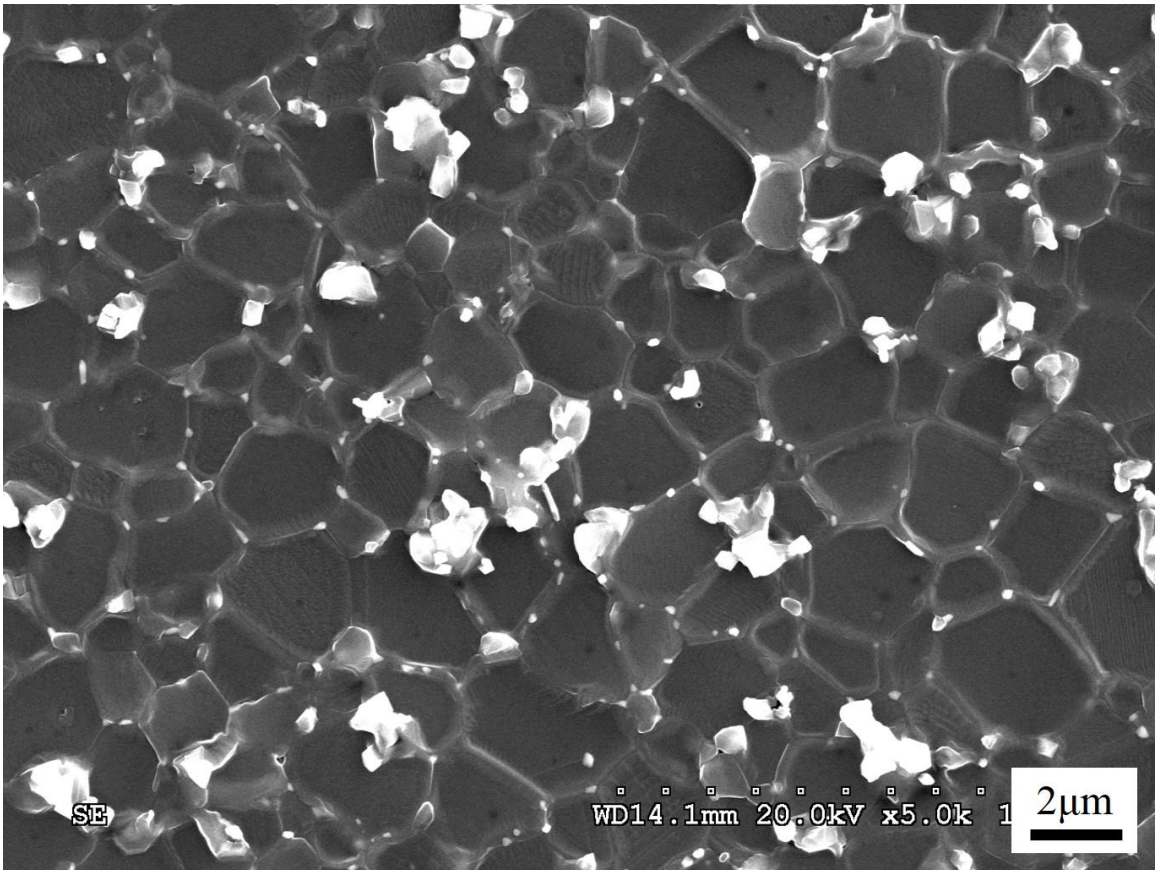

Figure 5.25 SEM image of the surface of a 500ppm Hf-doped alumina-Ni sample oxidized at 1400°C for 5h.

Table 5.10 Average grain size of 500ppm Hf-doped alumina-Ni samples oxidized at different temperatures. The results shown for 1250°C, 1320°C and 1400°C were from Wu[17].

***T* (°C)**	**Average G (μm)**
1400	4.9±0.6
1320	1.8±0.4
1250	4.3±0.9
1200	2.5±0.4
1150	2.2±0.4
1120	2.2±0.4
1095	2.1±0.4

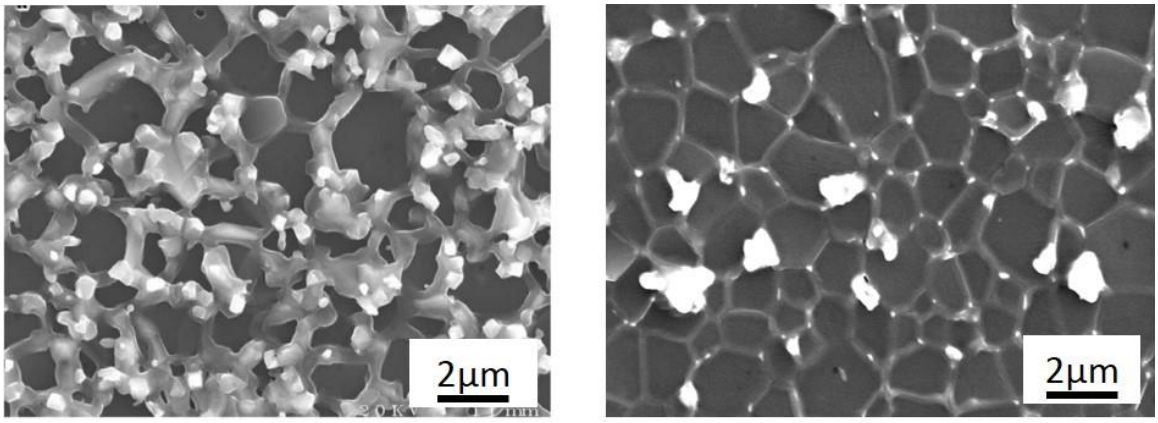

Figure 5.26 Surfaces of an undoped alumina-Ni and a 500ppm Hf-doped alumina-Ni sample after oxidation at 1300°C for 6h. The image of undoped alumina-Ni was from Cheng[95].

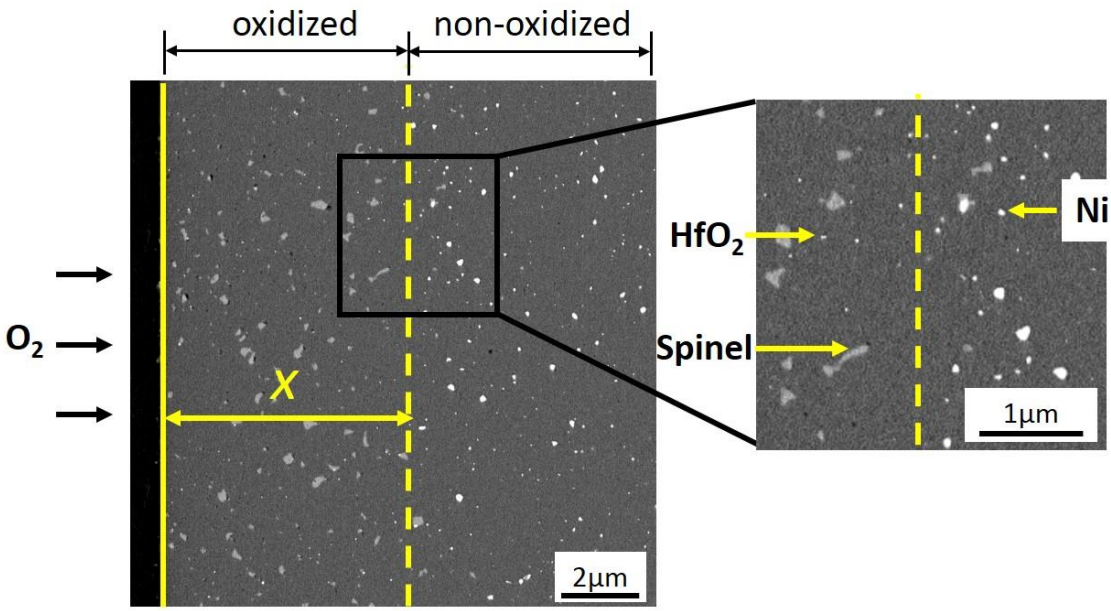

Figure 5.27 SEM images of the cross section of a 500ppm Hf-doped alumina-Ni sample oxidized at 1400°C for 5h.

5.2.2 Oxidation Rates

500ppm Hf-doped alumina-Ni samples were oxidized at seven different temperatures from 1095°C to 1400°C. At each temperature, samples were annealed for different times to measure the oxidation rate at that temperature. As mentioned earlier, the microstructure at the oxidation front indicated that diffusion controlled the overall oxidation process. So, for each sample, the square of oxidation depth was plotted with the oxidation time. Figure 5.28 shows these plots for samples oxidized at seven different temperatures. The linear relationship is consistent with diffusional transport as the rate controlling process. It should be noted that the rate constant at each temperature is given by the slope of the line corresponding to that temperature; the rate constants can be calculated by Eq. (5.2).

Having extracted the rate constants, the corresponding values were compared at different temperatures. The results for 1250°C, 1320°C and 1400°C were from earlier work by Wu[17]. To compare samples having different grain sizes, Eq. (5.3) was used to calculate the corrected rate constants. Table 5.11 shows the corrected rate constants at different temperatures. Figure 5.29 shows the corrected rate constants of undoped alumina-Ni and 500ppm Hf-doped alumina-Ni samples. The results of undoped alumina-Ni samples were from the earlier work of Cheng[15]. Clearly, for the temperature range considered here, Hf-doping decreases the oxidation rate in the alumina-Ni samples. We found that the activation energy for transport in undoped alumina-Ni samples is (450±10)kJ/mol, and the activation energy for transport in 500ppm Hf-doped samples is (540±15)kJ/mol using the results at all the temperatures. As discussed below, it is possible that the 500ppm Hf-doped alumina-Ni system undergoes a complexion transition. In that case, the activation energy

is (480±40)kJ/mol for the Hf-doped samples oxidized from 1250°C to 1400°C. For the Hf-doped samples oxidized from 1095°C to 1200°C, the activation energy is (480±50)kJ/mol.

Figure 5.30 shows the ratios of k_c between undoped alumina-Ni samples and 500ppm Hf-doped alumina-Ni samples at different temperatures. At temperatures above 1250°C, the ratios were about 10, while the ratios increase from 10 to 30 below 1200°C, indicating a more beneficial effect of Hf doping on slowing down the oxidation rate in alumina-Ni samples.

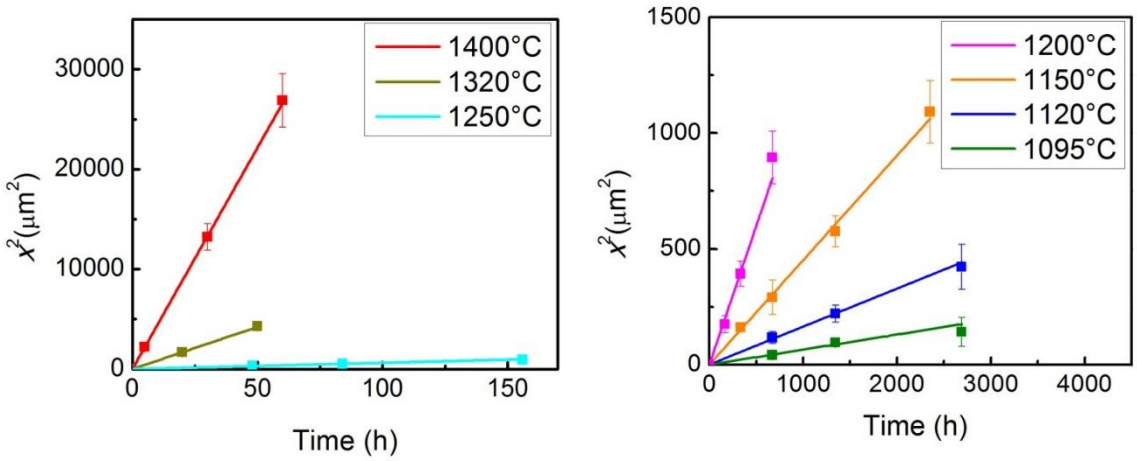

Figure 5.28 Plot of the square of the oxidation depth of 500ppm Hf-doped alumina-Ni samples versus oxidation time at seven different temperatures. The results from 1250°C, 1320°C and 1400°C were from Wu[17].

Table 5.11 Corrected rate constants of 500ppm Hf-doped alumina-Ni samples at different temperatures. The results for 1250°C, 1320°C and 1400°C were taken from the work of Wu[17].

T (°C)	k_c (m^2/s)
1400	$(2.2\pm0.3)\times10^{-19}$
1320	$(4.3\pm1.1)\times10^{-20}$
1250	$(7.3\pm1.6)\times10^{-21}$
1200	$(8.3\pm1.6)\times10^{-22}$
1150	$(2.7\pm0.5)\times10^{-22}$
1120	$(1.0\pm0.2)\times10^{-22}$
1095	$(3.8\pm0.9)\times10^{-23}$

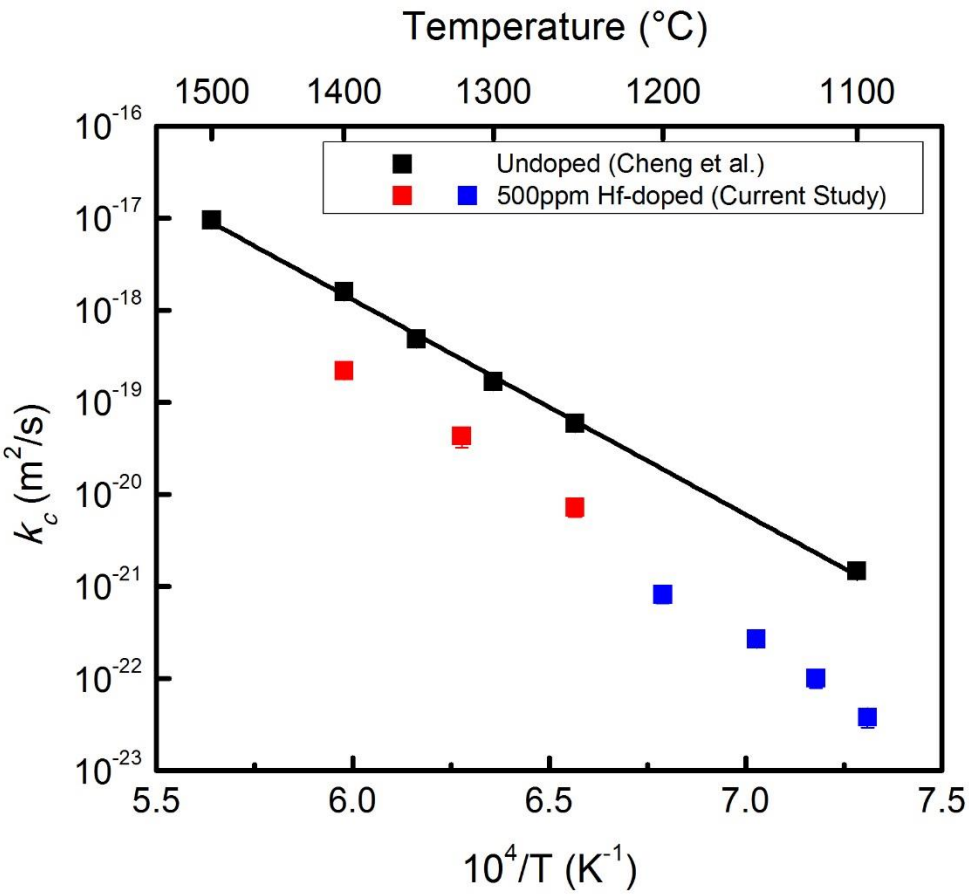

Figure 5.29 Corrected rate constants of undoped alumina-Ni and 500ppm Hf-doped alumina-Ni samples at different temperatures. The results for undoped alumina-Ni samples were from Cheng et al.[15].The results for 500ppm Hf-doped alumina-Ni samples at 1250°C, 1320°C and 1400°C were from Wu[17].

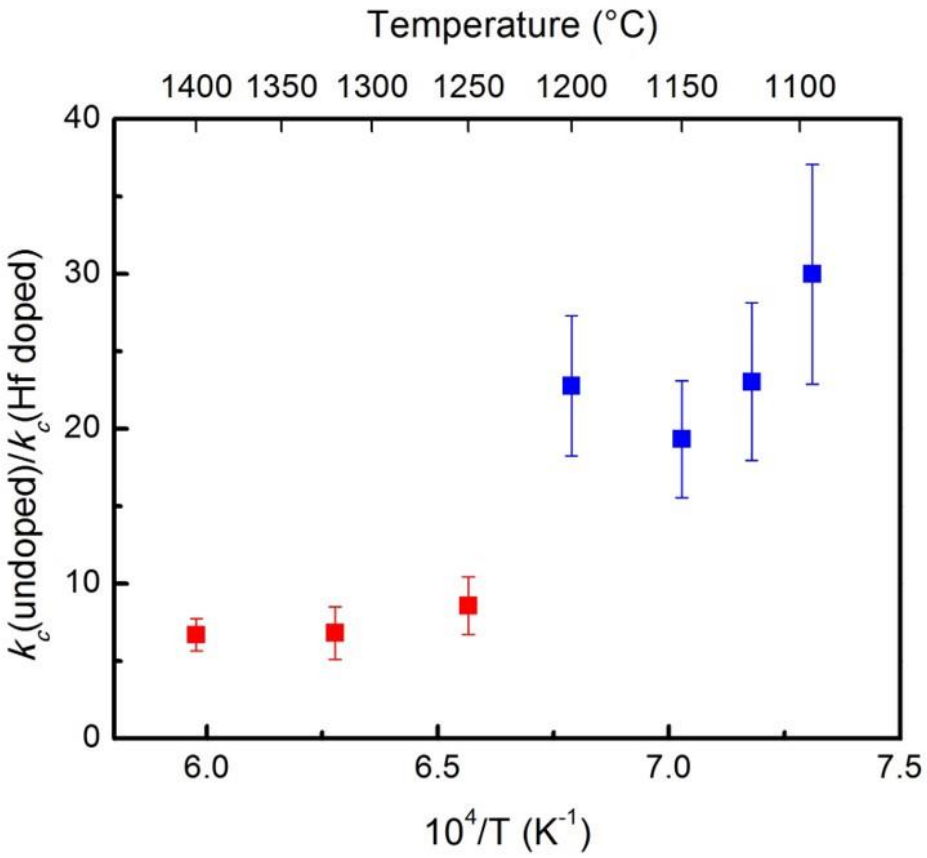

Figure 5.30 Ratios of corrected rate constants between undoped and 500ppm Hf-doped alumina-Ni samples at different temperatures.

5.2.3 Grain Boundary Structures

To understand how Hf-doping slows grain boundary transport in alumina, grain boundary structures in 500ppm Hf-doped alumina-Ni samples oxidized at 1400°C and 1150°C were examined.

Yu et al. have studied the segregation behavior of Hf^{4+} at grain boundaries in alumina[96]. Figure 5.31 shows a HAADF STEM image of a grain boundary in a 500ppm Hf-doped alumina-Ni sample oxidized at 1400°C for 5h. Together with EDS results, the bright dots at the GB were confirmed to be Hf^{4+} ions. Confirmed with DFT calculation, Hf^{4+} occupy Al^{3+} site at the GB. Moreover, using focal series imaging, it was confirmed that a monolayer of Hf^{4+}segregated on the surface of the GB. The GB in Figure 5.31 also exhibits strong faceting behavior along (2-1-10) direction.

For additional analysis, structures comprising 22 random GBs in 500ppm Hf-doped samples oxidized at 1150°C and 1400°C were characterized. (We note that Dr. Z. Yu collaborated in part of this work). Among all the characterized GBs, Hf^{4+} segregated at Al^{3+} sites, and some GBs exhibit faceting behavior while others did not. The latter boundaries were labeled as rough. Figure 5.32 shows two HAADF STEM images of GBs in Hf-doped samples oxidized at 1400°C. With one of the adjacent grains at different zone axes, both two GBs exhibits faceting behavior along (2-1-10). Figure 5.33 shows two HAADF STEM images of another two GBs in Hf-doped samples oxidized at 1400°C. Both GBs are non-facetted. Figure 5.34 shows two HAADF STEM images of two GBs in Hf-doped samples oxidized at 1150°C. Although both GBs exhibit faceting behavior, the faceting planes are different.

The faceting behavior of the characterized GBs were summarized in the form of a facet plane distribution for samples oxidized at 1400°C and 1150°C, respectively. The non-facetted GBs were labeled as rough. Figure 5.35 shows pie charts representing the facet plane distribution for samples oxidized at 1400°C and 1150°C. At 1400°C, a high frequency of grain boundaries exhibit (2-1-10) facets while, at 1150°C, a large proportion of boundaries is rough. The difference in the distribution of facet planes may correlate with the varying benefits of Hf-doping in decreasing oxidation rate in alumina.

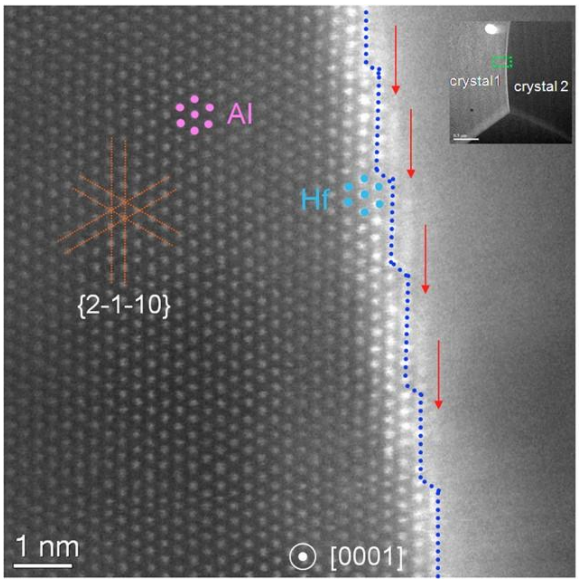

Figure 5.31 HAADF STEM image of a GB in a 500ppm Hf-doped alumina-Ni sample oxidized at 1400°C[96].

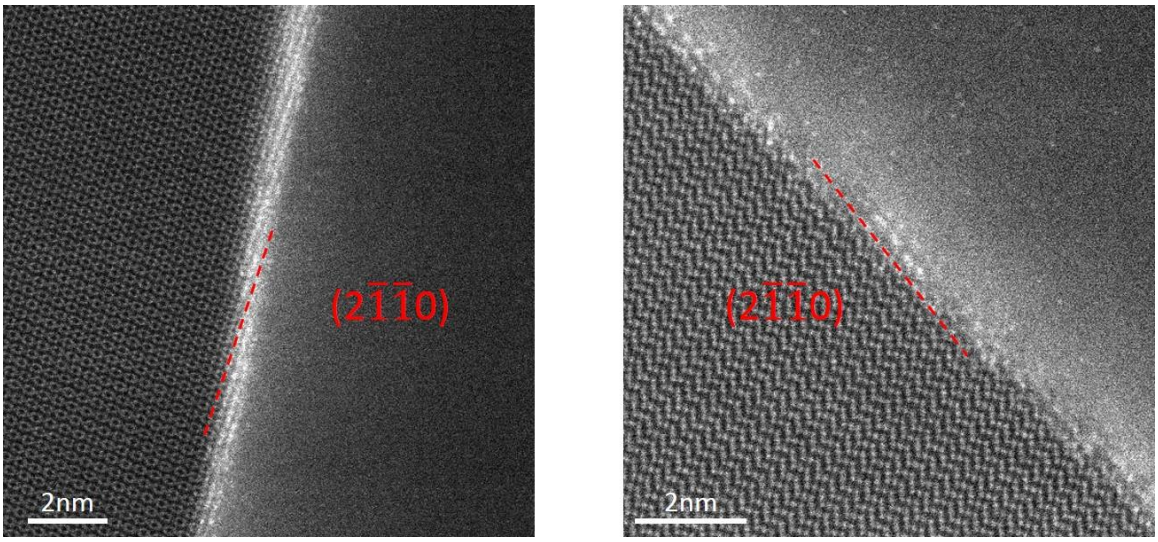

Figure 5.32 HAADF STEM images of faceted GBs in 500ppm Hf-doped alumina-Ni samples oxidized at 1400°C.

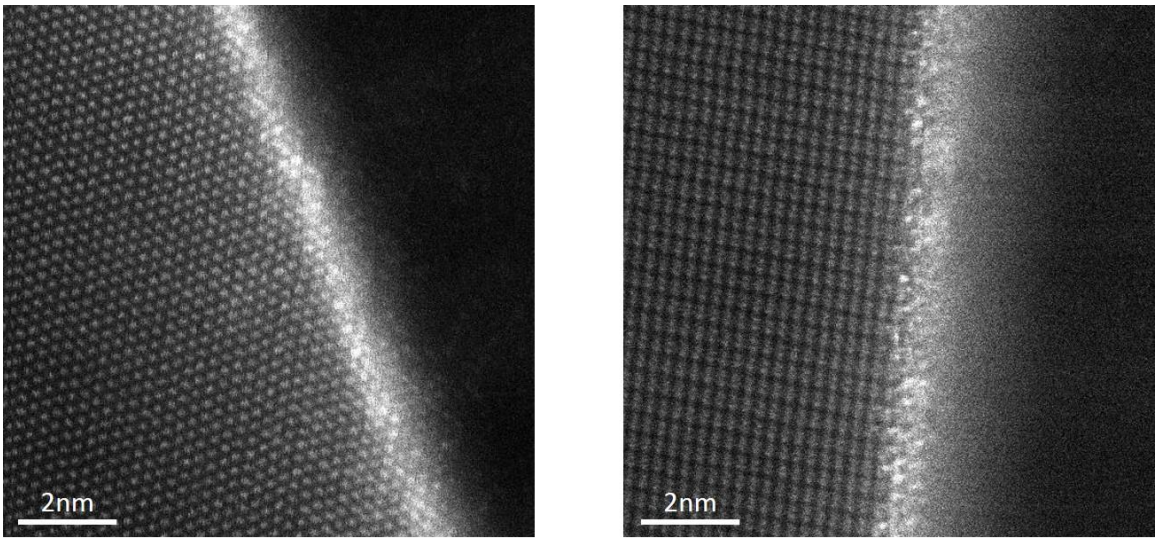

Figure 5.33 HAADF STEM images of rough (non-faceted) GBs in 500ppm Hf-doped alumina-Ni samples oxidized at 1400°C.

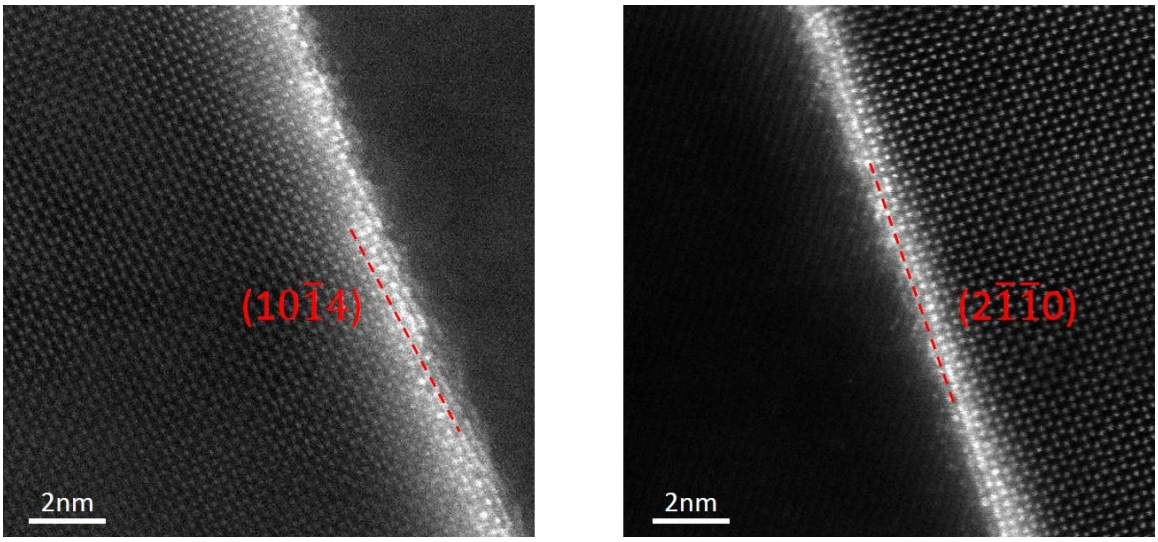

Figure 5.34 HAADF STEM images of faceted GBs in 500ppm Hf-doped alumina-Ni samples oxidized at 1150°C.

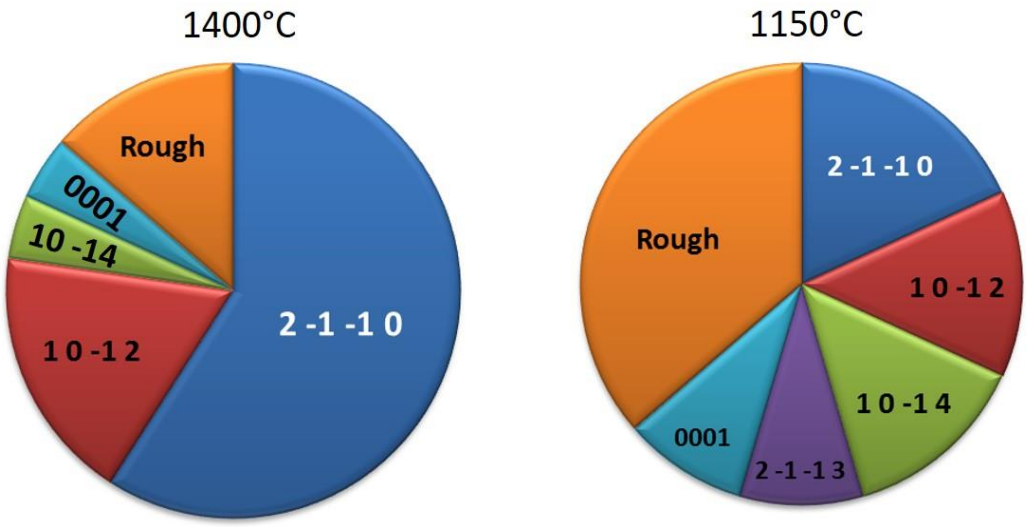

Figure 5.35 Facet plane distributions for 500ppm Hf-doped alumina-Ni samples oxidized at1400°C and 1150°C.

5.2.4 Discussion

Based on these results, the discussion here will have two foci, namely: 1.) understanding the effect of Hf-doping on grain boundary transport in alumina, and 2.) understanding the role of Hf-doping in decreasing the oxidation rate in alumina at different temperatures.

5.2.4.1 Effects of Hf-doping on Grain Boundary Transport in Alumina

Figure 5.29 clearly showed that Hf-doping effectively slows down the oxidation rate in alumina. This effect of Hf-doping could be a combination of retarding cation GB diffusion and anion GB diffusion in alumina.

The effect of Hf on cation GB diffusion can be explained by a site-blocking mechanism. In this study, atomic resolution HAADF STEM images showed that Hf^{4+} occupies Al^{3+} site at GBs. Hf^{4+} at GBs could block diffusion path of cations in alumina GBs. Figure 5.25 shows that Hf-doping retards Ni outward diffusion, which supports the site-blocking mechanism. This is consistent with the previous work on the effect of RE on grain boundary transport in alumina.

A previous study of the impact of Hf^{4+} concentration on grain boundary transport in alumina showed that the ratio of oxidation rate between undoped and Hf-doped alumina-Ni samples has a linear relationship with the grain boundary coverage ratio of Hf^{4+} prior to saturation[16]. The results were rationalized with reference to the theoretical work by Saxton[97], who calculated the ratio between the value of the obstructed and unobstructed diffusion coefficient, D*, as a function of obstacle concentration C, for various 2-D lattice geometries. Saxton found that the diffusion results could be represented by the relationship

$D^* = 1-C/C_p$, where C_p is the percolation threshold. The ratio of oxidation rates is analogous to D*, and thus the impact of Hf doping on grain boundary transport in alumina is consistent with site-blocking mechanism.

Creep studies in alumina have also shown that the effect of RE dopants on the decreasing creep rate in alumina is consistent with site-blocking mechanism[63]. Al GB diffusion was believed to determine the creep rate in alumina. Simulation results showed that outsize ions segregating at GBs could block a few critical diffusive pathways of Al GB diffusion, which is again consistent with the site-blocking mechanism.

The effect of Hf-doping on anion GB diffusion is more complex. The results from the current study alone cannot provide an unambiguous determination as to how Hf-doping affects oxygen GB diffusion in alumina due to the presence of Ni in the system. From the view of defect chemistry, Hf-doping could simply just counteract the effect of Ni on oxygen GB diffusion. Ni^{2+} in alumina introduces oxygen vacancy. With higher oxygen vacancy concentration, oxygen GB diffusion is expected to be faster. And doping with Hf^{4+} could compensate the effect of Ni^{2+}, resulting in a lower oxygen vacancy concentration and thus slower oxygen GB diffusion. Therefore, the effect of Hf-doping on compensating the effect of Ni and on slowing down oxygen GB diffusion in undoped alumina could not be separated from current results.

However, it can be shown that Hf-doping decreases oxygen inward diffusion in alumina based the results in literature and in the current study. Cheng et al.[94] showed that the presence of Ni alone enhanced transport by a factor of 2 relative to that for undoped alumina at 1300°C by comparing the rate constant in Ni doped alumina and undoped

alumina using a wedge-geometry bilayer sample setup. At 1320°C, the benefit of Hf-doping is about 7. Assuming that doping with Ni would not decrease the oxidation rate in Hf-doped alumina, Hf-doping decreases the oxidation rate in undoped alumina by at least a factor of 3.5. Cheng et al.[94] estimated the contribution of Ni outward diffusion during oxidation is about 22% at 1300°C. Moreover, two-stage oxidation experiments showed that the contribution of Al outward diffusion to the overall oxidation is about 50% without RE doping and less than 20% with RE doping[10]. These results indicate that the effect of Hf-doping on decreasing the oxidation rate in alumina by a factor of 3.5 is not purely due to the retardation of cation diffusion, which suggests that Hf-doping slows down oxygen GB diffusion as well in alumina.

This contradicts the results of recent high temperature oxygen permeation experiments which showed that oxygen GB diffusivity was the same in 0.2% HfO_2-doped alumina and undoped alumina, and dependent on P_{O_2} according to intrinsic[7]. 5.1.4.2.3 showed that the dependence they found is not due to intrinsic. It could be from the change in GB chemistry at a high temperature, which may explain that oxygen GB diffusivity in 0.2% HfO_2-doped alumina was as same as in undoped alumina.

The effect of Hf-doping on slowing down oxygen GB diffusion in alumina can be explained by, for example, one or more of the following: a site-blocking mechanism, a bond-strengthening mechanism, a point defect chemistry mechanism and a GB structure transition mechanism. As mentioned earlier, effect of Hf^{4+} concentration on grain boundary transport in alumina can be rationalized by site-blocking mechanism. The presence of Hf^{4+} at GBs could block diffusion pathways of oxygen and increase the activation energy of

oxygen GB diffusion. Since the bonding energy between Hf and O (801kJ/mol) is higher than that between Al and O (501kJ/mol)[60]. It is reasonable to expect oxygen GB diffusion involves overcoming a higher activation energy with the presence of Hf. Also, from the point of view of defect chemistry, the presence of Hf^{4+} in alumina introduces Al vacancies, and results in lowering the concentration of O vacancies based on Schottky defect equilibrium. This could also explain the effect of Hf-doping on retarding oxygen GB diffusion in alumina. Last, Hf-doping may change the GB structure of alumina, which could result in changing oxygen GB diffusion in alumina. As shown in the next section, GBs with different structures may correlate with different kinetic properties in Hf-doped alumina.

The discussion above assumes that it is ionic diffusion that determines the overall oxidation process in alumina. As mentioned earlier, it is still not clear to what content this assumption is valid. To understand this effect of Hf-doping on the oxidation rate in alumina, the transport mechanisms in alumina needs to be better understood.

5.2.4.2 Effect of Temperature on Oxidation Rates in Hf-doped Alumina

Figure 5.35 shows that a larger proportion of boundaries was rough at a lower temperature. The reason of this phenomena is still unknown. Assuming all the GBs were at thermodynamically stable states, GBs typically tends to become rougher at higher temperatures. But the GB chemistry may also change as temperature increases, which could influence the thermodynamic states of the GBs. Kelly et al. found the relative grain-boundary energies of Y-doped Al_2O_3 overall increases with increased temperature, attributed to a reduction in the grain boundary excess at higher temperature[98]. It is possible that the GB excess of Hf at different temperatures were different, which results in the structures of the GBs.

Figure 5.30 shows varying effects of Hf-doping on oxidation rate at different temperatures. With a higher activation energy, Hf-doping would have greater benefit at lower temperatures. However, the observation of different facet plane distributions at corresponding temperatures shown in Figure 5.35 may correlate with the abrupt change in the beneficial effect of Hf-doping. These results together suggest it is possible that 500ppm Hf-doped alumina undergoes a complexion transition at temperature between 1200°C and 1250°C.

Complexion transitions in alumina have been found in many systems[69]. Dillon and Harmer studied grain boundary mobility in alumina over a large range of temperature and chemistry, and found that each type of complexions have unique grain boundary structure, which determines the transport property of that GB. Complexion transitions could result in a change of overall transport behaviors.

More recently, complexion transitions have also been found in several RE-doped alumina systems. Bojarski et al. studied the grain growth behavior in 450ppm Y-doped alumina and found a complexion transition happening between 1450°C and 1600°C[68,99]. At 1450°C and 1600°C, all the grains exhibit unimodal grain size, but the average grain size is much larger in the sample s annealed at 1600°C. At 1500°C, where not all the GBs have transformed to high temperature complexions, a bimodal grain size was observed. The coexistence of two or multiple complexions is the reason this abnormal grain growth behavior.

Behera et al.[100] also found a complexion transition in 180ppm wt% Zr-doped alumina. A discontinuous increase in grain boundary mobility by over an order of magnitude within a narrow temperature window between 1550 and 1650 C was revealed. The discontinuity is attributed to a grain boundary complexion transition that occurs at about 1600 C. Since Zr and Hf have very similar chemical properties, a complexion transition in Hf-doped alumina is expected. And since 180ppm wt% is still below the solubility limit of Zr in alumina, the complexion transition temperature for Zr-doped or Hf-doped alumina would decrease when the doping concentration is beyond the solubility.

If one assumes that a complexion transition happens between 1200°C and 1250°C in 500ppm Hf-doped alumina, the data in Figure 5.29 should be fitted by two lines. One line is for the data above 1250°C with the same complexion type, and the other is for the data below 1200°C. The activation energies corresponding to these two complexions are both about 480kJ/mol, which is very close to the activation energy of the undoped data (450kJ/mol). This is consistent with the findings by Dillon and Harmer[69]. But without

further confirmation, no definitive conclusion can be drawn. The relationship between general grain boundary structures and the corresponding transport properties needs to be established to fully understand the varying effect of Hf-doping on slowing down the oxidation rate in alumina.

CHAPTER 6 CONCLUSIONS

The first part of the work investigated the effect on P_{O_2} on grain boundary transport in alumina. Reduction experiment were used to measure reduction rate constants under a large variation of P_{O_2}. A higher rate constant was observed with a larger P_{O_2} gradient across the sample. Under the P_{O_2} range of the current study, it was shown that the effect of P_{O_2} on rate constants in alumina was mainly due to the P_{O_2} gradient, which was the driving force of the transport. P_{O_2} showed negligible effect on $\sigma t_{ion} t_e$ in the samples. The experimental results were also used to examine whether point defect models can explain grain boundary transport in alumina. It was found that at 1400°C or lower temperatures, the point defect model Kitaoka et al.[5–9] used to explain their results could not be applied to alumina scales. After examining all the possible point defect models, only the extrinsic model with ionic diffusion rate limiting was consistent with the experimental results. Transport mechanisms in alumina, the impact of bulk point defect concentration on grain boundary defect concentration, and the link between boundary defect concentration and transport need further study.

The second part of the work studied the effect of Hf-doping on the oxidation rate in alumina at temperatures from 1095°C to 1400°C. Ni markers were used to track the oxidation front and thereby determined the oxidation rate. It was found that Hf-doping effectively slowed down the oxidation rate in alumina with a factor of 10 from 1250°C to 1400°C, a factor of 20-30 from 1095°C to 1200°C. Grain boundary structures in Hf-doped samples oxidized at 1400°C and 1095°C were also characterized. The effect of Hf-doping on the retardation of grain boundary transport in alumina was consistent with a site-

blocking mechanism. Furthermore, the grain boundary facet plane distribution at different temperatures may correlate with the varying benefits of Hf-doping in decreasing the oxidation rate, and suggested a possible grain boundary complexion transition occurring in the system. Further study is needed to establish the general grain boundary structures and transport properties.

CHAPTER 7 SUGGESTED FUTURE WORK

To fully understand the transport mechanisms in polycrystalline alumina, the contribution of electronic conduction and ionic conduction must to be determined. This goal can be achieved by measuring electrical properties of the grown alumina during the oxidation of alumina forming alloys. These alloys need to have very high purity to avoid the effect of other ions on the transport in alumina. The goal can also be achieved by measuring electrical properties while conducting oxygen permeation experiments on undoped alumina. In these two experiments, the task of measuring electrical properties of alumina at high temperature is challenging.

To understand the effect of Hf-doping on slowing down grain boundary transport in alumina, the structure and chemistry of a grain boundary needs to be correlated to its transport behavior. A study on oxygen diffusion and structure of individual general grain boundary in alumina is proposed. Dense alumina sample with relatively larger grain size will be first annealed under ^{18}O environment. The annealing temperature and time need to be controlled so that, for most GBs, the diffusion depth of ^{18}O is less than the GB length. After annealing, the SIMS imaging technique can be used to trace ^{18}O concentration and diffusion depth in GBs. Interesting GBs can be labeled in SIMS as well. After that, TEM samples containing the GBs of interest can be made and the GBs characterized to study their structures and chemistries. The hope is that a correlation may be established.

CHAPTER 8 CONTRIBUTION

The first part of the work showed the effect of P_{O_2} on grain boundary transport in alumina. The effect of P_{O_2} on rate constants in alumina was mainly due to the P_{O_2} gradient, which was the driving force of the transport. P_{O_2} showed negligible effect on $\sigma t_{ion} t_e$ in the samples. The results of this study provided useful information to high temperature alloy engineers that reducing the P_{O_2} outside the scale can effectively decreases the oxidation rate of the alloy. The results also solved a scientific puzzle about the viability of applying an intrinsic nonstoichiometric point defect model to grain boundary transport in alumina. The results showed that the intrinsic nonstoichiometric model could not be applied to alumina at 1400°C or lower temperatures. Among all the possible defect models, only the extrinsic model with ionic diffusion as the rate limiting process was consistent with the experimental results.

The second part of the work showed the effect of Hf-doping on retarding the oxidation rate in alumina. Close to the condition where alumina scales grow on Ni-based supper alloys, with the presence of Ni, Hf-doping decreased the oxidation rate by a factor of 10 from 1250°C to 1400°C, and by a factor of 20-30 from 1095°C to 1200°C compared to undoped alumina. Observations of grain boundary structures in Hf-doped samples oxidized at 1400°C and 1150°C showed a difference in facet plane distributions. This difference in grain boundary structures may correlate with the varying effects of Hf-doping on retarding the oxidation rate in alumina at different temperatures.

APPENDIX A. CORRECTION OF THE REDUCTION DEPTH AS A FUNCTION OF ANNEALING TIME

Reduction rate was calculated using the measured reduction depth and the annealing time for each reduction experiment, as mentioned in 5.1.3. However, the annealing time is not simply the holding time set in the program on the furnace. There are two contributing factors to the deviation.

The first is the deviation of the actual temperature in the furnace from the programed temperature during the annealing. Figure A.1 shows the heating schedule and the measured temperature during annealing a sample at 1400°C under P_{O_2}=6.5×10^{-13} for 5h. Above 1000°C, the actual temperature started to deviate from the programmed temperature. And the actual temperature didn't reach 1400°C at the time as programmed. This could be due to the heat loss through the tube. The result was that the actual holding time at 1400°C was not 5h as programmed.

The second is that reduction started at temperature below 1400°C. Figure 5.29 showed that the activation energy of the oxidation of undoped Ni-alumina samples is about 450kJ/mol. It is reasonable to assume that the activation energy of the reduction process is the same. Under this assumption, the reduction rate at 1370°C is more than half of the reduction rate at 1400°C. Since the actual temperature between 1370°C and 1400°C was about 0.5h, the annealing time was not the time that 1400°C was held.

To calculate the reduction rate accurately, an annealing with short holding time was conducted under each P_{O_2} to correct the annealing times for the other experiments under the same P_{O_2}. During this short run, 1400° was assured to be reached. Figure A.2 shows

the measured temperature during annealing samples at 1400°C under P_{O_2}=6.5×10^{-13} for 1.5h and 5h. The actual temperature during ramping up and ramping down stages were almost identical in these two runs. The only difference between these two runs was the time that 1400°C was held for, which was 3.5h. With this information, the sample annealed for 5h can be treated as being annealed by two subsequent steps. First, the sample was annealed following the same procedure as the sample annealed for 1.5h, including the ramping up and ramping down stages. After this step, the reduction depth of the sample was as the same as the reduction depth of the one of the sample annealed for 1.5h, x(1.5h). Second, the sample was annealed purely at 1400°C for 3.5h. After this step, the reduction depth of the sample was measured as x(5h). Based on the Wagner's oxidation theory, the reduction depth, x, and the annealing time, t, follows Eq. (A.1) at a given temperature.

$$\int_{x_1}^{x_2} 2x dx = k \int_{t_1}^{t_2} dt \qquad (A.1)$$

where x_1 and x_2 are the corresponding reduction depths at time t_1 and t_2, and k is the rate constant. If t_1 and t_2 are the time the second step mentioned above started and finished, x(1.5h) and x(5h) are x_1 and x_2. k can be calculated by using Eq. (A.2).

$$x_2^2 - x_1^2 = k(t_2 - t_1) \qquad (A.2)$$

Under each P_{O_2}, the reduction rate was calculated using the analysis described above. The reduction depth, x_1, of a sample set to be annealed for a short time, t_1, was measured. The results, x_i and t_i, from all the experiments under the same P_{O_2} including x_1 and t_1 were corrected using x_1 and t_1. Reduction rate, k, was calculated by fitting $x_i^2 - x_1^2$ as a linear function of $t_i - t_1$. The results are shown in Figure 5.7 and Figure 5.8.

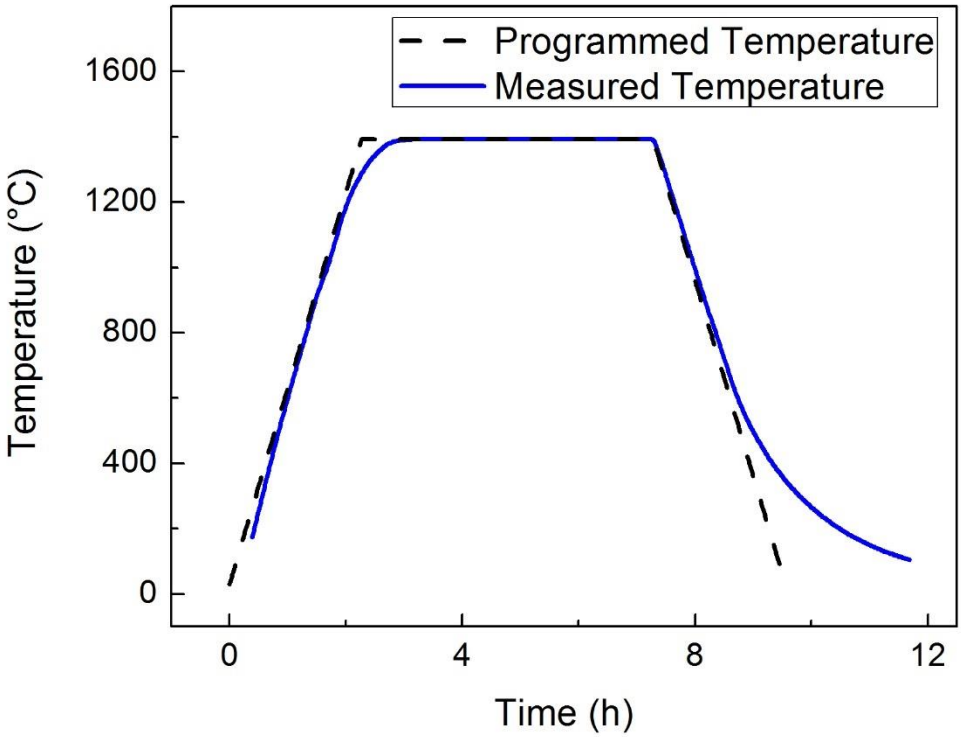

Figure A.1 Heating schedule and measured temperature during annealing a sample at 1400°C under P_{O_2}=6.5×10^{-13} for 5h. The furnace run started at 0h, 30°C.

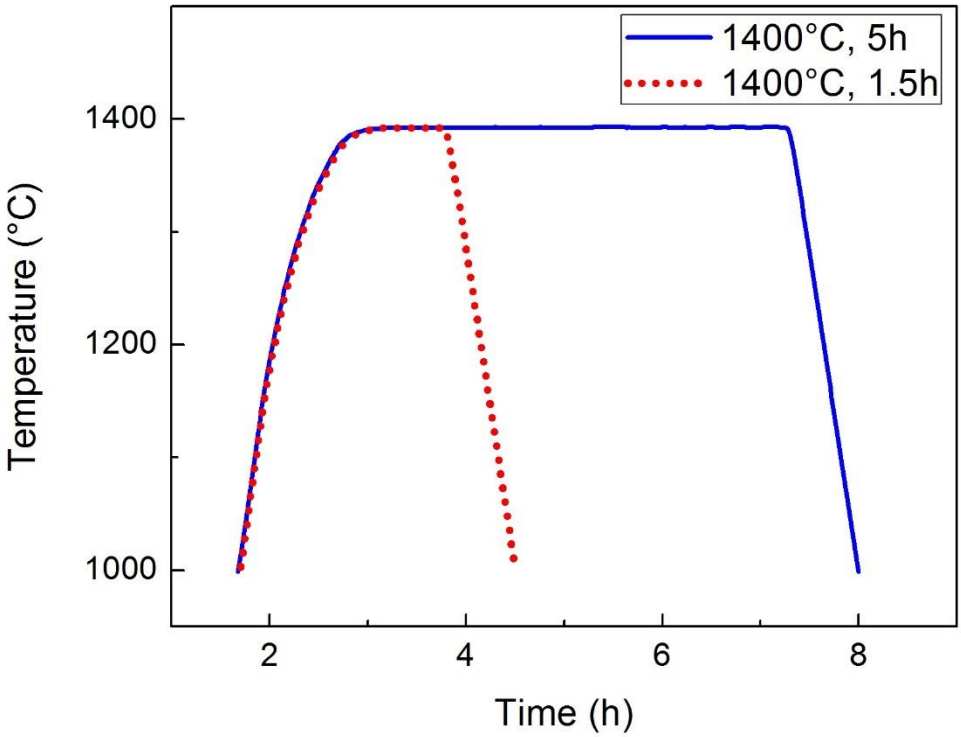

Figure A.2 Measured temperature during annealing samples at 1400°C under P_{O_2}=6.5×10^{-13} for 1.5h and 5h. Furnace runs started at 0h, 30°C.

BIBLIOGRAPHY

[1] N.P. Padture, M. Gell, E.H. Jordan, Thermal Barrier Coatings for Gas-Turbine Engine Applications, Science. 296 (2002) 280–284. doi:10.1126/science.1068609.

[2] D.R. Clarke, M. Oechsner, N.P. Padture, Thermal-barrier coatings for more efficient gas-turbine engines, MRS Bull. 37 (2012) 891–898. doi:10.1557/mrs.2012.232.

[3] A.G. Evans, D.R. Mumm, J.W. Hutchinson, G.H. Meier, F.S. Pettit, Mechanisms controlling the durability of thermal barrier coatings, Prog. Mater. Sci. 46 (2001) 505–553. doi:10.1016/S0079-6425(00)00020-7.

[4] N.S.J. James L. Smialek, Brian Gleeson, A.H.H. David B. Hovis, Oxygen Permeability and Grain-Boundary Diffusion Applied to Alumina Scales, (2013).

[5] S. Kitaoka, T. Matsudaira, M. Wada, Mass-Transfer Mechanism of Alumina Ceramics under Oxygen Potential Gradients at High Temperatures, Mater. Trans. 50 (2009) 1023–1031. doi:10.2320/matertrans.MC200803.

[6] T. Matsudaira, M. Wada, T. Saitoh, S. Kitaoka, The effect of lutetium dopant on oxygen permeability of alumina polycrystals under oxygen potential gradients at ultra-high temperatures, Acta Mater. 58 (2010) 1544–1553. doi:10.1016/j.actamat.2009.10.062.

[7] T. Matsudaira, M. Wada, T. Saitoh, S. Kitaoka, Oxygen permeability in cation-doped polycrystalline alumina under oxygen potential gradients at high temperatures, Acta Mater. 59 (2011) 5440–5450. doi:10.1016/j.actamat.2011.05.018.

[8] T. Matsudaira, M. Wada, S. Kitaoka, Effect of Dopants on the Distribution of Aluminum and Oxygen Fluxes in Polycrystalline Alumina Under Oxygen Potential

Gradients at High Temperatures, J. Am. Ceram. Soc. 96 (2013) 3243–3251. doi:10.1111/jace.12420.

[9] S. Kitaoka, T. Matsudaira, M. Wada, T. Saito, M. Tanaka, Y. Kagawa, Control of Oxygen Permeability in Alumina under Oxygen Potential Gradients at High Temperature by Dopant Configurations, J. Am. Ceram. Soc. 97 (2014) 2314–2322. doi:10.1111/jace.12935.

[10] P.Y. Hou, Impurity Effects on Alumina Scale Growth, J. Am. Ceram. Soc. 86 (2003) 660–68. doi:10.1111/j.1151-2916.2003.tb03355.x.

[11] B.A. Pint, K.L. More, I.G. Wright, Effect of Quaternary Additions on the Oxidation Behavior of Hf-Doped NiAl, Oxid. Met. 59 (2003) 257–283. doi:10.1023/A:1023087926788.

[12] B.A. Pint, Experimental observations in support of the dynamic-segregation theory to explain the reactive-element effect, Oxid. Met. 45 (1996) 1–37. doi:10.1007/BF01046818.

[13] B.A. Pint, K.B. Alexander, Grain Boundary Segregation of Cation Dopants in α - Al2 O 3 Scales, J. Electrochem. Soc. 145 (1998) 1819–1829. doi:10.1149/1.1838563.

[14] V. Deodeshmukh, N. Mu, B. Li, B. Gleeson, Hot corrosion and oxidation behavior of a novel Pt + Hf-modified γ′-Ni3Al + γ-Ni-based coating, Surf. Coat. Technol. 201 (2006) 3836–3840. doi:10.1016/j.surfcoat.2006.07.250.

[15] H. Cheng, S.J. Dillon, H.S. Caram, J.M. Rickman, H.M. Chan, M.P. Harmer, The Effect of Yttrium on Oxygen Grain-Boundary Transport in Polycrystalline Alumina

Measured Using Ni Marker Particles, J. Am. Ceram. Soc. 91 (2008) 2002–2008. doi:10.1111/j.1551-2916.2008.02391.x.

[16] Q. Wu, H.M. Chan, J.M. Rickman, M.P. Harmer, Effect of Hf 4+ Concentration on Oxygen Grain-Boundary Diffusion in Alumina, J. Am. Ceram. Soc. 98 (2015) 3346–3351. doi:10.1111/jace.13762.

[17] Q. Wu, Role of Hf4+ Doping on Oxygen Grain Boundary Diffusion in Alumina, Lehigh University, 2014.

[18] D.R. Mumm, A.G. Evans, I.T. Spitsberg, Characterization of a cyclic displacement instability for a thermally grown oxide in a thermal barrier system, Acta Mater. 49 (2001) 2329–2340. doi:10.1016/S1359-6454(01)00071-4.

[19] B.A. Pint, J.R. Martin, L.W. Hobbs, 18O/SIMS characterization of the growth mechanism of doped and undoped α-Al2O3, Oxid. Met. 39 (1993) 167–195. doi:10.1007/BF00665610.

[20] A.H. Heuer, T. Nakagawa, M.Z. Azar, D.B. Hovis, J.L. Smialek, B. Gleeson, N.D.M. Hine, H. Guhl, H.-S. Lee, P. Tangney, W.M.C. Foulkes, M.W. Finnis, On the growth of Al2O3 scales, Acta Mater. 61 (2013) 6670–6683. doi:10.1016/j.actamat.2013.07.024.

[21] A.H. Heuer, D.B. Hovis, J.L. Smialek, B. Gleeson, Alumina Scale Formation: A New Perspective, J. Am. Ceram. Soc. 94 (2011) s146–s153. doi:10.1111/j.1551-2916.2011.04573.x.

[22] V.K. Tolpygo, D.R. Clarke, Microstructural study of the theta-alpha transformation in alumina scales formed on nickel-aluminides, Mater. High Temp. 17 (2000) 59–70. doi:10.1179/mht.2000.011.

[23] G.C. Rybicki, J.L. Smialek, Effect of theθ-α-Al2O3 transformation on the oxidation behavior ofβ-NiAl + Zr, Oxid. Met. 31 (1989) 275–304. doi:10.1007/BF00846690.

[24] A.H. Heuer, Oxygen and aluminum diffusion in α-Al2O3: How much do we really understand?, J. Eur. Ceram. Soc. 28 (2008) 1495–1507. doi:10.1016/j.jeurceramsoc.2007.12.020.

[25] T. Amano, S. Yajima, Y. Saito, High-Temperature Oxidation Behavior of Fe–20Cr–4Al Alloys with Small Additions of Cerium, Trans. Jpn. Inst. Met. 20 (1979) 431–441. doi:10.2320/matertrans1960.20.431.

[26] H.M. Hindam, W.W. Smeltzer, Application of auger electron spectroscopy and inert metal marker techniques to determine metal and oxygen transport in oxide films on metals, Oxid. Met. 14 (1980) 337–349. doi:10.1007/BF00603789.

[27] E.W.A. Young, J.H.W. De Wit, The use of a 18O tracer and Rutherford backscattering spectrometry to study the oxidation mechanism of NiAl., Solid State Ion. 16 (1985) 39–46. doi:10.1016/0167-2738(85)90022-0.

[28] K.P.R. Reddy, J.L. Smialek, A.R. Cooper, 18O Tracer studies of Al2O3 scale formation on NiCrAl alloys, Oxid. Met. 17 (1982) 429–449. doi:10.1007/BF00742122.

[29] J. Jedlinski, G. Borchardt, On the oxidation mechanism of alumina formers, Oxid. Met. 36 (1991) 317–337. doi:10.1007/BF00662968.

[30] W.J. Quadakkers, A. Elschner, W. Speier, H. Nickel, Composition and growth mechanisms of alumina scales on FeCrAl-based alloys determined by SNMS, Appl. Surf. Sci. 52 (1991) 271–287. doi:10.1016/0169-4332(91)90069-V.

[31] R. Prescott, D.F. Mitchell, G.I. Sproule, M.J. Graham, Transport in α-Al2O3 scales on Fe□Al and Ni□Al alloys at 1100°C, Solid State Ion. 53 (1992) 229–237. doi:10.1016/0167-2738(92)90386-4.

[32] C. Mennicke, E. Schumann, M. Ruhle, R.J. Hussey, G.I. Sproule, M.J. Graham, The Effect of Yttrium on the Growth Process and Microstructure of α-Al2O3 on FeCrAl, Oxid. Met. 49 (1998) 455–466. doi:10.1023/A:1018803113093.

[33] B.A. Pint, Optimization of Reactive-Element Additions to Improve Oxidation Performance of Alumina-Forming Alloys, J. Am. Ceram. Soc. 86 (2003) 686–95. doi:10.1111/j.1151-2916.2003.tb03358.x.

[34] B.A. Pint, I.G. Wright, W.Y. Lee, Y. Zhang, K. Prüßner, K.B. Alexander, Substrate and bond coat compositions: factors affecting alumina scale adhesion, Mater. Sci. Eng. A. 245 (1998) 201–211. doi:10.1016/S0921-5093(97)00851-4.

[35] B.A. Pint, J.R. Martin, L.W. Hobbs, 18O/SIMS characterization of the growth mechanism of doped and undoped α-Al2O3, Oxid. Met. 39 (1993) 167–195. doi:10.1007/BF00665610.

[36] S.N. Basu, J.W. Halloran, Tracer isotope distribution in growing oxide scales, Oxid. Met. 27 (1987) 143–155. doi:10.1007/BF00667055.

[37] B.A. Pint, A.J. Garratt-Reed, L.W. Hobbs, Possible Role of the Oxygen Potential Gradient in Enhancing Diffusion of Foreign Ions on α-Al2O3 Grain Boundaries, J. Am. Ceram. Soc. 81 (1998) 305–314. doi:10.1111/j.1151-2916.1998.tb02335.x.

[38] C. Wagner, Theory of the tarnishing process, Z. Für Phys. Chem. Abt. B. B21 (1933) 25–41.

[39] P. Kofstad, High-temperature oxidation of metals, John Wiley & Sons, Inc., 1966.

[40] N. Birks, G.H. Meier, F.S. Pettit, Introduction to the High Temperature Oxidation of Metals, Cambridge University Press, 2006.

[41] J. Pappis, W.D. Kingery, Electrical Properties of Single-Crystal and Polycrystalline Alumina at High Temperatures, J. Am. Ceram. Soc. 44 (1961) 459–464. doi:10.1111/j.1151-2916.1961.tb13756.x.

[42] K. Kitazawa, R.L. Coble, Electrical Conduction in Single-Crystal and Polycrystalline Al2O3 at High Temperatures, J. Am. Ceram. Soc. 57 (1974) 245–250. doi:10.1111/j.1151-2916.1974.tb10879.x.

[43] J.-S. Chen, F.A. Kröger, Electrical and optical properties of single crystalline α-Al2O3 doped with nickel, J. Mater. Sci. 20 (1985) 3191–3200. doi:10.1007/BF00545185.

[44] J.S. Sheasby, D.B. Jory, Electrical properties of growing alumina scales, Oxid. Met. 12 (1978) 527–539. doi:10.1007/BF00603808.

[45] D. Nicolas-Chaubet, A.M. Huntz, F. Millot, Electrochemical method for the investigation of transport properties of alumina scales formed by oxidation, J. Mater. Sci. 26 (1991) 6113–6118. doi:10.1007/BF01113892.

[46] D. Nicolas-Chaubet, A.M. Huntz, F. Millot, Electrochemical method for the investigation of transport properties of alumina scales formed by oxidation, J. Mater. Sci. 26 (1991) 6119–6126. doi:10.1007/BF01113893.

[47] J. Balmain, A.M. Huntz, Improvement of the application of an electrochemical method for the determination of transport properties of anα-alumina scale. Part II: Influence of yttrium and palladium on alumina scales developed on aβ-NiAl alloy, Oxid. Met. 46 (1996) 213–234. doi:10.1007/BF01050797.

[48] D.M. Smyth, The Defect Chemistry of Metal Oxides, Oxford University Press, Inc., 2000.

[49] B.V. Dutt, J.P. Hurrell, F.A. Kröger, High-Temperature Defect Structure of Cobalt-Doped α-Alumina, J. Am. Ceram. Soc. 58 (1975) 420–427. doi:10.1111/j.1151-2916.1975.tb19014.x.

[50] S.K. Mohapatra, F.A. Kröger, Defect Structure of α-Al2O3 Doped with Titanium, J. Am. Ceram. Soc. 60 (1977) 381–387. doi:10.1111/j.1151-2916.1977.tb15517.x.

[51] B.V. Dutt, F.A. Kröger, High-Temperature Defect Structure of Iron-Doped α-Alumina, J. Am. Ceram. Soc. 58 (1975) 474–476. doi:10.1111/j.1151-2916.1975.tb18761.x.

[52] S.K. Mohapatra, F.A. Kröger, The Dominant Type of Atomic Disorder in α-Al2O3, J. Am. Ceram. Soc. 61 (1978) 106–109. doi:10.1111/j.1151-2916.1978.tb09249.x.

[53] K. Matsunaga, T. Tanaka, T. Yamamoto, Y. Ikuhara, First-principles calculations of intrinsic defects in ${\mathrm{Al}}_{2}{\mathrm{O}}_{3}$, Phys. Rev. B. 68 (2003) 085110. doi:10.1103/PhysRevB.68.085110.

[54] N.D.M. Hine, K. Frensch, W.M.C. Foulkes, M.W. Finnis, Supercell size scaling of density functional theory formation energies of charged defects, Phys. Rev. B. 79 (2009) 024112. doi:10.1103/PhysRevB.79.024112.

[55] C.R.A. Catlow, R. James, W.C. Mackrodt, R.F. Stewart, Defect energetics in $\ensuremath{\alpha}$-${\mathrm{Al}}_{2}$${\mathrm{O}}_{3}$ and rutile Ti${\mathrm{O}}_{2}$, Phys. Rev. B. 25 (1982) 1006–1026. doi:10.1103/PhysRevB.25.1006.

[56] R.W. Grimes, Solution of MgO, CaO, and TiO2 in α-AI2O3, J. Am. Ceram. Soc. 77 (1994) 378–384. doi:10.1111/j.1151-2916.1994.tb07005.x.

[57] K.P.D. Lagerlöf, R.W. Grimes, The defect chemistry of sapphire (α-Al2O3), Acta Mater. 46 (1998) 5689–5700. doi:10.1016/S1359-6454(98)00256-0.

[58] W.H. Strehlow, E.L. Cook, Compilation of Energy Band Gaps in Elemental and Binary Compound Semiconductors and Insulators, J. Phys. Chem. Ref. Data. 2 (1973) 163–200. doi:10.1063/1.3253115.

[59] R.H. French, Electronic Band Structure of Al2O3, with Comparison to Alon and AIN, J. Am. Ceram. Soc. 73 (1990) 477–489. doi:10.1111/j.1151-2916.1990.tb06541.x.

[60] W.M. Haynes, CRC Handbook of Chemistry and Physics, 93rd Edition, CRC Press, 2012.

[61] K.J.W. Atkinson, R.W. Grimes, M.R. Levy, Z.L. Coull, T. English, Accommodation of impurities in α-Al2O3, α-Cr2O3 and α-Fe2O3, J. Eur. Ceram. Soc. 23 (2003) 3059–3070. doi:10.1016/S0955-2219(03)00101-8.

[62] L. Feng, S.J. Dillon, Cr3+ chemical diffusivity in aliovalent doped aluminas, J. Eur. Ceram. Soc. (n.d.). doi:10.1016/j.jeurceramsoc.2017.04.053.

[63] J. Cho, C.M. Wang, H.M. Chan, J.M. Rickman, M.P. Harmer, Role of segregating dopants on the improved creep resistance of aluminum oxide, Acta Mater. 47 (1999) 4197–4207. doi:10.1016/S1359-6454(99)00278-5.

[64] I. Sakaguchi, V. Srikanth, T. Ikegami, H. Haneda, Grain Boundary Diffusion of Oxygen in Alumina Ceramics, J. Am. Ceram. Soc. 78 (1995) 2557–2559. doi:10.1111/j.1151-2916.1995.tb08703.x.

[65] T. Nakagawa, H. Nishimura, I. Sakaguchi, N. Shibata, K. Matsunaga, T. Yamamoto, Y. Ikuhara, Grain boundary character dependence of oxygen grain boundary diffusion in α-Al2O3 bicrystals, Scr. Mater. 65 (2011) 544–547. doi:10.1016/j.scriptamat.2011.06.024.

[66] T. Nakagawa, I. Sakaguchi, N. Shibata, K. Matsunaga, T. Mizoguchi, T. Yamamoto, H. Haneda, Y. Ikuhara, Yttrium doping effect on oxygen grain boundary diffusion in α-Al2O3, Acta Mater. 55 (2007) 6627–6633. doi:10.1016/j.actamat.2007.08.016.

[67] P. Fielitz, K. Kelm, R. Bertram, A.H. Chokshi, G. Borchardt, Aluminium-26 grain boundary diffusion in pure and Y-doped polycrystalline α-alumina, Acta Mater. 127 (2017) 302–311. doi:10.1016/j.actamat.2017.01.005.

[68] P.R. Cantwell, M. Tang, S.J. Dillon, J. Luo, G.S. Rohrer, M.P. Harmer, Grain boundary complexions, Acta Mater. 62 (2014) 1–48. doi:10.1016/j.actamat.2013.07.037.

[69] S.J. Dillon, M. Tang, W.C. Carter, M.P. Harmer, Complexion: A new concept for kinetic engineering in materials science, Acta Mater. 55 (2007) 6208–6218. doi:10.1016/j.actamat.2007.07.029.

[70] S.J. Dillon, M.P. Harmer, Relating Grain-Boundary Complexion to Grain-Boundary Kinetics I: Calcia-Doped Alumina, J. Am. Ceram. Soc. 91 (2008) 2304–2313. doi:10.1111/j.1551-2916.2008.02454.x.

[71] S.J. Dillon, M.P. Harmer, Relating Grain Boundary Complexion to Grain Boundary Kinetics II: Silica-Doped Alumina, J. Am. Ceram. Soc. 91 (2008) 2314–2320. doi:10.1111/j.1551-2916.2008.02432.x.

[72] J. Luo, H. Cheng, K.M. Asl, C.J. Kiely, M.P. Harmer, The Role of a Bilayer Interfacial Phase on Liquid Metal Embrittlement, Science. 333 (2011) 1730–1733. doi:10.1126/science.1208774.

[73] V.K. Gupta, D.-H. Yoon, H.M. Meyer, J. Luo, Thin intergranular films and solid-state activated sintering in nickel-doped tungsten, Acta Mater. 55 (2007) 3131–3142. doi:10.1016/j.actamat.2007.01.017.

[74] W.D. Kingery, H.K. Bowen, D.R. Uhlmann, Introduction to Ceramics, 2nd ed., Wiley-Interscience, 1976.

[75] M.I. Mendelson, Average Grain Size in Polycrystalline Ceramics, J. Am. Ceram. Soc. 52 (1969) 443–446. doi:10.1111/j.1151-2916.1969.tb11975.x.

[76] C.A. Schneider, W.S. Rasband, K.W. Eliceiri, NIH Image to ImageJ: 25 years of image analysis, Nat. Methods. 9 (2012) 671–675. doi:10.1038/nmeth.2089.

[77] S. Bhattacharya, A.R. Riahi, A.T. Alpas, Indentation-induced subsurface damage in silicon particles of Al–Si alloys, Mater. Sci. Eng. A. 527 (2009) 387–396. doi:10.1016/j.msea.2009.08.052.

[78] M. Nanko, High-temperature oxidation of ceramic matrix composites dispersed with metallic particles, Sci. Technol. Adv. Mater. 6 (2005) 129–134. doi:10.1016/j.stam.2004.11.004.

[79] K. Trumble, M. Ruhle, The thermodynamics of spinel interphase formation at diffusion-bonded nickel alumina Ni/Al2O3 interfaces, Acta Metall. Mater. 39 (1991) 1915–1924.

[80] T. Sekino, T. Nakajima, S. Ueda, K. Niihara, Reduction and Sintering of a Nickel–Dispersed-Alumina Composite and Its Properties, J. Am. Ceram. Soc. 80 (1997) 1139–1148. doi:10.1111/j.1151-2916.1997.tb02956.x.

[81] K. Stiller, L. Viskari, G. Sundell, F. Liu, M. Thuvander, H.-O. Andrén, D.J. Larson, T. Prosa, D. Reinhard, Atom Probe Tomography of Oxide Scales, Oxid. Met. 79 (2012) 227–238. doi:10.1007/s11085-012-9330-6.

[82] S.-I. Baik, X. Yin, D.N. Seidman, Correlative atom-probe tomography and transmission electron microscope study of a chemical transition in a spinel on an oxidized nickel-based superalloy, Scr. Mater. 68 (2013) 909–912. doi:10.1016/j.scriptamat.2013.02.025.

[83] F. Liu, K. Stiller, Atom probe tomography of thermally grown oxide scale on FeCrAl, Ultramicroscopy. 132 (2013) 279–284. doi:10.1016/j.ultramic.2013.02.004.

[84] Y. Chen, R.C. Reed, E.A. Marquis, Interfacial Solute Segregation in the Thermally Grown Oxide of Thermal Barrier Coating Structures, Oxid. Met. 82 (2014) 457–467. doi:10.1007/s11085-014-9502-7.

[85] Y. Dong, T. Barth, Y. Chen, E.A. Marquis, Oxide Scales Revealed by Atom Probe Tomography., Microsc. Microanal. 22 (2016) 656–657. doi:10.1017/S143192761600413X.

[86] K. Stiller, M. Thuvander, I. Povstugar, P.P. Choi, H.-O. Andrén, Atom probe tomography of interfaces in ceramic films and oxide scales, MRS Bull. 41 (2016) 35–39. doi:10.1557/mrs.2015.307.

[87] K.A. Unocic, B.A. Pint, Characterization of the alumina scale formed on a commercial MCrAlYHfSi coating, Surf. Coat. Technol. 205 (2010) 1178–1182. doi:10.1016/j.surfcoat.2010.08.111.

[88] K.A. Unocic, C.M. Parish, B.A. Pint, Characterization of the alumina scale formed on coated and uncoated doped superalloys, Surf. Coat. Technol. 206 (2011) 1522–1528. doi:10.1016/j.surfcoat.2011.07.044.

[89] B.A. Pint, K.L. More, Characterization of alumina interfaces in TBC systems, J. Mater. Sci. 44 (2009) 1676–1686. doi:10.1007/s10853-008-3221-x.

[90] T.A. Ramanarayanan, M. Raghavan, R. Petkovic-Luton, The Characteristics of Alumina Scales Formed on Fe-Based Yttria-Dispersed Alloys, J. Electrochem. Soc. 131 (1984) 923–931. doi:10.1149/1.2115728.

[91] D.J. Young, D. Naumenko, L. Niewolak, E. Wessel, L. Singheiser, W.J. Quadakkers, Oxidation kinetics of Y-doped FeCrAl-alloys in low and high pO2 gases, Mater. Corros. 61 (2010) 838–844. doi:10.1002/maco.200905432.

[92] A. Chatterjee, S. Srikanth, S. Sanyal, L. Krishna, K. Anand, P.R. Subramanian, Kinetic modeling of high temperature oxidation of Ni-base alloys, Comput. Mater. Sci. 50 (2011) 811–819. doi:10.1016/j.commatsci.2010.10.006.

[93] J. Roberts, Microstructural Considerations in Gas Permeation, Ceram Microstruct Proc Int Mater Symp 3rd. (1968) 509–521.

[94] H. Cheng, H.S. Caram, W.E. Schiesser, J.M. Rickman, H.M. Chan, M.P. Harmer, Oxygen grain-boundary transport in polycrystalline alumina using wedge-geometry bilayer samples: Effect of Y-doping, Acta Mater. 58 (2010) 2442–2451. doi:10.1016/j.actamat.2009.12.030.

[95] H. Cheng, Role of Yttrium and Nickel on Oxygen Grain Boundary Diffusion in Alumina, Lehigh University, 2009.

[96] Z. Yu, Q. Wu, J.M. Rickman, H.M. Chan, M.P. Harmer, Atomic-resolution observation of Hf-doped alumina grain boundaries, Scr. Mater. 68 (2013) 703–706. doi:10.1016/j.scriptamat.2013.01.015.

[97] M.J. Saxton, Anomalous diffusion due to obstacles: a Monte Carlo study, Biophys. J. 66 (1994) 394–401. doi:10.1016/S0006-3495(94)80789-1.

[98] M.N. Kelly, S.A. Bojarski, G.S. Rohrer, The temperature dependence of the relative grain-boundary energy of yttria-doped alumina, J. Am. Ceram. Soc. 100 (2017) 783–791. doi:10.1111/jace.14488.

[99] S.A. Bojarski, M. Stuer, Z. Zhao, P. Bowen, G.S. Rohrer, Influence of Y and La Additions on Grain Growth and the Grain-Boundary Character Distribution of Alumina, J. Am. Ceram. Soc. 97 (2014) 622–630. doi:10.1111/jace.12669.

[100] S.K. Behera, P.R. Cantwell, M.P. Harmer, A grain boundary mobility discontinuity in reactive element Zr-doped Al2O3, Scr. Mater. 90–91 (2014) 33–36. doi:10.1016/j.scriptamat.2014.07.010.

VITA

Yan Wang was born on January 9th, 1989 in Tianjin, China, to Weiqi Wang and Meiyun Wang. Yan grew up in Tianjin. He went to Nankai middle school and Nankai high school in Tianjin, and graduated in 2007. Then he went to Tsinghua University in Beijing and graduated with a Bachelor of Science in Materials Science and Engineering in 2011. In August 2011, Yan came to Lehigh University to pursue his Ph.D. degree in Materials Science and Engineering. At Lehigh, he worked with Prof. Martin P. Harmer, Prof. Helen M. Chan and Prof. Jeffrey M. Rickman. Following graduation, Yan will pursue an industrial career at Corning as a ceramic process research scientist.